

# Journal of THERMOELECTRICITY

International Research

Founded in December, 1993

published 6 times a year

---

No. 5

2016

---

## Editorial Board

Editor-in-Chief LUKYAN I. ANATYCHUK

Petro I. Baransky

Bogdan I. Stadnyk

Lyudmyla N. Vikhor

Oleg J. Luste

Valentyn V. Lysko

Elena I. Rogacheva

Stepan V. Melnychuk

Andrey A. Snarskii

## International Editorial Board

Lukyan I. Anatyshuk, *Ukraine*

A.I. Casian, *Moldova*

Steponas P. Ašmontas, *Lithuania*

Takenobu Kajikawa, *Japan*

Jean-Claude Tedenac, *France*

T. Tritt, *USA*

H.J. Goldsmid, *Australia*

Sergiy O. Filin, *Poland*

L. Chen, *China*

D. Sharp, *USA*

T. Caillat, *USA*

Yuri Gurevich, *Mexico*

Yuri Grin, *Germany*

Founders – National Academy of Sciences, Ukraine  
Institute of Thermoelectricity of National Academy of Sciences and Ministry  
of Education and Science of Ukraine

Certificate of state registration № KB 15496-4068 ИП

Editorial office manager Ye. Bryzytska

Editors:

L. Vikhor, V. Kramar, V. Katerynchuk, O. Luste, T. Podbegalina

Approved for printing by the Academic Council of Institute of Thermoelectricity  
of the National Academy of Sciences and Ministry of Education and Science, Ukraine

Address of editorial office:

Ukraine, 58002, Chernivtsi, General Post Office, P.O. Box 86.

Phone: +(380-372) 90 31 65.

Fax: +(380-3722) 4 19 17.

E-mail: [jt@inst.cv.ua](mailto:jt@inst.cv.ua)

<http://www.jt.inst.cv.ua>

---

Signed for publication 25.11.16. Format 70×108/16. Offset paper №1. Offset printing.  
Printer's sheet 11.5. Publisher's signature 9.2. Circulation 400 copies. Order 5.

---

Printed from the layout original made by “Journal of Thermoelectricity” editorial board  
in the printing house of “Bukrek” publishers,  
10, Radischev Str., Chernivtsi, 58000, Ukraine

Copyright © Institute of Thermoelectricity, Academy of Sciences  
and Ministry of Education and Science, Ukraine, 2016

## CONTENTS

### **Theory**

- L.I. Anatychuk, L.M. Vikhor, M.P. Kotsur, R.R. Kobylianskyi, T.Ya. Kadenyuk.* Optimal control of time dependence of cooling temperature in thermoelectric devices 5
- Rasit Ahiska, Gunay Omer.* Thermoelectricity in Turkey 12
- P.V. Gorskiy.* Lattice thermal conductivity of thermoelectric materials based on *Zn-Cd-Sb* 23

### **Materials Research**

- Montasser S. Tahat.* Mechanical and thermo-electric properties of *Cu/SiC/Gr* multi-layer hybrid metal matrix composite 30
- V.P. Shafraniuk.* Research on mechanical stress relaxation in real crystals by X-ray diffraction moire method 37
- E.I. Rogacheva, K.V. Martynova, A.S. Bondarenko.* Thermoelectric and mechanical properties of  $(Bi_{1-x}Sb_x)_2Te_3$  ( $x = 0 \div 0.07$ ) semiconductor solid solutions 47
- O.N. Manik, T.O. Manik, V.R. Bilinsky-Slotylo.* Peculiarities of electronic structure of hybrid orbitals and interatomic interaction in cadmium antimonide crystals 57

### **Design**

- L.I. Anatychuk, R.R. Kobylianskyi, I.A. Konstantinovich, V.V. Lys'ko, O.V. Puhantseva, Yu.Yu. Rozver, V.A. Tiumentsev.* Calibration bench for thermoelectric converters of heat flux 65
- U.I. Abdulkhakimov, D.V. Yevdulov, O.V. Yevdulov, N.A. Nabiev.* Model of thermoelectric device for carrying out thermal cosmetology procedures 73

### **Thermoelectric products**

- M.V. Maksimuk, I.S. Andrusiak.* Electronic control unit for thermoelectric automobile starting pre-heater 80
- L.I. Anatychuk, A.V. Prybyla, M.M. Korop.* Comparative analysis of thermoelectric and compression heat pumps for individual air conditioners at elevated ambient temperatures 87



**L.I. Anatychuk<sup>1,2</sup>, L.M. Vikhor<sup>1</sup>, M.P. Kotsur<sup>1</sup>,  
R.R. Kobylanskyi<sup>1,2</sup>, T.Ya. Kadenyuk<sup>1</sup>**

<sup>1</sup>Institute of Thermoelectricity of the NAS and MES Ukraine,  
1 Nauky str., Chernivtsi, 58029, Ukraine;  
<sup>2</sup>Yu.Fedkovich Chernivtsi National University,  
2 Kotsyubynsky str., Chernivtsi, 58012, Ukraine

## **OPTIMAL CONTROL OF TIME DEPENDENCE OF COOLING TEMPERATURE IN THERMOELECTRIC DEVICES**

---

*We consider a physical model of thermoelement in the unsteady-state cooling mode, on the cold surface of which account is taken of the volumetric heat capacity of connecting and insulating plates, heat release of the object, heat exchange with the environment, the Joule heat release on the contact resistances between thermoelectric material and metal interconnects, as well as the influence of the Thomson effect in the bulk of thermoelement legs. A method for calculation of optimal time dependences of thermoelement supply current ensuring the prescribed time dependences of cooling temperature is described. Examples of computer simulation results of optimal current control functions for given continuous, piecewise continuous and periodic functions of cooling temperature versus time are provided.*

**Key words:** thermoelement, unsteady-state thermoelectric cooling process, time dependences of temperature, current control functions.

### **Introduction**

The thermoelectric cooling method is widely used to provide thermal modes for a variety of electronic, medical and measuring devices. In some cases, such devices operate in dynamic modes, which require changing the temperature of cooling (heating) the object in accordance with the prescribed time law. The thermoelectric cooler makes it easy to realize such dynamic modes by controlling the temperature of cooling (heating) due to time variation of thermoelement supply current.

The actual problem of thermoelectric cooling or heating control lies in the establishment of optimal time dependence of supply current that would ensure the prescribed time dependence of the operating surface temperature of thermoelements. This problem relates to the problems of control synthesis of the process of unsteady-state thermoelectric cooling or heating.

Analysis of scientific information [1 – 10] shows that published results of theoretical research on the unsteady-state cooling process mainly concern determination of temperature behavior in thermoelement powered from current pulses of certain prescribed shape. As regards control synthesis problems related to search for optimal time functions of current for the unsteady-state cooling and heating processes, ways to solve them have not been adequately studied.

The purpose of the work was to develop the algorithm and computer means for the calculation of optimal time dependence of thermoelectric converter supply current ensuring in accordance with the prescribed law a change in the temperature of object which is cooled or heated by this converter.

The problem of cooling temperature control synthesis in the unsteady-state mode is related to solving two questions. First of all, it is necessary to be able to determine whether or not the prescribed

time dependence of cooling temperature can be realized, since the possibility of achieving the prescribed temperature within certain time is related to restricted fast response of thermoelectric cooler. Answer to this question is given by solving optimization problem of finding minimum cooling temperature during certain time interval. Computer methods of solving this problem were proposed in [11, 12]. In these works it is shown which minimal temperature is achieved in the unsteady-state cooling mode during different time intervals with the aid of single-stage and two-stage thermoelectric coolers.

The second question lies in finding the algorithm according to which for the prescribed time function of cooling temperature  $T_c(t)$  the shape of control current pulse  $I(t)$  is determined. The methods of solving such problem were considered in [13, 14]. The results were obtained for the approximate physical models of thermoelectric cooler in the unsteady-state mode. Only one thermoelectric leg was considered, whose material parameters, namely the Seebeck coefficient  $\alpha$ , coefficient of resistivity  $\rho$ , coefficient of thermal conductivity  $\kappa$  and volumetric heat capacity  $c$ , do not depend on temperature. In [13], on the cold surface of leg, only the Peltier heat absorption is taken into account, disregarding the heat capacity of cooled object, the Joule heat release on the contact resistance between thermoelectric material of the leg and metal interconnects which have a significant impact on cooling temperature in a dynamic mode [15]. In [14], the influence of these factors is taken into account, but the intensity of active heat release of cooled object in the process of unsteady-state cooling is disregarded, which is also important in practical application. Therefore, to find a relationship between given temperature function  $T_c(t)$  and control current  $I(t)$ , we will use the specified physical model of thermoelement.

### Physical model of thermoelement in the unsteady-state mode and its mathematical description

Schematic of thermoelement in the unsteady-state cooling mode is shown in Fig. 1. The thermoelement legs of height  $l$  and cross-section  $s$  are made of  $n$ - and  $p$ -type conductivity materials. Characteristics of leg materials, namely the Seebeck coefficient  $\alpha_{n,p}(T)$  and coefficient of resistivity  $\rho_{n,p}(T)$  are temperature-dependent, and coefficient of thermal conductivity  $\kappa_{n,p}$  and coefficient of heat capacity  $c_{n,p}$  will be assumed to be constants due to their inessential dependence on temperature in thermoelectric materials for coolers.

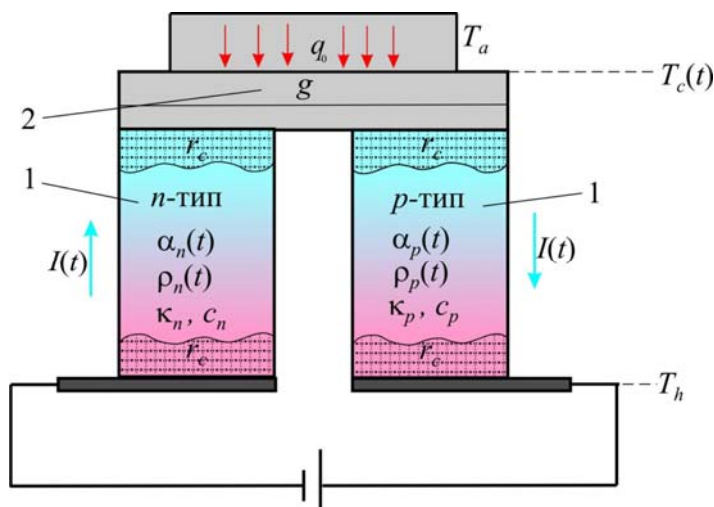


Fig. 1. Schematic of thermoelement in the unsteady-state cooling mode.  
 1 – thermoelement legs, 2 – lumped volumetric heat capacity  
 g of connecting and insulating plates of cooled object.

It is assumed that heat-releasing surface of thermoelement is maintained at fixed temperature  $T_h$ , the lateral surface of legs is adiabatically insulated. At the cold junction of thermoelement we take into account absorption of the Peltier heat, release of the Joule heat on the junction contacts with contact resistance  $r_c$ , lumped volumetric heat capacity  $g$  of connecting and insulating plates and cooled object, heat exchange between the cold surface and the environment with temperature  $T_a$ , as well as active heat release of cooled object of power  $q_0$ .

For such a model temperature distribution in thermoelement legs is assigned by a system of one-dimensional equations of unsteady-state heat conduction given by

$$\begin{cases} c_n \frac{\partial T_n}{\partial t} = \kappa_n \frac{\partial^2 T_n}{\partial x^2} + \rho_n(T) \frac{I^2(t)}{s^2} - T_n \frac{\partial \alpha_n(T)}{\partial T_n} \frac{I(t)}{s} \frac{\partial T_n}{\partial x} \\ c_p \frac{\partial T_p}{\partial t} = \kappa_p \frac{\partial^2 T_p}{\partial x^2} + \rho_p(T) \frac{I^2(t)}{s^2} - T_p \frac{\partial \alpha_p(T)}{\partial T_p} \frac{I(t)}{s} \frac{\partial T_p}{\partial x} \end{cases}, \quad (1)$$

where  $x \in [0, l]$ ,  $t \in [0, t_{\max}]$ .  $I(t)$  is current in thermoelement legs which is a function of time. Eqs.(1) take into account the Thomson effect which arises in the bulk of thermoelement legs due to temperature dependence of the Seebeck coefficient  $\alpha_{n,p}(T)$ .

The boundary conditions for these equations are of the form:

$$\begin{aligned} \left[ \kappa_n s \frac{\partial T_n}{\partial x} + \kappa_p s \frac{\partial T_p}{\partial x} \right]_{x=0} - [\alpha_p(T_c(t)) + |\alpha_n(T_c(t))|] I(t) T_c(t) - \\ - g \frac{\partial T_c(t)}{\partial t} - 2sH(T_c(t) - T_a) + 2 \frac{r_c}{s} I^2(t) + q_0 = 0 \\ T_n(0, t) = T_p(0, t) \equiv T_c(t) \\ T_n(l, t) = T_p(l, t) \equiv T_h \end{aligned} \quad (2)$$

where  $T_c(t)$ , the temperature of thermoelement cold surface, is the prescribed function of time,  $H$  – coefficient of convective heat exchange in the environment.

Initial temperature distribution in the legs corresponds to steady-state distribution with the initial value of current  $I_0$  and is given as a function

$$T_{n,p}(x, 0) = C_0 I_0^2 x^2 + C_1 x + C_2. \quad (3)$$

where  $C_0$ ,  $C_1$  and  $C_2$  are constants determined by solutions of a steady-state problem of thermal conductivity in thermoelement legs at constant current  $I_0$ .

Under conditions  $I_0 = 0$  A,  $T_h = T_a$  the initial conditions of the boundary problem (1) – (2) will have a simple form

$$T_n(x, 0) = T_p(x, 0) \equiv T_a. \quad (4)$$

The problem is to find current control function  $I(t)$  such that would ensure the prescribed time dependence of cold temperature  $T_c(t)$ .

### **Solving the problem of optimal control synthesis**

To solve the formulated problem, we use the averaged parameter values of thermoelement leg materials, namely

$$\alpha = (\overline{\alpha_p} + |\overline{\alpha_n}|) / 2; \quad \rho = (\overline{\rho_p} + \overline{\rho_n}) / 2; \quad \kappa = (\kappa_p + \kappa_n) / 2; \quad c = (c_p + c_n) / 2. \quad (5)$$

Note that in the first approximation the influence of the Thomson effect in Eqs.(1) can be taken into account by the arithmetic averaging of the Seebeck coefficients in the operating temperature range [16], while for coefficients of resistivity it is advisable to use the integral averaging [16]. Then the average values of these coefficients in (5) are determined as follows:

$$\overline{\alpha_{n,p}} = (\alpha_{n,p}(T_h) + \alpha_{n,p}(T_c(t))) / 2, \quad (6)$$

$$\overline{\rho_{n,p}} = \frac{1}{(T_h - T_c(t))} \int_{T_c(t)}^{T_h} \rho_{n,p} dT. \quad (7)$$

Such approximations allow solving instead of problem (1) – (3) for thermoelement a similar initial boundary problem of unsteady-state thermal conduction for a single leg with averaged according to (5) – (7) thermoelectric parameters  $\alpha$ ,  $\rho$ ,  $\kappa$  and  $c$ .

Using the Laplace transform method, as it was proposed in [14], we obtain the relation between given function of cooling temperature  $T_c(t)$  and current control function  $I(t)$  in the form

$$I(t) = \frac{1}{\alpha T_c(t)} \left[ \frac{r_c}{s} I^2(t) + \frac{\kappa \rho}{c s l} \int_0^{at} K(t - \tau) I^2(\tau) d\tau + \Phi(t, T_c(t)) \right], \quad (8)$$

where

$$\Phi(t, T_c(t)) = -g \frac{dT_c(t)}{dt} - HsT_c(t) - \frac{r_c}{s} I_0^2 + A - \frac{\kappa s}{l} \int_0^{at} \mathfrak{G}_1(t - \tau) \frac{dT_c(\tau)}{d\tau} d\tau - \frac{\kappa \rho}{c s l} I_0^2 \int_0^{at} K(\tau) d\tau,$$

$$A = (\alpha I_0 + Hs) \frac{\frac{\kappa s}{l} T_h + HsT_a + q_0 + (0.5 + \frac{r_c}{\rho l}) \frac{\rho l}{s} I_0^2}{\alpha I_0 + Hs + \frac{\kappa s}{l}},$$

$$a = \frac{\kappa}{cl^2}, \quad K(t) = \mathfrak{G}_1(t) - \mathfrak{G}_0(t), \quad \mathfrak{G}_1(t) = 1 + 2 \sum_{k=1}^{\infty} \exp(-\pi^2 k^2 at), \quad \mathfrak{G}_0(t) = 1 + 2 \sum_{k=1}^{\infty} (-1)^k \exp(-\pi^2 k^2 at)$$

Relation (8) is a nonlinear integral equation which is solved by numerical method of successive approximations. A fairly complex algorithm for solving such an equation is realized with the help of computer simulation software developed in the MathLab environment.

### Computer simulation results

Simulation of current control functions ensuring the prescribed time dependences of cooling temperature was performed for thermoelements the legs of which are made of *Bi-Te* based materials of *n*- and *p*-type conductivity with standard thermoelectric characteristics  $\alpha_{n,p}$ ,  $\rho_{n,p}$ ,  $\kappa_{n,p}$ ,  $c_{n,p}$  [17]. Calculations were performed for the legs of height  $l = 0.14$  cm, cross-section area  $s = 0.1 \times 0.1$  cm<sup>2</sup>, with contact resistance value  $r_c = 5 \cdot 10^{-6}$  Ohm·cm<sup>2</sup>. Account was taken of heat exchange between the heat-absorbing surface of thermoelements and the environment of temperature  $T_a = 300$  K, with the heat exchange coefficient  $H = 10^{-3}$  W/cm<sup>2</sup>K. The lumped volumetric heat capacity of connecting and insulating plates and cooled object was equal to  $g = 0.002$  J/K. Considered were variants of modules



operation in the mode without thermal load, that is, the value of heat release of cooled object was assumed equal to  $q_0 = 0$ , and with the load per one leg  $q_0 = 0.03$  W.

Figs. 2 – 4 show examples of the prescribed time dependences of cooling temperature  $T_c(t)$  and the respective control functions of thermoelement supply current  $I(t)$  calculated for them. Fig. 2 gives dependences  $I(t)$  ensuring continuous temperature reduction to the prescribed value within the prescribed time interval.

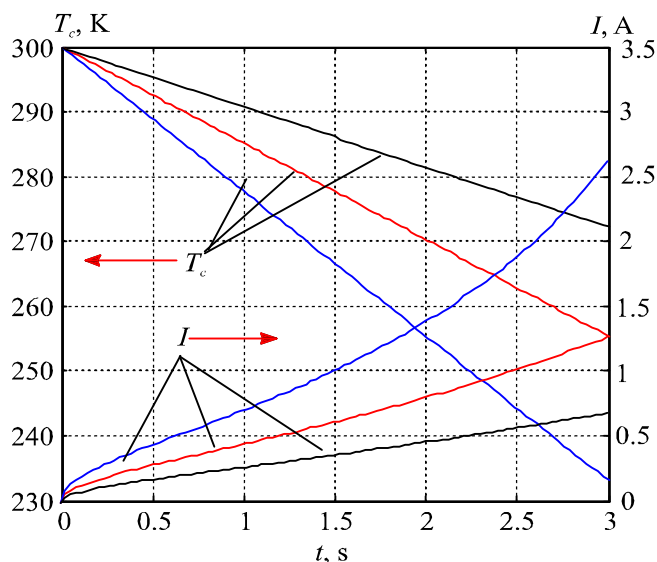


Fig. 2. The prescribed time dependences of cooling temperature  $T_c(t)$  and the respective control functions of thermoelement supply current  $I(t)$ .  $q_0 = 0$ .

Fig. 3 shows examples of piecewise linear function of temperature versus time  $T_c(t)$  and their respective controls  $I(t)$ . It is apparent that the choice of such optimal control makes it possible to reduce the time required by thermoelectric device for reaching steady-state mode.

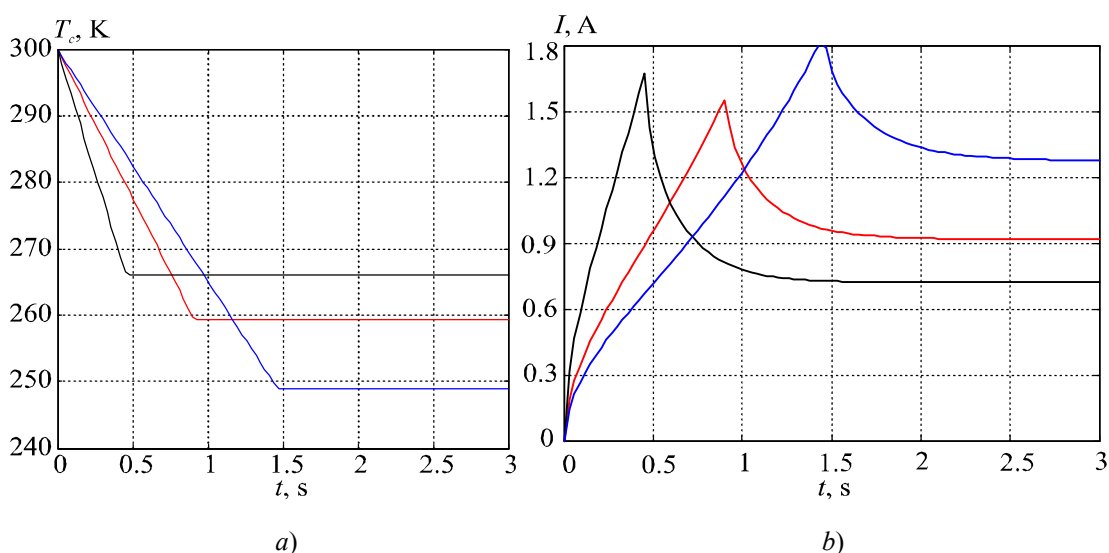


Fig. 3. a) The prescribed time dependences of cooling temperature  $T_c(t)$  and b) the respective control functions of thermoelement supply current  $I(t)$ .  $q_0 = 0$ .

Fig. 4 shows a periodic change in cooling temperature which is ensured by the respective periodic control function of thermoelement supply current.

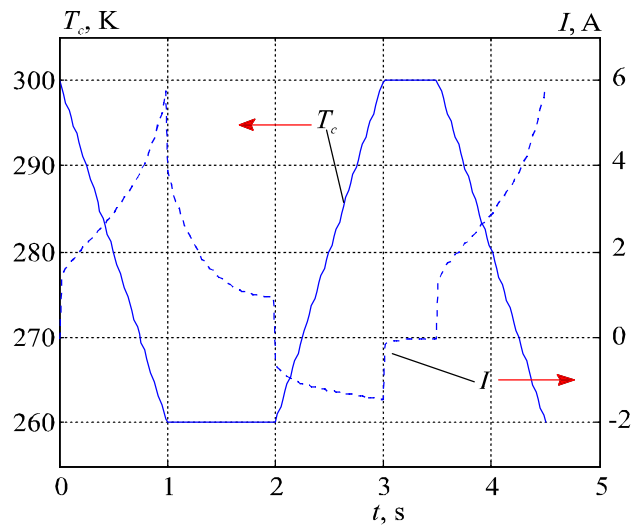


Fig. 4. The prescribed time dependences of cooling temperature  $T_c(t)$  and the respective control functions of thermoelement supply current  $I(t)$ .  $q_0 = 0.03$  W.

## Conclusions

1. The developed computer simulation method allows determination of optimal time functions of thermoelement supply current control ensuring the prescribed dependences of change in cooling temperature with time. It should be noted that there are practically no experimental methods which would allow finding similar functions for thermoelement current control.
2. Establishment of the time dependences of current optimal for specific purposes is of important practical significance. Such functions are used for the design and autocalibration of special electronic regulators which are necessary to ensure the operation of system for automatic control of unsteady-state cooling process in thermoelectric devices of various applications.

## References

1. G. J. Snyder, J.-P. Fleurial, T. Caillat, R. G. Yang, G. J. Chen, Supercooling of Peltier Cooler Using a Current Pulse, *J. Applied Physics* 92, 1564 – 1569 (2002).
2. T. Thonhauser, G.D. Mahan, L. Zikatanov, J. Roe, Improved Supercooling in Transient Thermoelectrics, *Applied Physics Letters* 85(15), 3247 – 3249 (2004).
3. R.G. Yang, G.J. Chen, A.R. Kumar, G.J. Snyder, J.-P. Fleurial, Transient Cooling of Thermoelectric Coolers and its Applications for Microdevices, *Energy Conversion and Management* 46, 1407 – 1421 (2005).
4. L.M. Shen, H.X. Chen, F. Xiao, Y.X. Yang, S.W. Wang, The Step-Change Cooling Performance of Miniature Thermoelectric Module for Pulse Laser, *Energy Conversion and Management* 80, 39 – 45 (2014).
5. L.M. Shen, F. Xiao, H.X. Chen, S.W. Wang, Numerical and Experimental Analysis of Transient Supercooling Effect of Voltage Pulse on Thermoelectric Element, *Int. J. of Refrigeration* 35, 1156 – 1165 (2012).
6. M. Ma, J. Yu, A Numerical Study on the Temperature Overshoot Characteristic of a Realistic Thermoelectric Module under a Current Pulse Operation, *Int. J. of Heat and Mass Transfer* 72, 234 – 41 (2014).
7. J.N. Mao, H.X. Chen, H. Jia, X.L. Qian, The Transient Behavior of Peltier Junctions Pulsed with Supercooling, *J. of Applied Physics* 112(1), 014514-1-014514-9 (2012).

8. Chin-Hsiang Cheng, Shu-Yu Huang, Tsung-Chieh Cheng, A Three-Dimensional Theoretical Model for Predicting Transient Thermal Behavior of Thermoelectric Coolers, *Int. J. of Heat and Mass Transfer* 53, 2001 – 2011 (2010).
9. A.A. Snarskii, I.V. Bezsudnov, Rotating Thermoelectric Device in Periodic Steady State, *Energy Conversion and Management* 94, 103 – 111 (2015).
10. L.V. Hao, Xiao-Dong Wang, Tian-Hu Wang, Jing-Hui Meng, Optimal Pulse Current Shape for Transient Supercooling of Thermoelectric Cooler, *Energy* 83, 788 – 796 (2015).
11. M. Kotsur, Optimal Control of Distributed Parameter Systems with Application to Transient Thermoelectric Cooling, *Advances in Electrical and Computer Engineering* 15, 117 – 122 (2015).
12. M.P. Kotsur, Mathematical Simulation and Optimization of Nonsteady Thermoelectric Cooling Process, *Technology Audit and Production Reserves* 1, 2(27), 29 – 34 (2016).
13. E.K. Iordanishvili, B.E. Malkovich, On the Possibility of Temperature Control of Cold Thermoelement Junction, *Issues of Radioelectronics, Series Thermal Regimes, Temperature Control and Cooling of Electronic Equipment* 2, 74 – 81 (1971).
14. M.A. Kaganov, A.S. Rivkin, Reproduction of Given Time Variation of Temperature by Means of Semiconductor Thermoelements, *Journal of Engineering Physics and Thermophysics* 24(5), 902 – 907 (1973).
15. A.S. Rivkin, Optimal Control of Nonsteady Thermoelectric Cooling Process, *Technical Physics* 43(7), 1563 – 1570 (1973).
16. *Thermoelectric Coolers*, Ed.by A.A. Vainer (Moscow: Radio i Sviaz, 1983), 176p.
17. B.M. Goltsman, V.A. Kudinov, and I.A. Smirnov, *Semiconductor Thermoelectric Materials Based on Bi<sub>2</sub>Te<sub>3</sub>* (Moscow: Nauka, 1972), 320 p.

Submitted 31.10.2016



Rasit Ahiska

## Rasit Ahiska<sup>1</sup>, Gunay Omer<sup>2</sup>

Rasit Ahiska<sup>1</sup>, Gunay Omer<sup>2</sup>

<sup>1</sup>Department of Physics, Faculty of Science, Gazi University, 06500 Ankara, Turkey;

<sup>2</sup>TES Ltd Co., Ankara, Turkey



Gunay Omer

### THERMOELECTRICITY IN TURKEY

---

*The present paper provides information about Turkey. The high potential of Turkey in the field of solar, geothermal and wind energy and industrial waste heat is shown. The issues of incentives for investments in industry, power engineering, development works, the science of Turkey and new home productions are discussed. A survey of the current state of thermoelectric science and industry in Turkey is made, the prospects of development and all kinds of international cooperation for the progress of these technologies in Turkey are considered.*

**Key words:** Turkey, investments, thermoelectricity, cooperation.

#### Introduction

Turkey, officially called the Republic of Turkey, mainly in Anatolia, with a smaller portion in Europe, has a territory of total area 783.562 square kilometers. Turkey's location at the crossroads of Europe and Asia makes it a country of significant geostrategic importance. After defeating the occupying countries in the war for independence (1919 – 1922) in 1923, Mustafa Kemal Atatürk proclaimed the Republic of Turkey. Turkey is a democratic, multicultural, secular, unitary, constitutional republic. The majority of population professes Islam. Turkey as a member of the Council of Europe, NATO, the Organization for Economic Cooperation and Development (OECD), the Organization for Security and Cooperation in Europe (OSCE) and the G-20 group has been integrated into the western world. Since 1963 Turkey has been an associate member of European Economic Community, in 1995 joined the EU Customs Union, and in 2005 the European Union started negotiations with Turkey towards full membership in the EU. The country is also a member of the Turkish Council, the International Organization of Turkic Culture, the Organization of Islamic Cooperation and the Organization for Economic Cooperation. Today Turkey with its 80-million population, growing economy and active diplomatic initiatives is a recognized powerful regional state. With the gross domestic product 718,221 billion US dollars (2015), purchasing power parity 1.543 trillion US dollars (2015) and annual growth of gross domestic product 4 %, Turkey is the world's 16<sup>th</sup> powerful economy. Turkey is the largest Moslem economy in the world followed by Indonesia and Saudi Arabia [1].

The energy potential of Turkey for hydroenergy is 216 billion kW-h, geothermal energy - 31 500 MW, solar energy -500 Mtoe/year (million tons of oil equivalent), wind energy - 400 billion kW-h, respectively. In other words, according to the value of renewable energy sources, Turkey is in one of the most favourable regions of the world. At present, hydropower with its share of 41 % in total electricity production of Turkey is one of the most widely used renewable energy sources. By 2020 about 90 % of hydropower potential of Turkey is expected to be exploited. On the other hand, today from the geothermal resources in Turkey 20 MW of electric energy is generated. It is planned that in

2020 this value will increase to 1000 MW. In other words, in 2020 1 mln 250 thousand buildings will be heated by geothermal energy. On the other hand, as per the end of 2002 1.8 GW of electricity was produced from wind energy. It is planned that by 2025 7% of demand for electric energy will be covered at the cost of wind energy.

Although Turkey has a big potential in terms of using renewable energy sources, the share of renewable energy sources in total volume of energy production is very low. Nevertheless, biomass energy of renewable energy sources is of great importance due to very high proportion in total volume of energy production. In fact, total energy demand of the country making 77 044 Mtoe/year and annual energy demand in 2010 175 054 Mtoe prove to be lower than the potential of renewable energy sources.

The infrastructures of renewable energy sources in Turkey received the official status in 2005, when the Renewable Energy Law was issued, and for harmonization of actions with the EU there was adopted the National Renewable Energy Action Plan (LEAP) for the period of 2011 – 2020 [2]. According to this plan, by 2023 22 % of electric energy will be produced by hydroelectric power stations of Turkey (but the amount will be much greater due to greater total amount), and 16 % will be produced from other renewable energy sources. According to LEAP, in transport sector 10 % of energy will be produced from renewable energy sources. According to plan, the energy of wind will increase from 3 GW to 20 GW, and solar energy will increase to 5 GW. In 2013 Turkey exceeded the average world level in energy production from the renewable energy sources. While the average world level was as low as 22 %, in Turkey this figure reached 29 % [3]. By the end of 2015 32.5 % of electric energy in Turkey had been produced from renewable energy sources. In the same year 25.8 % of energy was produced by hydro power plants, 4.4 % from wind energy, 1.3 % from geothermal energy, 0.6 % from biogas and other sources, 0.4 % from solar energy [4].

According to Turkish Wind Atlas (REPA), at the height of 50 meters the Aegean Sea, Marmara Sea and eastern mediterranean regions are regarded as the places with high wind energy potential. For wind velocities over 7 m/s the wind energy potential in Turkey is set at the level of 47.849 MW. Wind electric energy production and its connection to Turkish power grid started in 1998. Since 2005, especially after the adoption of Renewable Energy Law, electric energy production constantly increases and by now global growth rate has been achieved. In Turkey, by the end of 2015 the volume of wind energy production made 11.552 GWh. By the end of 2015 the installed capacity of wind power plants for operation was 4.503 MW [5].

According to Atlas of Solar Energy Potential (GEPA) prepared by Turkish Ministry of Energy, the annual time of sunlight is 2.737 hours (on the average 7.5 hours daily), the annual amount of solar energy is 1.527 kWh/m<sup>2</sup> (on the average 4.2 kWh/m<sup>2</sup> daily). It was determined that in 2012 the total installed area of solar collectors was about 18.640.000 square meters. The annual production of flat-plate solar collectors was 1.164.000 m<sup>2</sup>, vacuum tube collectors - 57.600 square meters. 50 % of produced flat-plate collectors and 100 % of vacuum tube collectors were realized in the domestic market of Turkey. In 2012 by means of solar collectors there was produced about 768.000 toe of thermal energy. In the same year from this thermal energy 500.000 toe were used for heating of dwellings, and 268.000 toe – for industrial application. With creation of unlicensed solar power stations, by the end of 2015 electric energy production reached the capacity of 248.8 MW. According to Turkish Ministry of Energy, in 2023 the licensed solar power stations will reach the capacity about 3000 MW. Today for the potential and direct usage of geothermal energy Turkey ranks second in Europe and fifth in the world. By the results of 2005 the potential of geothermal energy production in Turkey, with the annual use 24.839.9TJ/year or power factor 0.5 for 6900.5 GWh/year, was 1495 MW [6].

## **Investments in Turkey**

In the volume and scope of investments, primarily in scientific-technological and innovative implementations, as well as investments in industry, agriculture, defence, science and culture Turkey is one of the leading countries of the world. To attract international and domestic investors to Turkey, the state and government of the country have prepared the legal infrastructure and brought to readiness the government and private sectors of the country. The investment strategy of Turkey is to provide full technological, economic and political independence due to development of local production and creation of new industries. Investments in Turkey are supported by various means. Among them, creation of Free Economic Zones has top priority. According to the latest data of the Ministry of Economy of the Republic of Turkey, in 21 zones about 50.000 companies from hundreds of different countries manufacture various goods and services for the domestic and world market. These companies are provided with the following privileges:

1. Privileged position in the domestic market of Turkey for major manufacturers.
2. Low cost for plots of land and labour force in free trade zone.
3. Free transfer of international revenue and profit.
4. Exemption from tax on profit government tax.
5. Exemption from VAT for tax on profit.
6. Absence of legal restrictions on the foreign trade.
7. The use of any converted currency.
8. Duty-free imported goods.
9. Easy access to Turkish ports.
10. Exemption from taxes on bank operations.
11. No restrictions on the quality of products and prices of goods.
12. Unlimited participation of foreign capital in investments.
13. Provision of ready, modern workplaces with a good infrastructure for production and business.
14. A ban on the strike and lockout.
15. Removal of restrictions on the terms of stay of any product in free trade zone.
16. Granting of privileges to all companies irrespective of their affiliation [7].

At the top of measures by the Ministry of Science, Industry and Technology of Turkey to support investments and local mass production is Teknoyatirim grant for domestic companies. According to the Ministry, in the framework of Teknoyatirim grant the program of investments in high-technology products is funded. This program supports the investments from natural and legal persons of Turkey engaged in research activity, as well as in the introduction of the results of these works in the form of a patent or novel high-technology products. Within the program of investments in high-technology products today the Ministry in 26 provinces has concluded 204 contracts on the projects. 35 projects of them have been successfully completed, and the companies have obtained from the state free of charge 15.256.138.98 TL for the purchase of machines and equipment.

To scientists and postgraduates working on the dissertations including industrial introductions and to companies introducing these new inventions and technologies to local industry, the Ministry lends very big financial support. This grant is called SANTEZ and its budget volume is 500.000TL - 1.000.000TL. Moreover, the Ministry for young businessmen with condition of creation of a new private company for the purpose of realization of a new project according to Teknogirişim program immediately and without compensation grants to a businessman 100.000 TL. Similar programs also exist in the other ministries of Turkey. There is a peculiar competition between different ministries [8].

In Turkey, the greatest support to research activities, the acquisition and implementation of

patents is offered by TÜBİTAK. TÜBİTAK grants are grouped into six programs. These include grants for scientists or grants for companies that are grouped into two programs: ACADEMIC, including national programs, international programs, programs for guest researchers and other programs, and INDUSTRIAL, including national programs, international partner programs and other programs. Academic national programs are grouped into 11 grants. The terms of these grants vary from 12 to 36 months, and the budget – from 30.000TL to 2.500.000TL. Academic international programs include three grants. Academic programs for guest researchers include two grants. Under these grants, foreign guest researchers receive full medical and other insurances and are paid high salaries. Industrial national programs are grouped into 13 grants. The terms of these grants vary from 12 to 36 months, and the budget - from 500.000TL to 5.000.000TL. Industrial international partner programs are grouped into 2 grants. Moreover, companies engaged in research activities are offered very big tax and other discounts [9].

### **Thermoelectric research in Turkey**

It is fair to say that the basic research in the field of heat pipes and thermoelectricity in Turkey dates back to 1992, when the family of a Turkish scientist Ahiska working on these issues returned to its historical homeland. The first peak of thermoelectric activities in Turkey was election of the first and so far the only Turkish scientist a corresponding member of the International Thermoelectric Academy during the XIII Forum held in 2009 in Kyiv. The first thermoelectric investigations represented as thermoelectric projects in the annual interlyceum project competitions organized by TÜBİTAK were a great success in Turkey. The thermoelectric projects of 1992 – 2007 without exception always won the first or second places, and these projects represented Turkey at Science Festivals in the USA or other countries. In 1993, for the first time in Turkey, an international patent was received on medical device for thermoelectric cooling of human brain. Flexible technology of thermoelectric module patented in this medical device is an important event not only for Turkey, but for the whole world. Founded in 1999 at Gazi University, Ankara, the first and only in Turkey research Thermoelectric & Heat Pipe Laboratory raised the quality of scientific and technical research in the field of thermoelectricity and heat pipes to the university level. In this laboratory, by 2013 dozens of dissertations had been prepared, hundreds of papers had been published, dozens of projects and patents had been done [10 – 48]. Since 2013 this work continues at Department of Physics of Gazi University. Here, for the first time in Turkey, such lectures as Physics of Thermoelectricity 1 and 2, Physics of Heat-Exchange Systems 1 and 2, Patent Preparation Rules were organized for students, and for post-graduates - such lectures as Theory of Thermoelectric Module and Devices and Bulk and Nano Thermoelectric Materials. Here again was created Thermoelectric & Heat Pipe Laboratory. At the cost of state Teknogirişim grant the first and only thermoelectric company TES Ltd was founded in 2010 in Turkey. Thus, the foundations for new industrial branches of thermoelectricity and heat pipes were laid in Turkey. Unfortunately, such extensive and comprehensive studies as performed by Gazi University and company TES Ltd., are very few in Turkey. However, with the onset of state investments in semiconductor and thermoelectric technologies, with every passing day the number of scientists involved in these fields in Turkey increases considerably, as well as the number of projects, published papers and obtained patents. The research geography also expands. Today, besides Gazi University, thermoelectric studies are pursued at Tokat University, Hitit University of Çorum, Istanbul Technical University, Sakarya University, Erdogan University in Rize, Pamukkale University in Denizli and other universities of the country. A number of university and research projects financially

supported by TÜBİTAK are implemented and carried out there.

The first project in the field of thermoelectricity that obtained a grant from the Turkish state was TTGV138 project for thermoelectric material preparation and use for creation of medical device Thermohypotherm for cooling of human brain. The project duration was 1993-1995 and its budget - 600.000 \$. Although the grant was won, no funding was allocated. Despite this, the Thermohypotherm device was fabricated and received a European patent.



Fig. 1. The first project and patent in the field of thermoelectricity that obtained a grant from the Turkish state. Medical device Thermohypotherm for cooling of human brain.

The first international project of Gazi and Ivano-Frankivsk Universities “New Semiconductor Materials On The Base Of Lead Telluride For Thermoelectric Energy Transformers, 01.05.2010 – 01.05.2012” won a grant from TÜBİTAK. The second international Turkish-Ukrainian project was NATO project with a budget of 239.000 EUR “Thermoelectric Materials and Devices for Increasing of Energy Saving and Security”, SPS964536, 12.02.2013 – 30.06.2016.



Thermoelectric Materials and Devices for Energy Saving and Security Increase

**Brief details**

Project title: **Thermoelectric Materials and Devices for Energy Saving and Security Increase**

Duration: **24 month**

Institutions:

 **NATO country** - Gazi University / TES Ltd (Ankara, **Turkey**);  
 **NATO partner country** – Vasyl Stefanyk Precarpathian National University (Ivano-Frankivsk, **Ukraine**)

Budget:

NATO Funding Envelope Requested (ceiling)			
By Year		By Category	
Year 1	€ 121 200	Equipment	€ 144 400 (60.4%)
Year 2	€ 117 800	Training/Stipends	€ 24 400 (10.2%)
		Implementation	€ 70 200 (29.3%)
<b>NATO Total Funding</b>			<b>€ 239 000</b>
Non-NATO Funding			€ 80 000

( 31 )

Fig. 2. Turkish-Ukrainian project NATO/SPS964536.

The second big grant from the Turkish Republic allotted for the development of high thermoelectric technologies and heat pipe technologies and products is Teknogirişim grant from the Ministry of Industry for the project “Thermoelectric solar panel” for the amount of 75.000 TL. Thus, in 2010 in Turkey the first and only thermoelectric company TES Ltd. was founded and started to work.



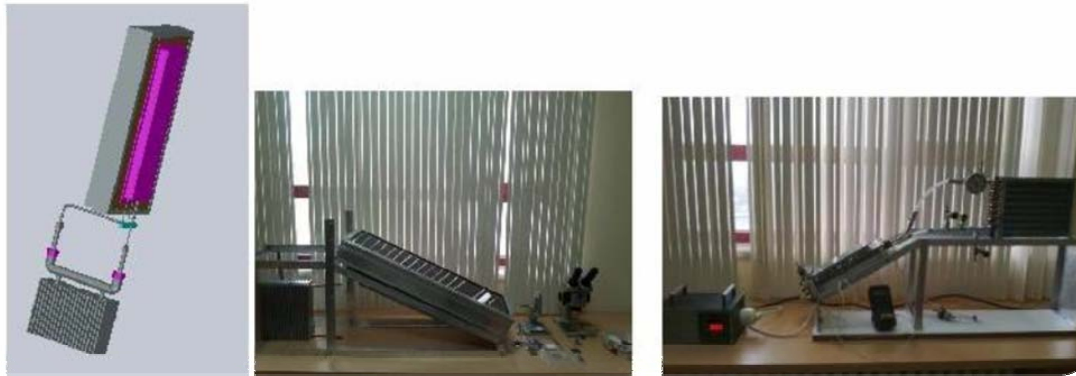


*Fig. 3. Thermoelectric solar panel of company TES Ltd created in 2010 with the support of a grant from the Republic of Turkey.*

Creation of company TES Ltd marked a new stage in the development of high thermoelectric technologies and heat pipe technologies. Since the beginning of the company activities all the projects have been funded by the state and TES Ltd.



*Fig. 4. Company TES Ltd created in 2010 by the grant from the Republic of Turkey.*

The first project funded by Ministry of Industry and company TES Ltd. was SANTEZ project “Production and Introduction of Computer-Controlled Thermoelectric Generator, 94.160TL, 2011 – 2012”. After its successful completion, the project continues, now in the framework of Teknoyatirim grant, 1.000.000TL, (2015 – 2018).



*Fig. 5. SANTEZ and Teknoyatirim Projects funded by the Ministry of Industry (Turkey) and company TES Ltd.*

The first project funded by TÜBİTAK and company TES Ltd. was “Development of thermoelectric solar panel, thermoelectric material and modules”, 880.000TL, 2013 – 2015.

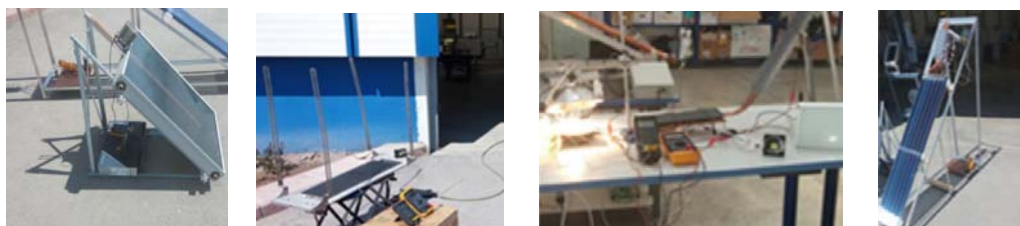


*Fig. 6. Joint project of TÜBİTAK and company TES Ltd “Development of thermoelectric solar panel, thermoelectric material and modules”.*

The second project funded by TÜBİTAK and company TES Ltd was “Thermoelectric minibar with a heat pipe”, 236.000 TL 2015 – 2016.



*Fig. 7. Joint project of TÜBİTAK and company TES Ltd “Thermoelectric minibar with a heat pipe”.*

The second project funded by the Ministry of Industry (KOSGEB – Small and Medium Enterprises Development Organization) and company TES Ltd. was “Desktop thermoelectric ice generator, 150.000 TL, 2014 – 2015”. According to the results of the project, a patent for ice generator was obtained in 2017, the costs of which were paid by TÜBİTAK under the patent grant.



*Fig. 8. Joint project of the Ministry of Industry (KOSGEB – Small and Medium Enterprises Development Organization) and company TES Ltd “Desktop thermoelectric ice generator”.*

Besides the above projects, Gazi University and company TES Ltd continue investigations and works on many projects, such as thermoelectric boiler, thermoelectric solar pump, thermoelectric utilizer of waste heat, transport thermoelectric liquid cooler, thermoelectric CPU cooler with a heat pipe, TEPAS instrument for testing of cooling modules and TEGPAS instrument for testing of generator modules.

### **Concluding remarks**

Turkey, with its millennial statehood, booming economy, young and dynamic population, investments in all spheres of activity, especially in science, industry and new technologies, location at the crossroads of Europe and Asia giving the country an important geo-strategic advantage is a

powerful country. All state institutions and organizations lend material and moral support to development of science, culture, industry, local production, bilateral and multilateral cooperation that provided the figures bringing Turkey to one of the first places in the world. Such situation is observed in all the spheres, as well as in thermoelectric and heat pipes technology. This position is confirmed with growing support in these fields in recent years. Taking into account these realities, for scientists and companies investments in new technologies, such as thermoelectric and heat piles technologies, participation in various joint scientific grants will be a correct and cost-effective decision. Election of a Turkish scientist to the International Thermoelectric Academy and the existence of thermoelectric company are a big benefit for cooperation between the Academy members and Turkey.

The present work was supported by TÜBİTAK grant 1511/1120014 and NATO grant SFP/984536.

## References

1. <https://tr.wikipedia.org>
2. <http://www.tuik.gov.tr>
3. "Turkey". International Monetary Fund. 7 Mayıs 2016 tarihinde kaynağından arşivlendi. Erişim tarihi: 2 Kasım 2014.
4. <http://www.tuik.gov.tr/PreHaberBultenleri.do?id=18616>
5. CIA. 4 Mart 2016 tarihinde kaynağından arşivlendi. Erişim tarihi: 28 Mayıs 2014.
6. "2015 Human Development Report". 15 Aralık 2015. 17 Haziran 2016 tarihinde kaynağından arşivlendi. Erişim tarihi: 15 Aralık 2015.
7. [www.ekonomi.gov.tr](http://www.ekonomi.gov.tr)
8. <http://www.sanayi.gov.tr>
9. <http://www.tubitak.gov.tr>
10. TES Ltd., Masaüstü Termoelektrik Buz Makinesi (2017), Patent No: 2014/14588
11. G. Omer, A.H. Yavuz, and R. Ahıska, Heat Pipes Thermoelectric Solar Collectors for Energy applications, *International Journal of Hydrogen Energy*, 2017, Accept
12. R. Ahıska, Organizmayı sıcaklıkla etkilemek için termoelektrik tıp cihazı (1993), Patent No: 26708.
13. Serkan Dişlitaş, Raşit Ahıska, Üç ayrıklı ölçüme dayalı parabol algoritması ile termoelektrik modülün  $I_{max}$   $V_{max}$  ve  $E_{max}$  parametrelerinin belirlenmesi, *Journal of the Faculty of Engineering and Architecture of Gazi University* **31**(4), 1063 – 172 (2016)
14. R. Ahıska, The Thermoelectric Solar Panels, *Journal of Vasyl Stefanyk Precarpathian National University* **3**(1), 9 – 14 (2016)
15. Raşit Ahıska, Hayati Mamur, Development and Application of a New Power Analysis System for Testing of Geothermal Thermoelectric Generators, *International Journal of Green Energy* **13**(7), 672 – 681 (2016)
16. Raşit Ahıska, Phase Content and Thermoelectric Properties of Optimized Thermoelectric Structures Based on the Ag Pb Sb Te System, *Journal of Electronic Materials* **45**(3), 1576 – 1583 (2016)
17. Abdullah Hakan Yavuz, Raşit Ahıska, Load and No Load Tests of the Thermoelectric Brain Cooler Designed for Brain Hypothermia, *Proc. of The Fifth Intl. Conf. On Advances in Applied Science and Environmental Technology - ASET 2016*, 1(15)

18. Hayati Mamur, Raşit Ahıska, Application of a DC DC Boost Converter with Maximum Power Point Tracking for Low Power Thermoelectric Generators, *Energy Conversion and Management* **97**, 265 – 272 (2015)
19. Hayati Mamur, Raşit Ahıska, A Review of Thermoelectric Generators in Renewable Energy, *International Journal of Renewable Energy Research* **4**(1), 128 – 136 (2014).
20. Raşit Ahıska, Dmytro Freik, Taras Parashchuk, and Igor Gorichok Igor, Quantum Chemical Calculations of the Polymorphic Phase Transition Temperatures of ZnS, ZnSe and ZnTe Crystals, *Turkish Journal of Physics* **38**(1), 125 – 129 (2014)
21. Raşit Ahıska, Hayati Mamur, Design and Implementation of a New Portable Thermoelectric Generator for Low Geothermal Temperatures, *IET Renewable Power Generation* **7**(6), 700 –706 (2013)
22. Raşit Ahıska, Hayati Mamur, A Test System and Supervisory Control and Data Acquisition Application with Programmable Logic Controller for Thermoelectric Generators, *Energy Conversion and Management* **64**, 15 – 22 (2012)
23. Raşit Ahıska, Serkan Dişlitaş, and Günay Ömer Günay, A New Method and Computer Controlled System for Measuring the Time Constant of Real Thermoelectric Modules, *Energy Conversion and Management* **53**(1), 314 – 321 (2012)
24. Raşit Ahıska, Serkan Dişlitaş Serkan, Computer Controlled Test System for Measuring the Parameters of the Real Thermoelectric Module, *Energy Conversion and Management* **52**(1), 27 – 36 (2011)
25. Ayşe Demirhan, Ahmet Memduh Kaymaz, Raşit Ahıska, and İnan Güler, A Survey on Application of Quantitative Methods on Analysis of Brain Parameters Changing with Temperature, *Journal of Medical Systems* **34**(6), 1059 – 1071 (2010)
26. Raşit Ahıska, Kenan Ahıska, New Method for Investigation of Parameters of Real Thermoelectric Modules, *Energy Conversion and Management* **51**(2), 338 – 345 (2010)
27. Raşit Ahıska, Kenan Ahıska, and Günay Ahıska, Analysis of a New Method for Measurement of Parameters of Real Thermoelectric Module Employed in Medical Cooler for Renal Hypothermia, *Instrumentation Science & Technology* **37**(1), 102 – 123 (2009)
28. Abdullah Hakan Yavuz, Raşit Ahıska, and Mahmut Hekim, Modeling of a Thermoelectric Brain Cooler by Adaptive Neuro Fuzzy Inference System, *Instrumentation Science & Technology* **11**, 636 – 655 (2008). (Yayın No: 2109665)
29. Raşit Ahıska, Abdullah Hakan, and Kaymaz Mehmet Kaymaz, Control of a Thermoelectric Brain Cooler by Adaptive Neuro Fuzzy Inference System, *Instrumentation Science & Technology* **36**(6), 636 – 655 (2008), Doi: 10.1080/10739140802451287 (Yayın No: 2105747)
30. Raşit Ahıska, New Method for Investigation of Dynamic Parameters of Thermoelectric Modules, *Turk J Elec Engin* **15**(1), 51 – 65 (2007). (Yayın No: 2102295)
31. Metin Kapıdere, Raşit Ahıska, and İnan Güler İnan (2005). A New Microcontroller Based Human Brain Hypothermia System, *Journal of Medical Systems* **29**(5), 501 – 512 (2005)
32. Nihal Fatma Güler, Raşit Ahıska, Design and Testing of a Microprocessor Controlled Portable Thermoelectric Medical Cooling Kit, *Applied Thermal Engineering* **22**(11), 1271 –1276 (2002)
33. Ihor Horichok, Raşit Ahıska, Dmytro Freik, Luybomyr Nykyruiy, Stepan Mudry, Ostap Matkivskiy, and Taras Semko, Phase Content and Thermoelectric Properties of Optimized Thermoelectric Structures Based on the Ag Pb Sb Te System, *Journal of Electronic Materials* **1 – 7** (2000)
34. Lubomir Nykyruiy, Dmytro Freik, Raşit Ahıska, Oleg Matkivskiy, Igor Lishchynskiy, and Igor

- Hryhoruk Igor, Composite Thermoelectric Materials on the Base of *PbTe* with *Ag* and *ZnO* Nanoinclusions, *5th Polish Forum Smart Energy Conversion & Storage (2015)* (Tam Metin Bildiri)(Yayın No:2109066)
35. Raşit Ahıska, Dmytro Freik, Ivan Lishchynskyy, and Igor Chavjak, Growth Processes Structure and Thermoelectric Properties in *SnTe* Based Vapor Phase Nanocondensates. *34th Annual International Conference on Thermoelectrics (ICT 2015) and 13th European Conference on Thermoelectrics (ECT 2015) (/)*(Yayın No:2169846)
36. Raşit Ahıska, Lubomir Nykyruy, and Feride Ahıska, Comparison of Thermoelectric and Fotovoltaic Solar Panels, *XVI International Forum on Thermoelectricity (2015)* (Tam Metin Bildiri/)(Yayın No:2107936)
37. Raşit Ahıska, Dmytro Freik, Ivan Chavjak, Lubomir Nykyruy, and Misha Mazur, Doping Semiconductors on the Base of IV VI for Thermoelectric International Conference of Physics and Technology of Thin Films and Nanosystems. *International Conference on the Physics and Technology of Thin Films and Nanosystems ICPTTFN-XV (2015)* (Tam Metin Bildiri/)(Yayın No:2108673)
38. Raşit Ahıska, Lyubomyr Nykyruy, Ivan Chavjak, and Natalia Freik, *The Influence of the Surface on the Thermoelectric Properties of SnTe Bi Thin Films, Science and Applications of Thin Films, Conference & Exhibition (2014/)*(Yayın No:2113184)
39. Raşit Ahıska, Lyubomyr Nykyruy, and Dmytro Freik, Quantum Size Oscillations of Thermoelectric Characteristics in IV VI Semiconductor Nanostructures, *Science and Applications of Thin Films, Conference & Exhibition, SATF 2014 (/)*(Yayın No:2113400)
40. Dmytro Freik, Lyubomyr Nykyruy, Raşit Ahıska, and Lyubov Mezhylovska, Processes of Structure Formation and Thermoelectric Properties of the Semiconductor Systems *Pb Sn Sb Bi Te*, *XII International Conference on Nanostructured Materials (NANO 2014) (/)*(Yayın No:2112910)
41. Raşit Ahıska, Lyubomyr Nykyruy, Dmytro Freik, Lyubov Mezhylovska, Ihor Horichok, Yuri Khalavka, and Kenan Ahıska, Thermoelectric Composites on the Base of *PbTe* with Nanoiclusions of Colloidal *Ag*, *International Conference on Thermoelectrics - ICT2014 (/)*(Yayın No:2112470)
42. Lyubomyr Nykyruy, Dmytro Freik, Lyubov Mezhylovska, Raşit Ahıska, and Volodymyr Potyak, *Pb Sb Bi Te*, Thin Film Condensates for Thermoelectric Application, *International Conference on Thermoelectrics - ICT2014 (/)*(Yayın No:2111997)
43. Raşit Ahıska. Hayati Mamur, and Metin Uliş, Modelling and Experimental Study of Thermoelectric Module as Generator, *Journal of the Faculty of Engineering and Architecture of Gazi University* **26**(4), 889 – 896 (2011), Atif Sayısı: 8 (Kontrol No: 2104813)
44. Raşit Ahıska, Mamur Hayati, and Metin Uliş, Termoelektrik Modülün Jeneratör Olarak Modellenmesi Ve Deneysel Çalışması, *Gazi Üniversitesi Mühendislik-Mimarlık Fakültesi Dergisi* **26**(4) (2011) (Kontrol No: 2110090)
45. Raşit Ahıska, Ugur Fidan, Serkan DişlitaşSerkan (2008). The Influence Of The Different Temperature Control Systems On The Thermoelectric Medicine Kıt S Performance, *Journal of The Faculty of Engineering and Architecture of Gazi University* **23**(1), 441 – 447 (2008), Atif Sayısı: 1 (Kontrol No: 2109447)
46. Raşit Ahıska, Kenan Ahıska, Esnek İki Fazlı Termoelektrik Cpu Soğutucusu, *Gazi Üniversitesi Mühendislik-Mimarlık Fakültesi Dergisi* **22**(2), 25 – 35 (2007). (Kontrol No: 2110819)
47. Raşit Ahıska, Serkan Dişlitaş, Microcontroller Based Thermoelectric Generator Application,

- GU Journal of Science* **19**(2), 135 – 141 (2006), Atıf Sayısı: 14 (Kontrol No: 2101608)
48. Raşit Ahıska, Bünyamin Ciylan, Yılmaz Savaş, and İnan Güler, Standart termoelektrik modülün Z parametresinin ölçülmesi için yeni yöntem ve yeni sistem, *Gazi Üniversitesi Mühendislik-Mimarlık Fakültesi Dergisi* **19**(4), 467 – 473 (2004), Atıf Sayısı: 10 (Kontrol No: 2104436)
49. Raşit Ahıska, İnan Güler, and Yılmaz Savaş, Termoelektrik soğutucunun özelliklerinin araştırılması, *Politeknik Dergisi* **2**(3), 89 – 94 (1999), Atıf Sayısı: 9 (Kontrol No: 2104603)

Submitted 07.10.2016



P.V. Gorskiy

P.V. Gorskiy<sup>1,2</sup>

<sup>1</sup>Institute of Thermoelectricity of the NAS and MES Ukraine,  
Nauky str., Chernivtsi, 58029, Ukraine;  
Yu.Fedkovich Chernivtsi National University,  
<sup>2</sup>Kotsyubynsky str., Chernivtsi, 58012, Ukraine

## LATTICE THERMAL CONDUCTIVITY OF THERMOELECTRIC MATERIALS BASED ON Zn-Cd-Sb

---

*Formulae for the components of the lattice thermal conductivity tensor of rhombic thermoelectric materials are derived. In the process of calculations, phonon-phonon scattering due to both normal processes and umklapp processes, is taken into account. Both the anisotropy of the sound velocity and the anisotropy of the Gruneisen tensor are taken into account. For the calculation of phonon relaxation time an approximation is used wherein this time, though anisotropic, depends on phonon frequency as a whole, rather than on the individual components of its quasi-momentum. The results of calculations are involved for the interpretation of experimental data on thermal conductivity anisotropy of cadmium and zinc antimonides. Comparison of the obtained results to the experimental data and other model theoretical approaches shows that when evaluating thermal conductivity anisotropy of rhombic crystals of cadmium and zinc antimonides one should take into account the anisotropy of the Gruneisen parameters and sound velocities, as well as frequency dependence of phonon relaxation time. However, as the Debye temperatures, their "scalar" values, determined by the calorimetric method, should be used, and not the components of the corresponding tensors determined on the basis of X-ray diffraction studies. Then it turns out that the "umklapp coefficient" which determines the frequency dependence of the intensity of the interphonon collisions due to the corresponding processes is also anisotropic. A fairly good agreement of the theoretical ratio of the components of the lattice thermal conductivity tensor of cadmium antimonide with the experimentally observed ratio of the components of the total thermal conductivity tensor indicates that the anisotropy of the lattice component of the thermal conductivity of cadmium antimonide is close to the anisotropy of the component due to free charge carriers.*

**Key words:** cadmium antimonide, zinc antimonide, symmetry, phonon spectrum, anisotropy, phonons, normal processes, umklapp processes, Gruneisen tensor, lattice thermal conductivity.

### Introduction

Despite the fact that currently bismuth telluride and alloys based on it are the dominant thermoelectric materials, there is an aspiration to replace them with other materials that do not contain tellurium. The need for a gradual abandonment of tellurium as a component of thermoelectric materials is due to a number of factors. Among them, mention should be made, in particular, of the high cost of tellurium, its limited production and reserves, its toxicity for living organisms and the environment, and the inoperability of materials based on the Bi (Sb)-Te (Se) system at high temperatures. At the same time, these shortcomings are lacking, for example, in cadmium and zinc antimonides. At room and lower temperatures, the thermoelectric figure of merit of these materials is low, so they are not used for the manufacture of thermoelectric coolers. However, they could be regarded as a worthy competitor to tellurium-containing materials as "generator" materials, since in

the range of 400 – 600 K their thermoelectric figure of merit sharply increases, and, moreover, can be substantially increased through optimization due to doping with a number of impurities in the appropriate concentrations [1].

It should be noted that thermoEMF anisotropy of cadmium and zinc antimonides, as well as possible origination in them of transverse thermoEMF, including due to thermal conductivity anisotropy, allows using these materials, especially cadmium antimonide, for the manufacture of anisotropic, including optical, thermoelements [2].

In view of the foregoing, the purpose of this paper is theoretical analysis of the mechanism of origination of lattice thermal conductivity anisotropy of rhombic crystals and application of the results to estimate of lattice thermal conductivity anisotropy of zinc and cadmium antimonides.

### **Analytical calculation of lattice thermal conductivity of rhombic crystals and discussion of the results**

Cadmium antimonide *CdSb*, as well as zinc antimonide *ZnSb*, is an orthorhombic crystal of group  $D_{2h}^{15}$ . The first Brillouin zone of these crystals is a rectangular parallelepiped, due to which the tensors of kinetic coefficients of these crystals in the absence of a magnetic field are diagonal, and each of them has, generally speaking, three independent and different components. The same symmetry property is typical of: sound propagation velocity in these crystals, the Gruneisen parameter characterizing the degree of influence of deformations, hence, of the anharmonism of lattice vibrations on the energy spectrum of phonons, the Debye temperature determined from X-ray diffraction studies, as well as umklapp parameter characterizing dependence of the possibility of interphonon collisions with umklapp on phonon frequency. At the same time, the Debye temperature, determined by calorimetric method, just as the specific heat of crystal, is a scalar. Based on these considerations, let us derive formulae which determine components of lattice thermal conductivity tensor of orthorhombic crystals.

Let us start with the calculation of  $\kappa_{111}$  component. We proceed from the general formula of thermal conductivity given in [3], according to which this component is equal to:

$$\kappa_{111} = \int_0^{\omega_D} \rho v_{1g}^2 \tau_{11}(\omega) dc_V(\omega). \quad (1)$$

In this formula:  $\rho$  – crystal density,  $v_{1g}$  – group sound velocity along the corresponding axis,  $\tau_{11}(\omega)$  – depending on phonon frequency as a whole, component of relaxation time tensor,  $dc_V(\omega)$  – differential contribution to crystal heat capacity at a constant volume.

To calculate the lattice thermal conductivity of a crystal from Eq. (1), it is also necessary to specify the model phonon spectrum of an orthorhombic crystal. Since in the Debye approximation the phonon spectrum of an isotropic crystal is linear with respect to the quasimomentum modulus, it is clear that in the simplest approximation for an orthorhombic crystal it can have, for example, the form:

$$\omega(\vec{k}) = \sqrt{v_1^2 k_1^2 + v_2^2 k_2^2 + v_3^2 k_3^2}, \quad (2)$$

In this formula,  $v_1, v_2, v_3$  – phase sound velocities in the directions of principal crystallographic axes,  $k_1, k_2, k_3$  – components of quasi-momentum along the same axes. Therefore, formula (1) can be transformed as follows:



$$\kappa_{l11} = \int_0^{\omega_D} \frac{M}{V} v_1^2 \tau_{11}(\omega) d\left(\frac{dE}{MdT}\right) = \frac{\hbar^2}{(kT)^2} \int_0^{\omega_D} \Gamma_{pl1}(\omega) \tau_{11}(\omega) \frac{\omega^2 \exp(\hbar\omega/kT)}{[\exp(\hbar\omega/kT) - 1]^2} d\omega, \quad (3)$$

where

$$\begin{aligned} \Gamma_{pl1}(\omega) &= \iiint v_1^2(\vec{k}) \delta(\omega - \omega(\vec{k})) d\tau_{\vec{k}} = \iiint \frac{v_1^4 k_1^2}{(2\pi)^3 (v_1^2 k_1^2 + v_2^2 k_2^2 + v_3^2 k_3^2)} \times \\ &\times \delta\left(\omega - \sqrt{v_1^2 k_1^2 + v_2^2 k_2^2 + v_3^2 k_3^2}\right) dk_1 dk_2 dk_3 = \iint \frac{2v_1 \sqrt{\omega^2 - (v_2^2 k_2^2 + v_3^2 k_3^2)}}{(2\pi)^3 \omega} dk_2 dk_3 = \\ &= \frac{v_1}{4\pi^3} \int_0^{\omega} \frac{\sqrt{\omega^2 - \omega_1^2} 2\pi \omega_1 d\omega_1}{\omega v_2 v_3} = \frac{v_1 \omega^2}{6\pi^2 v_2 v_3}. \end{aligned} \quad (4)$$

In formula 3,  $M$  is crystal mass,  $V$  is crystal volume.

The relaxation time of longitudinal phonons in normal scattering in accordance with the procedure developed in [4] for an orthorhombic crystal can be represented in the following form

$$\tau_{pl1}(\omega) = \frac{3\pi v_c^5 \rho}{16\gamma_{11}^2 k_B T \omega^4} = \frac{3\pi \rho (v_1 v_2 v_3)^{5/3}}{16\gamma_{11}^2 k_B T \omega^4}. \quad (5)$$

In this formula,  $v_c = \sqrt[3]{v_1 v_2 v_3}$ ,  $\gamma_{11}$  – the Gruneisen tensor component.

However, normal processes occur with retention of full momentum of phonon subsystem and, therefore, they do not yield final value of lattice thermal conductivity. At the same time, in the temperature range typical for the application of "generator" thermoelectric materials (TEM), the umklapp processes play a decisive role, for which the frequency of interphonon collisions is proportional to the phonon frequency. Taking into account these processes in addition, as well as the contribution of transverse phonon legs, we find the following final expressions for the components of lattice thermal conductivity tensor:

$$\kappa_{l11} = \frac{\pi \rho \hbar}{32 \gamma_{11}^2 \theta^3 k_B T_D^2} \int_0^1 \frac{x^4 \exp(x/\theta) dx}{(\exp(x/\theta) - 1)^2} \left[ \frac{(v_{1l})^{8/3} (v_{2l} v_{3l})^{2/3}}{x^4 + \mu_{11} x} + \frac{2(v_{1l})^{8/3} (v_{2l} v_{3l})^{2/3}}{x(3.125\theta^3 + \mu_{11})} \right], \quad (6)$$

$$\kappa_{l22} = \frac{\pi \rho \hbar}{32 \gamma_{22}^2 \theta^3 k_B T_D^2} \int_0^1 \frac{x^4 \exp(x/\theta) dx}{(\exp(x/\theta) - 1)^2} \left[ \frac{(v_{2l})^{8/3} (v_{1l} v_{3l})^{2/3}}{x^4 + \mu_{22} x} + \frac{2(v_{2l})^{8/3} (v_{1l} v_{3l})^{2/3}}{x(3.125\theta^3 + \mu_{22})} \right], \quad (7)$$

$$\kappa_{l33} = \frac{\pi \rho \hbar}{32 \gamma_{33}^2 \theta^3 k_B T_D^2} \int_0^1 \frac{x^4 \exp(x/\theta) dx}{(\exp(x/\theta) - 1)^2} \left[ \frac{(v_{3l})^{8/3} (v_{1l} v_{2l})^{2/3}}{x^4 + \mu_{33} x} + \frac{2(v_{3l})^{8/3} (v_{1l} v_{2l})^{2/3}}{x(3.125\theta^3 + \mu_{33})} \right]. \quad (8)$$

In these formulae, through  $\gamma_{11}, \gamma_{22}, \gamma_{33}$  we denote the Gruneisen tensor components, and through  $\mu_{11}, \mu_{22}, \mu_{33}$  – the components of umklapp coefficients. Indexes  $l, t$  refer to the longitudinal and transverse legs, the components of the Gruneisen parameter tensors and the umklapp coefficients are assumed to be independent of the phonon polarization. Besides,  $T_D$  – caloric Debye temperature,  $\theta = T/T_D$ .

At high temperatures, when the Peierls law and the Leibfried-Schlemann formula are valid, formulae (6) – (8) go over into the following:

$$\kappa_{l11} = \frac{\pi\rho\hbar}{32\gamma_{11}^2\theta k_B T_D^2} \left[ (v_{1l})^{8/3} (v_{2l}v_{3l})^{2/3} F(\mu_{11}) + \frac{(v_{1t})^{8/3} (v_{2t}v_{3t})^{2/3}}{3.125\theta^3 + \mu_{11}} \right], \quad (9)$$

$$\kappa_{l22} = \frac{\pi\rho\hbar}{32\gamma_{22}^2\theta k_B T_D^2} \left[ (v_{2l})^{8/3} (v_{1l}v_{3l})^{2/3} F(\mu_{22}) + \frac{(v_{2t})^{8/3} (v_{1t}v_{3t})^{2/3}}{3.125\theta^3 + \mu_{22}} \right], \quad (10)$$

$$\kappa_{l33} = \frac{\pi\rho\hbar}{32\gamma_{33}^2\theta k_B T_D^2} \int_0^1 \left[ (v_{3l})^{8/3} (v_{1l}v_{2l})^{2/3} F(\mu_{33}) + \frac{(v_{3t})^{8/3} (v_{1t}v_{2t})^{2/3}}{3.125\theta^3 + \mu_{33}} \right]. \quad (11)$$

Function  $F(\mu)$  is determined as follows:

$$F(\mu) = \int_0^1 \frac{x dx}{x^3 + \mu}. \quad (12)$$

We apply these results to estimate the anisotropy of lattice thermal conductivity of zinc and cadmium antimonides. However, first of all, we note that in [5] the following relation was used to estimate the lattice thermal conductivity of rhombic crystals and its anisotropy:

$$\kappa_{lji} \propto T_{Di}^3 / \gamma_{ii}^2, \quad (13)$$

In this formula,  $T_{Di}$  – the Debye temperatures determined from X-ray diffraction data,  $\gamma_{ii}$  – the Gruneisen tensor components.

To compare our results with the results obtained within model (13) for *ZnSb*, we use the data given in Table [5].

Table

*Elastic constants (in the Voigt notation) and the Gruneisen tensor components of ZnSb single crystal*

$c_{11}$	$c_{22}$	$c_{33}$	$c_{44}$	$c_{55}$	$c_{66}$	$c_{12}$	$c_{23}$	$c_{13}$	$\gamma_{11}$	$\gamma_{22}$	$\gamma_{33}$
9.22	10.38	9.38	2.13	4.65	3.46	3.31	3.10	3.80	1.30	1.08	0.86

Elastic constants are given in units of  $10^{10}$  Pa.

Moreover, the Debye temperatures determined from X-ray diffraction data are equal to:  $T_{D1} = 223$  K,  $T_{D2} = 271$  K,  $T_{D3} = 283$  K.

Sound velocities for the longitudinal and transverse waves in orthorhombic crystal can be defined by the formulae:

$$\begin{aligned} v_{1l} = \sqrt{c_{11}/\rho}; v_{1t} = \sqrt{2c_{55}c_{66}/\rho(c_{55} + c_{66})}; v_{2l} = \sqrt{c_{22}/\rho}; v_{2t} = \sqrt{2c_{44}c_{66}/\rho(c_{44} + c_{66})}; \\ v_{3l} = \sqrt{c_{33}/\rho}; v_{3t} = \sqrt{2c_{44}c_{55}/\rho(c_{44} + c_{55})}. \end{aligned} \quad (14)$$

Taking into account that zinc antimonide density according to [6] is  $6380 \text{ kg/m}^3$ , we obtain the

following values of said velocities (in m/s):

$$\begin{aligned} v_{1l} &= 3.802 \cdot 10^3; v_{1t} = 2.494 \cdot 10^3; v_{2l} = 4.034 \cdot 10^3; \\ v_{3l} &= 2.033 \cdot 10^3; v_{3t} = 3.834 \cdot 10^3; v_{3t} = 2.140 \cdot 10^3. \end{aligned} \quad (15)$$

Using formula (13) for the estimate of thermal conductivity anisotropy we find that components of lattice thermal conductivity tensor of zinc antimonide correlate as 1.0:2.6:5.2.

However, the procedure used in [5] does not take into account either the contribution of transverse phonons or the fact that the temperature whereby said estimate is performed is not substantially higher than the Debye temperature, or sound velocity anisotropy in crystal. Therefore, we clarify the impact of these factors on lattice thermal conductivity anisotropy of *ZnSb*. Note that due to limited amount of experimental data on this matter we have to assume that “umklapp parameter”  $\mu$  is isotropic and, hence, thermal conductivity anisotropy is governed only by the anisotropy of sound velocity, the Gruneisen tensor and X-ray characteristic temperatures, if such are used in formulae (6) – (8) instead of isotropic caloric Debye temperature.

In this case, we select the value of the "umklapp parameter" from the requirement of "coincidence of theory with experiment", i.e. in such a way that thermal conductivity averaged over the directions, which, as can easily be shown, is equal to the "experimental" value given in the handbook [6]; i.e. 1.4 W/(m·K) at 293 K. Then, taking into account the above values of *ZnSb* parameters, we get  $\mu = 4.997$ , and, hence,  $\kappa_{111} = 0.968$  W/(m·K),  $\kappa_{122} = 1.256$  W/(m·K),  $\kappa_{133} = 1.977$  W/(m·K). These values correlate as 1:1.298:2.042, which is substantially lower than in conformity with formula (13).

If, however, we assume, as it is done in [5], that “experimental” value of thermal conductivity is equal to 2 W/(m·K) at 293 K, we obtain that  $\mu = 3.328$ , and, hence,  $\kappa_{111} = 1.375$  W/(m·K),  $\kappa_{122} = 1.800$  W/(m·K),  $\kappa_{133} = 2.826$  W/(m·K). These values correlate as 1:1.309:2.055, i.e. such a correction does not significantly change thermal conductivity anisotropy.

However, if in formulae (6) – (8) instead of X-ray characteristic temperatures we use isotropic caloric Debye temperature 225 K and assume “experimental” value of thermal conductivity equal to 1.4 W/(m·K) at 293 K, we get that  $\mu = 5.973$ , and, hence,  $\kappa_{111} = 0.821$  W/(m·K),  $\kappa_{122} = 1.301$  W/(m·K),  $\kappa_{133} = 2.078$  W/(m·K). These values correlate as 1:1.585:2.531. Strange as it may seem, within the framework of the above approach, the use of the isotropic Debye temperature slightly increases the expected anisotropy of the lattice thermal conductivity. The latter estimate of thermal conductivity anisotropy seems to be “most shrewd”, but a deviation from it may indicate, for instance, the anisotropy of umklapp coefficient  $\mu$ .

We now proceed to estimate of cadmium antimonide thermal conductivity anisotropy. Moduli of elasticity of cadmium antimonide at temperature 293 K in units  $10^{10}$  Pa are equal to [7]:  $c_{11[100]} = 7.97$ ;  $c_{22[010]} = 9.50$ ;  $c_{33[001]} = 8.40$ ;  $c_{44[001]} = 1.257$ ;  $c_{44[010]} = 1.259$ ;  $c_{55[001]} = 2.982$ ;  $c_{55[100]} = 2.997$ ;  $c_{66[010]} = 1.883$ ;  $c_{66[001]} = 1.867$ .

By virtue of this, with regard to cadmium antimonide density equal to 6900 kg/m<sup>3</sup> [7], the values of sound velocities in this single crystal along the principal directions are, respectively, equal to:  $v_{1l} = 3.399 \cdot 10^3$  m/s;  $v_{1t} = 1.828 \cdot 10^3$  m/s;  $v_{2l} = 3.711 \cdot 10^3$  m/s;  $v_{2t} = 1.477 \cdot 10^3$  m/s;  $v_{3l} = 3.489 \cdot 10^3$  m/s;  $v_{3t} = 1.602 \cdot 10^3$  m/s.

Components of the Gruneisen tensor of *CdSb* have the following values [7]:  $\gamma_{11} = 1.28$ ;  $\gamma_{22} = 0.48$ ;  $\gamma_{33} = 0.64$ . In so doing, the characteristic Debye temperatures are equal to:  $T_{D1} = 180$  K,  $T_{D2} = 215$  K,  $T_{D3} = 204$  K [7].

Guided by thermal conductivity value of *CdSb* given in [6] and equal to 1 W/(m·K), on the assumption of umklapp parameter isotropy, but with regard to the anisotropy of X-ray characteristic Debye temperatures, we get  $\mu = 7.256$ , and, hence,  $\kappa_{11l} = 0.696$  W/(m·K),  $\kappa_{22l} = 0.894$  W/(m·K),  $\kappa_{33l} = 1.41$  W/(m·K). These values of components of lattice thermal conductivity tensor correlate as 1:1.284:2.026. Using caloric isotropic Debye temperature equal to 180 K, we get  $\mu = 8.651$ , and, hence,  $\kappa_{11l} = 0.59$  W/(m·K),  $\kappa_{22l} = 0.925$  W/(m·K),  $\kappa_{33l} = 1.485$  W/(m·K). These values correlate as 1:1.568:2.517. At the same time, the estimate of lattice thermal conductivity anisotropy by formula (13) yields the ratio 1:12.118:5.823, which, as we shall see later, is obviously exaggerated in comparison with the true one.

From the experimental data on thermal conductivity anisotropy of hole-type cadmium antimonide presented in [8] it follows that in given material this anisotropy is fundamentally different from electric conductivity anisotropy. Namely, for electric conductivity components the ratio  $\sigma_{22} < \sigma_{11} < \sigma_{33}$  is valid, and for thermal conductivity components – the ratio  $\kappa_{11} < \kappa_{22} \approx \kappa_{33}$ . If scattering of free charge carriers is assumed to be isotropic, then, with regard to the Wiedemann-Franz relation, such anisotropy is attributable to essential contribution of lattice thermal conductivity. If, however, scattering of free charge carriers is anisotropic, it can also contribute to increase or reduction of thermal conductivity anisotropy. Moreover, it can testify to the anisotropy of umklapp coefficient in *CdSb*.

We will estimate thermal conductivity anisotropy of *CdSb* with regard to the above facts. For this purpose we will make a model assumption that two of the three components umklapp coefficient tensor coincide. Under this assumption the following variants are possible: 1) on the assumption that  $\mu_{11} = \mu_{22} \neq \mu_{33}$ , taking into account caloric (scalar) Debye temperature we obtain that  $\mu_{11} = \mu_{22} = 6.907$ ,  $\mu_{33} = 11.533$ ,  $\kappa_{11} = 0.722$  W/(m·K),  $\kappa_{22} = \kappa_{33} = 1.139$  W/(m·K), and then the ratio  $\kappa_{22}/\kappa_{11} = 1.578$ ; 2) on the assumption that  $\mu_{11} = \mu_{33} \neq \mu_{22}$ , taking into account caloric (scalar) Debye temperature, we obtain that  $\mu_{11} = \mu_{33} = 10.423$ ,  $\mu_{22} = 6.235$ ,  $\kappa_{11} = 0.498$  W/(m·K),  $\kappa_{22} = \kappa_{33} = 1.251$  W/(m·K), and then the ratio  $\kappa_{22}/\kappa_{11} = 2.512$ ; 3) on the assumption that  $\mu_{11} = \mu_{22} \neq \mu_{33}$ , taking into account anisotropic X-ray characteristic Debye temperature, we obtain  $\mu_{11} = \mu_{22} = 5.895$ ,  $\mu_{33} = 9.662$ ,  $\kappa_{11} = 0.837$  W/(m·K),  $\kappa_{22} = \kappa_{33} = 1.082$  W/(m·K), and then the ratio  $\kappa_{22}/\kappa_{11} = 1.293$ ; 4) on the assumption that  $\mu_{11} = \mu_{33} \neq \mu_{22}$ , taking into account anisotropic X-ray characteristic Debye temperature, we obtain  $\mu_{11} = \mu_{33} = 8.627$ ,  $\mu_{22} = 5.246$ ,  $\kappa_{11} = 0.596$  W/(m·K),  $\kappa_{22} = \kappa_{33} = 1.202$  W/(m·K), and then the ratio  $\kappa_{22}/\kappa_{11} = 2.017$ . Note that the estimate of thermal conductivity anisotropy by the variant “1”, i.e. 1.578, is closest to the experimentally observed, as long as according to the evidence from [2] the above relation is 1.68, and, thus, the error is 6.2 % from the larger value. However, according to the evidence from [2], the averaged over directions thermal conductivity value at 300 K is 1.6 W/(m·K), and the value from handbook [6] – 1 W/(m·K). Both values can be simultaneously true only in the case when the higher of them characterizes full thermal conductivity of *CdSb* single crystal, and the lower – its lattice component. Therefore, it can be concluded that lattice thermal conductivity anisotropy of cadmium antimonide is close to component anisotropy due to free charge carriers.

## Conclusions

1. Lattice thermal conductivity anisotropy of cadmium and zinc antimonides is due to anisotropy of sound velocity, the Gruneisen tensor and phonon umklapp parameter.
2. The use of anisotropic X-ray characteristic Debye temperature instead of its isotropic caloric value reduces the expected estimate of lattice thermal conductivity anisotropy.
3. Estimate of lattice thermal conductivity anisotropy of cadmium and zinc antimonides without regard to sound velocity anisotropy and the frequency dependence of phonon relaxation time in said materials results in drastic overrating of this anisotropy value as compared to the experimental data.

The author considers it his pleasant duty to express his gratitude to the chief researcher L.N. Vikhor for the useful and constructive discussion of the results of the work.

## References

1. M.I. Fedorov, L.V. Prokofyeva, Yu.I. Ravich, P.P. Konstantinov, D.A.Pshenai-Severin, and A.A.Shabaldin, Thermoelectric Figure of Merit of *ZnSb* Intermetallide, *Semiconductors* **48**(4), 448 – 453 (2014).
2. A.A. Ascheulov, I.S. Romanyuk, *Anisotropic Optical Thermoelements Based on Cadmium Antimonide and Their Application* (Kyiv: Zoloti Litavry Publ., 2012), 228p.
3. P.G. Klemens, Lattice Thermal Conductivity, In: *Solid State Physics. Advances in Research and Applications*, Vol.7, pp. 1 – 98 (New York: Academic Press. Inc. Publishers, 1958), 526 p.
4. P.V. Gorskiy, V.P. Mikhalchenko, Reduction of Thermoelectric Material Lattice Thermal Conductivity Using Shape-Forming Element Optimization, *J. Thermoelectricity* **1**, 18 – 25 (2013).
5. L.I. Anatyshuk, V.P. Mikhalchenko, On the Correlation between Thermal Elasticity Anisotropy and Some Thermoelectric Properties of *ZnSb* Single Crystals, *J. Thermoelectricity* **3**, 33 – 41 (2002).
6. G.B. Boki, I.P. Voronina, and G.G. Dvoriankina, *Crystal-Chemical, Physics-Chemical and Physical Properties of Semiconductor Substances* (Moscow: Standards Publ.House, 1973), 208 p.
7. V.P. Mikhalchenko, X-Ray Diffractometric and Acoustic Studies of Some Anharmonic Effects in Crystals, *Doctoral Thesis in Physical and Mathematical Sciences* (Chernivtsi, 1976), 314 p.
8. V.B. Lazarev, V.Ya. Shevchenko, Ya.Kh. Grinberg, and V.V. Sobolev, *Semiconductor Compounds  $A^{II}B^V$*  (Moscow: Nauka, 1978), 256 p.

Submitted 12.10.2016



*Montasser S. Tahat*

**Montasser S. Tahat**

Al-Balqa' Applied University, Al-Huson University College, Mechanical Engineering Department, PO Box 50, Al-Huson 21510, Irbid, Jordan

**MECHANICAL AND THERMO-ELECTRIC  
PROPERTIES OF *Cu/SiC/Gr* MULTI-LAYER HYBRID  
METAL MATRIX COMPOSITE**

---

*Combined effect of both graphite and SiC content into Cu matrix has been studied during fabrication of Cu-graphite-SiC multilayer and single-layer composites by powder metallurgy. Mechanical properties of the composites are enhanced by simultaneous addition of equal weight fraction of SiC and Gr particulates of 3 %, 6 %, 9 %, and 12 % reinforcement into pure Cu, whereas electrical conductivity deteriorates. Multi-layer composites enhanced the wear resistance and improved the friction performance. The CTE could be decreased effectively through well bonding between reinforcement phase and metal matrix. Electrical conductivity decreases with increase in both graphite and SiC content. This single and multilayer hybrid metal composites will have promising future in electrical contacts, thermal and electronic packaging, friction and brakes materials applications.*

**Key words:** *Cu-Gr/SiC*, HMMCs, multi-layer composites.

## **Introduction**

Since the discovery of thermoelectric materials, great efforts have been put into the improvement of their efficiency and the development of devices for real life applications. This progress has been accelerated in the last few decades by the increasing demand for renewable energy sources. The discovery and design of compounds with intrinsically low thermal conductivity, especially compounds with a special bonding nature and stable crystal structure, is a new direction to broaden the scope of potential thermoelectric (TE) materials [1].

Copper is used extensively in thermoelectric instrument making as a material for connection of thermoelements. Therefore, research on the properties of *Cu* based materials, in particular, copper nanocomposites, is vital for thermoelectricity.

Copper is a widely used industrial and functional metal for various thermal and electronic applications, i.e. electronic packaging, electrical contacts and resistance welding electrodes. The scope of the devices could be significantly expanded from temperature sensors to mass produced, flexible thermoelectric generators [2]. This is because of good thermal and electrical conductivity, high plasticity and excellent resistance to corrosion and oxidation. Nevertheless, low mechanical strength and undesirable wear resistance limit its applications [3 – 7].

Suitable thermal and mechanical properties can be achieved by blending appropriate metallic and ceramic phases to form a composite. The incorporation of *SiC* hard reinforcing particles into the *CuMCs* improving their mechanical and tribological behavior, *Cu/SiC* metal matrix composites, because of their excellent electrical and thermal conductivity, enhanced hardness values, wear and frictional properties, has been the subject of extensive research [8 – 10].

Characteristics of *CuMCs* reinforced with soft reinforcement particles of *Gr*, being a solid lubricant and possessing good conductivity and anti-seizure properties are covered in [11 – 12].

Use of single reinforcement in copper may sometimes lead to the deterioration in the values of its physical properties. To overcome this, the concept of use of two different types of reinforcement is being tried out in copper matrix. To offset these effects, graphite being a solid lubricant and possessing good conductivity can be dispersed in copper along with *SiC* [13 – 15].

However, insufficient information is available about the processing and characterization of these novel laminated hybrid copper composites. The present study has been carried out to investigate combined effect of graphite and *SiC* into *Cu* matrix during fabrication of *Cu*-graphite-*SiC* multilayer hybrid metal matrix composite by layer compaction and pressure sintering at varying equal weight fraction of *SiC* and *Gr* particulates of 3 %, 6 %, 9 %, and 12 % reinforcement. This experimental analysis and test results on the thermo-physical properties of multilayer and single layer composites *Cu/SiC/Gr*-HMMCs will provide essential guidelines to the manufacturers.

## **Experimental procedure**

### **Materials and preparation of composites**

For the preparation of the composites, the raw material powders used were commercially pure powders of copper, tin, *SiC*, barium sulphate, graphite and zinc stearate. Silicon carbide particles of 45 μm average size and graphite particles of 90 μm average size were used in this study.

In order to manufacture *Cu*-graphite-*SiC* composite, powders were blended in a shaker mixer for 30 min to ensure the uniform distribution and homogeneous mixing of copper, graphite and *SiC* powders. The powder mixtures were cold compacted by uniaxial die pressing by applying pressure of 500 MPa for 15 min and then sintered in a tubular furnace at 750 °C for 90 minutes in argon atmosphere, while keeping the same compaction and sintering parameter. For now, we have produced composites *D* and samples test №2.

This samples were subject to the manufacturer’s recommended cure cycle. The purpose of addition of tin is to facilitate the liquid phase sintering for better densification. At this stage, we have processed multilayer hybrid composites (*A*, *B* and *C*) for samples test №1: The specimens have the same structure, i.e., *Cu* matrix, physical dimensions, and differ only in *SiC/Gr* reinforcement and laminate lay up as per table.

*Table*

*The content of reinforcing and matrix materials*

Composite	Layers	Silicon Carbide ( <i>SiC</i> ), %	Graphite ( <i>Gr</i> ), %	Matrix
<i>A</i>	3	9	9	1 % <i>Sn</i> , 10 % <i>BaSO4</i> and 83 % <i>Cu</i>
<i>B</i>	3	6	6	1 % <i>Sn</i> , 10 % <i>BaSO4</i> and 77 % <i>Cu</i>
<i>C</i>	3	3	3	1 % <i>Sn</i> , 10 % <i>BaSO4</i> and 81 % <i>Cu</i>
<i>D</i>	1	9	9	1 % <i>Sn</i> , 10 % <i>BaSO4</i> and 81 % <i>Cu</i>

## **Testing Procedures**

### **Samples Test №1: Single to multi-layered *Cu*-HMMCs**

Composites were cast in required diameter and length. The silicon carbide particles exhibit the form of solid crystal, whereas the graphite particles appear to be flakes.

The different samples were precision weighed on electronic balance to an accuracy of 0.1 mg. In general, the experimental data obtained from the three specimens cut from the same composite were taken as the average value.

The wear and friction behavior of the composites was studied using a computer controlled pad-on-disk laboratory scale inertial brake dynamometer in air at ambient temperature (25 – 30 °C).

The compression tests were carried out in a universal testing machine at a strain rate of 0.001 m/s. The size of the specimen for compression and thermal expansion was 5 × 5 × 20 mm. The coefficient of thermal expansion of specimens was tested from 20 °C to 200 °C, with the heating rate of 5 °C/min, using Linesis 75 Platinum Horizontal Dilatometer.

### **Samples test №2: Single Layer, 10 % BaSO<sub>4</sub> and 78 % – 87 % Cu, varying SiC/Gr contents of 3 %, 6 %, 9 %, and 12 %:**

The density measurements were carried out to determine the porosity levels of the samples. The density of the samples was measured according to ISO 2738 standard. The measured density was compared to the value obtained using rule-of-mixtures so as to determine the volume fraction of porosity.

Four probe electrical resistivity measuring instrument was used to measure the electrical resistance of the sample, in which two probes were connected with the ammeter and another two with the voltmeter.

## **Results and Discussion**

### **Density and Porosity**

Fig. 1 shows the variation of relative density for single-layer Cu-graphite-SiC hybrid composites containing 3 %, 6 %, 9 %, and 12 % SiC and 3 %, 6 %, 9 %, and 12 % graphite. The percentage porosity present in the composites rises with the increase of the reinforcement content, as shown later in Fig. 4. Graphite is a solid lubricant material and facilitates movement and rearrangement of matrix and reinforcement particles resulting in higher densification. It is also observed that the value of relative density increases with increase in SiC content. The density of composite depends on the volume fraction of soft and hard phase. At low fraction of SiC, hard particle is well dispersed and soft graphite and Cu particles can deform to fill the gaps and the density value of around 85 % is achieved depending on graphite content. The volume fraction of porosity, and its size and distribution in a cast metal matrix composite play an important role in controlling the material mechanical properties. It is necessary that porosity levels be kept to a minimum.

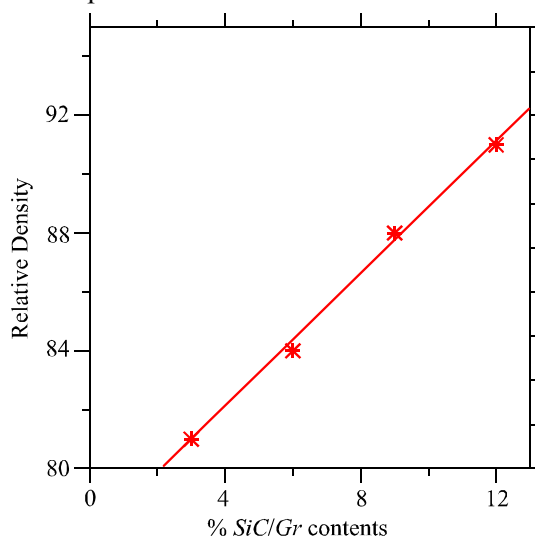


Fig. 1. The density variations with increasing SiC/Gr contents.



### Wear Resistance

As shown in Fig. 2, with the increase in the SiC/Gr contents and layers, the wear rate of Cu/SiC/Gr HMMCs reduces. It was found that the amount of graphite released on the wear surface forms a tribofilm on the contact surfaces. This reduces the wear rate. The presence of graphite tribolayer (or mechanically mixed layer) also increases the seizure resistance and enables to run under boundary lubrication without galling. Increasing protrusion of SiC particles results in formation of a more stable lubricating film on the tribosurface of hybrid composites.

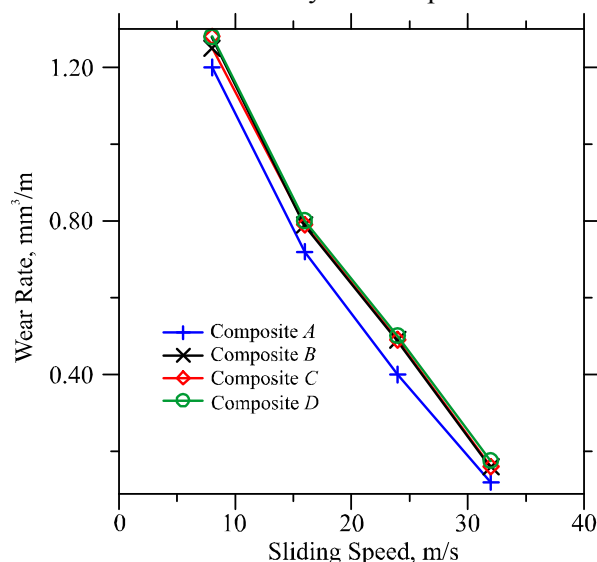


Fig. 2. The effect of SiC/Gr addition on the matrix wear rate of the investigated composites.

### Braking Performance

As shown in Fig. 3, the amount of graphite released on the wear surface forms a tribofilm on the contact surfaces. This reduces the overall friction coefficient. Also, composites D show a very high friction coefficient of 0.565 at 4 m/s. This high friction does not translate into improving braking performance or wear resistance. The development of an oxide scale, greater participation of graphite in the sliding, weakening adhesive and abrasive frictional contacts diminish the frictional forces at the interface with growing sliding speeds.

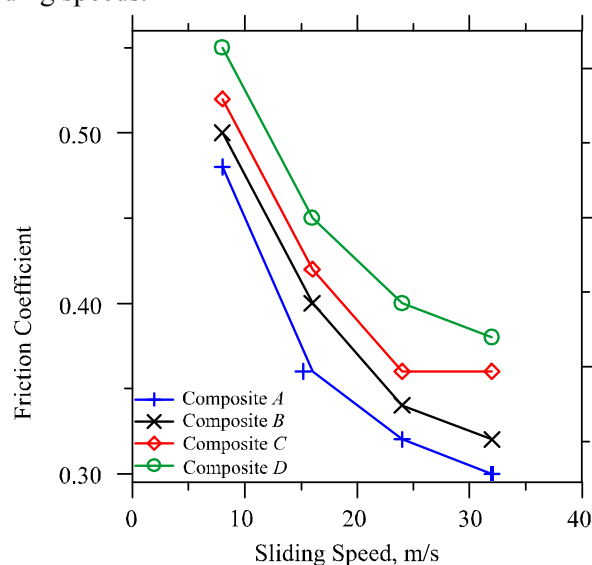


Fig. 3. Effect of sliding speed on mean friction coefficient of the composites.

### Thermal Expansion and Porosity

It is evident from Fig. 4 that coefficient of thermal expansion (CTE) of a laminated composite is lower than that of a single-layer one. As SiC/Gr volume fraction increases, the CTE tends to decrease linearly with increase of porosity. The packaging materials in microelectronics should have high thermal conductivity to dissipate the heat, and low CTE to decrease the thermal expansion mismatch among the devices. It is evident from the plot in Fig. 4 that the CTE of Cu-SiC-Gr hybrid composites decreases with increase in % reinforcement. Introducing a high amount of graphite to the Al-Si matrix alloy was found to be beneficial for the dimensional stability. Results revealed that graphite particles absorb the thermal expansion because of their layered structure.

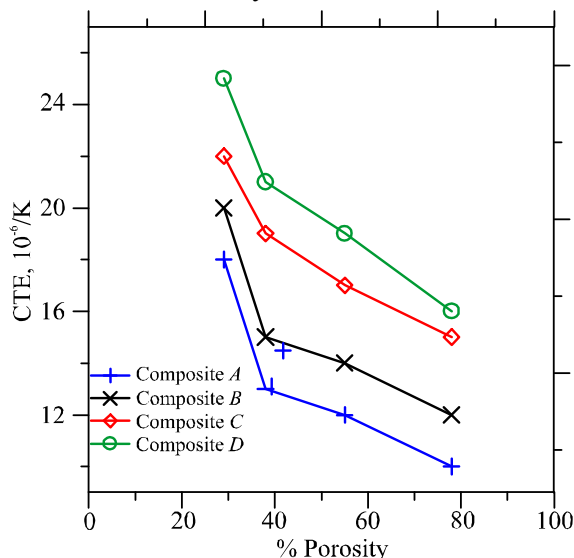


Fig. 4. Variations in CTE for different particulate composites (temperature: 100 °C).

### Compressive Strength

Fig. 5 shows the compressive stress–strain curve for Cu-graphite-SiC composites. It is observed that compressive strength of a laminated composite is greater than that of a single layer one. This is due to higher density and hardness of the composites. It has been observed that the bending strength of three-layer Cu based composites is much greater than that of a single layer, due to residual compressive stresses in the outer layer.

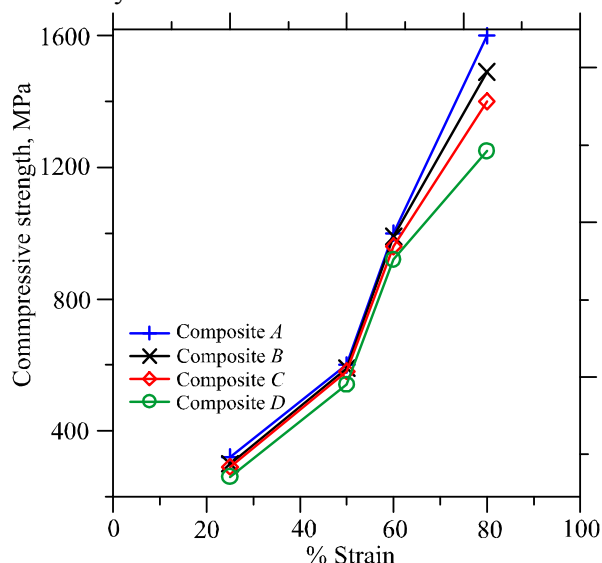


Fig. 5. Effect of reinforcements volume fraction on compressive strength.

## Electrical Conductivity

From Fig. 6 it can be observed that the electrical conductivity of layered Cu hybrid composites containing 3 %, 6 %, 9 %, and 12 % SiC and 3 %, 6 %, 9 % and 12 % graphite tends to decrease linearly with increase of SiC/Gr. The ceramic based SiC forms a barrier to motion of copper electrons, providing electrical conductivity. SiC particles added into pure copper redouble the electrical resistivity via distorting the structure, and so the electrical conductivity of composites decreases with increasing the volume ratio of SiC [13].

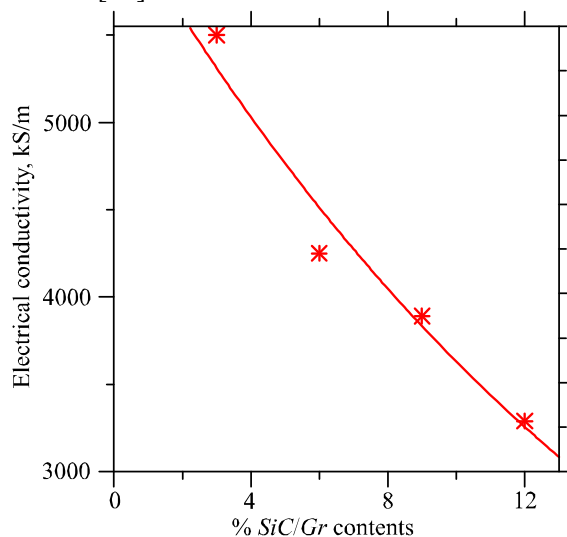


Fig. 6. Effect of reinforcements volume fraction on electrical conductivity.

Cu based metal matrix composite with very low SiC/Gr (0 – 4 %) is highly recommended to be used in many electrical contacts, thermal and electronic packaging applications, as it possesses high electrical conductivity.

## Conclusions

The following points were concluded from the conducted tests of the composites:

1. Cu hybrid composites have been successfully fabricated by layer compaction and pressure sintering with varying dispersion of SiC and Gr particles. We have studied thermophysical properties of Cu/SiC/Gr hybrid composites in three-layer and single-layer configurations containing 3 %, 6 %, 9 % and 12 % SiC and 3 %, 6 %, 9 % and 12 % graphite.
2. The processing employed in this paper would enable realization of electrical contacts, friction materials, brakes and electronic packages made of Cu-Gr/SiC HMMCs.

## References

1. Baoli Du, Ruizhi Zhang, Kan Chen, Amit Mahajan, and Mike J. Reece, The Impact of Lone-Pair Electrons on the Lattice Thermal Conductivity of the Thermoelectric Compound  $CuSbS_2$ , *J. Mater. Chem. A* **5**(7), 3249 – 3259 (2017).
2. Virgil Andrei, Kevin Bethke, and Klaus Rademann, Adjusting the Thermoelectric Properties of Copper(I) Oxide-Graphite-Polymer Pastes and the Applications of Such Flexible Composites, *Phys. Chem. Chem. Phys.* **18**, 10700 – 10707 (2016).
3. M. Lekka, D. Koumoulis, N. Kouloumbi, and P.L. Bonora, Mechanical and Anticorrosive Properties of Copper Matrix Micro- and Nano-Composite Coatings, *Electrochim Acta* **54**, 2540 –

- 2546 (2009).
4. Y. Zhan, G. Zhang, The Effect of Interfacial Modifying on the Mechanical and Wear Properties of *SiCp/Cu* Composites, *Mater Lett* 57, 4583 – 4591 (2003).
  5. K.M. Shu, G.C. Tu, The Microstructure and the Thermal Expansion Characteristics of *Cu/SiCp* Composites, *Mater Sci Eng A* 349, 236 – 247 (2003).
  6. J. Zhu, L. Liu, H. Zhao, B. Shen, and W. Hu, Microstructure and Performance of Electroformed *Cu/nano-SiC* Composite, *Mater Des* 28, 1958 – 1962 (2007).
  7. Th. Schubert, B. Trindade, T. Weibgarber, and B. Kieback, Interfacial Design of *Cu*-based Composites Prepared by Powder Metallurgy for Heat Sink Applications, *Mater.Sci.Eng.A* 475, 39 – 44 (2008).
  8. Mohsen Barmouz, Mohammad Kazem Besharati Givi, and Javad Seyfi, On the Role of Processing Parameters in Producing *Cu/SiC* Metal Matrix Composites via Friction Stir Processing: Investigating Microstructure, Microhardness, Wear and Tensile Behavior, *Materials Characterization* 62, 108 – 117 (2011).
  9. K.M. Shu, G.C. Tu, Fabrication and Characterization of *Cu-SiCp* Composites for Electrical Discharge Machining Applications, *Mater Manuf Processes* 16(4), 483 – 502 (2001).
  10. S.G. Sapate, A. Uttarwar, R.C. Rathod, and R.K. Paretkar, Analyzing Dry Sliding Wear Behaviour of Copper Matrix Composites Reinforced with Pre-Coated *SiCp* Particles, *Mater Des* 30, 376 – 386 (2009).
  11. Y. Zhan, G. Zhang, The Role of Graphite Particles in the High-Temperature Wear of Copper Hybrid Composites against Steel, *Mater.Des.* 27, 79 – 84 (2006).
  12. Y. Qin, Y. Wu, D. Wang, P. Li, X. Huang, and Y. Zheng, Influence of *SiC* Particle Size on the Wear Properties of *SiC/Cu* Composites, *Adv.Mater.Res.* 311 – 313, 635 – 639 (2011).
  13. T. Ram Prabhu, V.K. Varma, and Srikanth Vedantam, Tribological and Mechanical Behavior of Multilayer *Cu/SiC/Gr* Hybrid Composites for Brake Friction Material Applications, *Wear* 317, 201 – 212 (2014).
  14. C.S. Ramesh, R.N. Ahmed, M.A. Mujeebub, and M.Z. Abdullah, Development and Performance Analysis of Novel Cast Copper-*SiC-Gr* Hybrid Composites, *Mater. Des.* 30, 1957 – 1965 (2009).
  15. A. Meher & D. Chaira, Effect of Graphite and *SiC* Addition into *Cu* and *SiC* Particle Size Effect on Fabrication of *Cu-Graphite-SiC* MMC by Powder Metallurgy, Published online by Trans Indian Inst Met (2017).

Submitted 21.10.2016



*V.P. Shafraniuk*

## **V.P. Shafraniuk**

Higher Educational Establishment of Ukraine  
Bukovinian State Medical University, 2 Teatralna Square,  
Chernivtsi, 58000, Ukraine

### **RESEARCH ON MECHANICAL STRESS RELAXATION IN REAL CRYSTALS BY X-RAY DIFFRACTION MOIRE METHOD**

---

*The paper presents the results of research on the strain fields arising in the vicinity of local damages in silicon and germanium single crystals using X-ray diffraction moire method. It is established that relaxation of strain fields around mechanical damages (indenter marks and scratches, laser induced damages) takes place even at room temperature, as well as at annealing temperatures from 473 K to 1073 K. Low-temperature relaxation results from atomic displacement due to weakening of chemical bonds, whereas high-temperature relaxation results from dislocation motion in  $\{111\}$  planes and  $\langle 110 \rangle$  directions.*

**Key words:** scratches, indenter marks, X-ray interferometer, moire fringes, thermoelement, thermal cooler.

#### **Introduction**

A relevant problem in thermoelectricity is creation of high-quality and reliable metal-thermoelectric material ohmic contacts. The quality and reliability of such contacts is influenced by structural perfection of near-surface layers of thermoelectric materials. In most cases, a metal layer-thermoelectric material structure comprises areas of local mechanical stresses that are related to interface boundaries and local damages of material surface [1]. Thermal treatment stipulated by technology of creating contacts to high-temperature thermoelectric materials based on germanium-silicon solid solutions leads to relaxation of local mechanical stresses and formation of dislocation clusters [2]. Physical regularities of the process of relaxation of mechanical stresses in planar contact structures allow solving the problem of preservation of structural perfection of thermoelectric materials, which is a prerequisite for creation of high-quality and reliable contacts in thermoelectric materials. With modern microminiaturization of semiconductor devices and thermoelectric modules it is necessary to know the distance at which working components should be arranged from the scribed stripes, as long as strain fields affect the electric parameters of these devices. The data on the dynamic properties of dislocations in semiconductors were mainly obtained from measuring the velocity of dislocations [2] under the effect of time-constant stress, whereas formation of defects in real semiconductor structures occurs in variable stress field. In [2], by X-ray topography methods it was established that during scribing strain fields have a length of  $\sim 100 - 150 \mu\text{m}$ .

Thus, the research on the process of relaxation of local mechanical stresses is of great current interest. X-ray diffraction moire (XRD) method is exceptionally sensitive to slight strains ( $10^{-4} - 10^{-8}$ ) and relative rotations ( $0.1 - 0.001^\circ$ ) of atomic planes and makes it possible to measure with high accuracy the absolute values of wavelength and periods of crystal lattices, to determine refraction factors and dispersion corrections of various substances, to study the heterogeneity of thermoelectric solid solutions *Ge-Si*, *Bi-Te*, biological objects with phase moire topography, to determine the Burgers

vector of single dislocations [3 – 8]. In its universality, XRD method outperforms considerably all known X-ray diffraction methods. Exactly for this reason the present paper employs XRD method to study the relaxation of strain fields in real crystals which occur around local damages (indenter marks, scratches, laser induced damages – craters) in the surface layers of silicon and germanium at different annealing temperatures.

### Research methods

Research was performed on interferometer samples made of perfect silicon and germanium single crystals. Prior to causing local mechanical damages on the output surface of the analyzing crystal, interferometers had been investigated. Some interferometers under study partially comprised structural moire fringes and were moire-free, i.e. perfect. Local mechanical damages in the surface layers on the output surface of silicon, germanium analyzing crystal of (111), (100), (110) orientation were simulated with the aid of microhardness indenter marks, scratches and laser induced damages. Moire patterns were obtained in  $CuK\alpha$ -radiation using a scanner along the diffraction vector. Marks and scratches were applied by a diamond indenter on microhardness tester on the output surface of the interferometer analyzing crystal in different crystallographic directions at different loads. Laser surface damage manifested in the form of a crater, was made by means of neodymium laser on the surface of analyzer (111).

### Research results

During scribing of a scratch two processes should be distinguished: impression and indenter motion along crystal surface. A zone of plastically strained material permeated with microcracks and chips, as well as a zone of elastic stresses related to riveting are created in the vicinity of a scratch. The strained area in the vicinity of microindenter marks and scratches can be found from moire patterns [5].

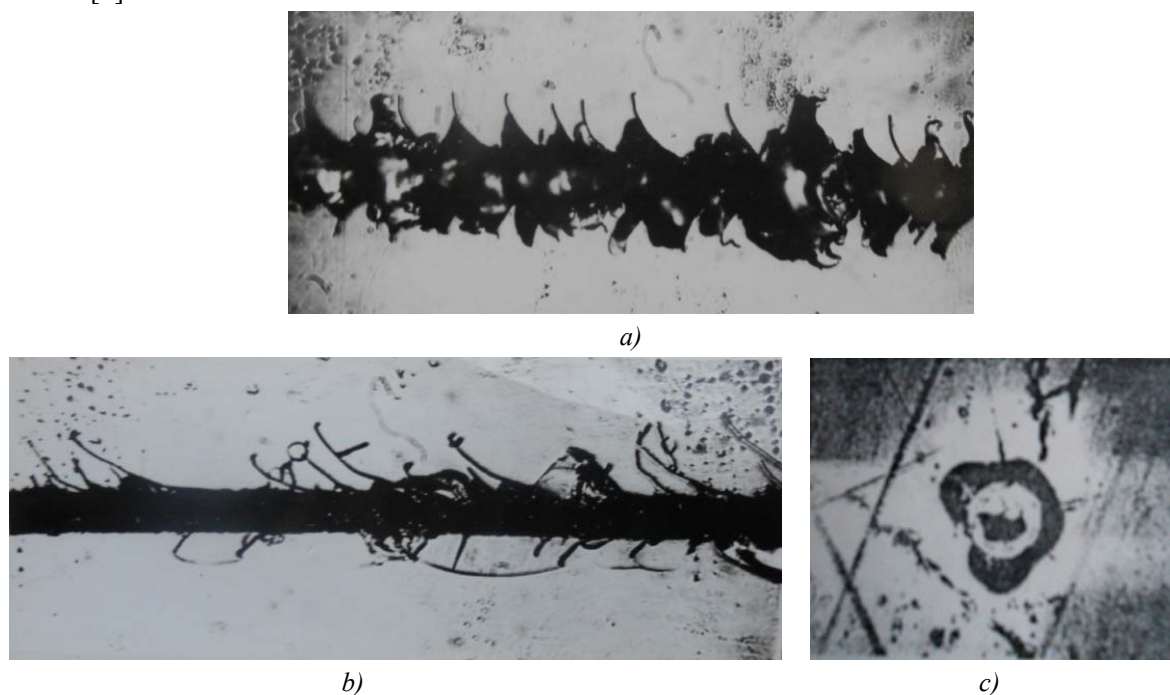


Fig. 1. Appearance of scratches in different crystallographic directions on the surface of analyzer: a) in  $[110]$  direction, b) in  $[11\bar{2}]$  direction, c) image of laser induced damage on (111) surface.

Fig. 2 shows a moire pattern from a scratch and indenter marks at different loads 15, 20, 25 g applied on the output surface of the analyzing crystal of perfect silicon interferometer. The direction of a scratch coincides with the direction of the diffraction vector  $g$  at a load of 25 g and length 2 mm. Moire patterns were obtained with the aid of a scanner in  $CuK\alpha$ -radiation along the diffraction vector. Moire fringe is symmetrical with respect to the centre of a scratch divided by zero moire fringe corresponding to the resulting strain field from the scratch. To the left and right of the zero fringe there are 12 – 14 moire fringes the distance between which with approach to the edges of a scratch is reduced, which allows speaking about strain increase. It is known that a moire fringe is a geometrical place of points of equal displacements along the diffraction vector, since as at the distance equal to moire fringe period the value of displacement is equal to interplanar distance of perfect lattice. An interferogram was also obtained from this scratch at rotation of interferometer by 90 degrees with the use of reflection  $(0\bar{2}2)$ , when the diffraction vector is normal to this scratch. Scratch image on the moire pattern is an intermittent light line restricted on both sides by a dark halo, and a diffraction contrast from a scratch (Fig. 2), when the diffraction vector is parallel to it, is composed of black and white lobes. Moire fringes envelop the scratches.

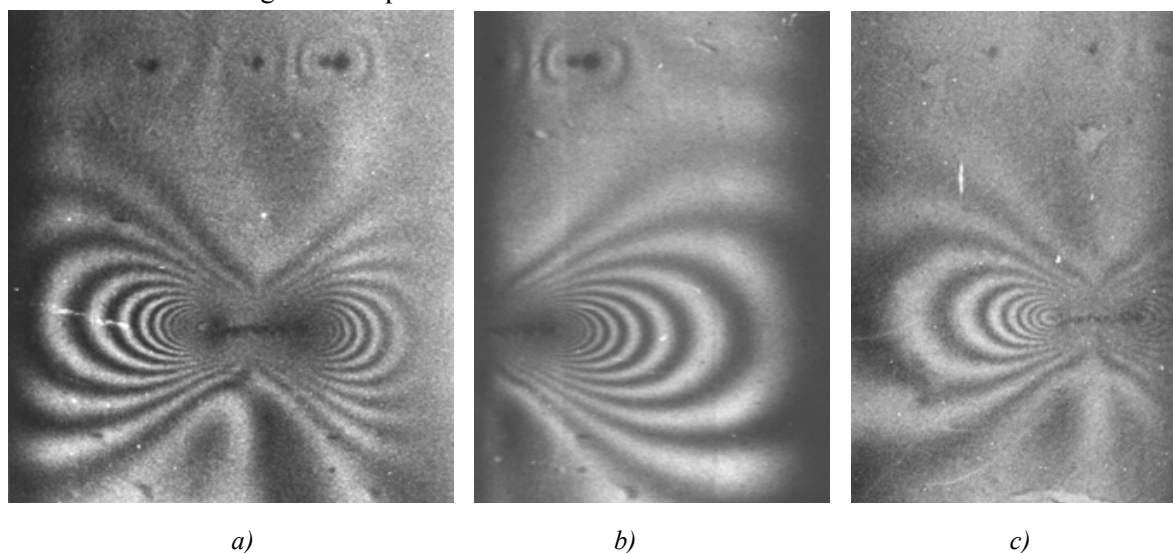


Fig. 2. Moire patterns from the scratch and indenter marks obtained from different areas of interferometer analyzer in  $CuK\alpha$  radiation at room temperature (a, b). b) after annealing at temperature 673 K. Reflection  $(0\bar{2}2)$ ,  $\times 10$ .

On moire patterns (Fig. 2) one can simultaneously observe diffraction images of the scratch and indenter marks, localized next to them and long-range strain fields in the form of moire fringes. From the moire patterns it is seen that elastic strain fields of indenter marks expand to large distances which many times exceed their real dimensions  $d$ . The defined dimensions of contrast areas  $D$  along the diffraction vector allow speaking about their asymmetry. The asymmetry line of diffraction contrast with respect to reflection planes coincides with zero contrast line perpendicular to the diffraction vector. Reducing the load and indenter mark size, we managed to show that the ratio of contrast value to indenter mark size increases and this is most probably due to peculiarities of stress relaxation in the surfaces layers of silicon. Decrease in  $D/d$  with increasing the load and indenter mark size is attributable to the onset of brittleness limit in silicon crystal under the indenter and the relief of residual stresses in the process of occurrence of microcracks.

Fig. 2 shows a moire pattern at interferometer annealing at temperature 673 K in the air. From

the moire patterns (Fig. 2) it is seen that partial stress relaxation takes place in the vicinity of indenter marks and scratches.

On the diffraction moire patterns there are three typical dependences of moire fringe period on strain value:  $\Lambda_d = \frac{d_0 d}{|d - d_0|} = \frac{1}{\Delta g}$  - dilatation moire, rotation moire -  $\Lambda_r = \frac{1}{\Delta g_r} = \frac{d_0}{\theta}$ , mixed moire -  $\frac{1}{\Lambda} = \sqrt{\left(\frac{1}{\Lambda_d}\right)^2 + \left(\frac{1}{\Lambda_r}\right)^2}$ . Measuring the periods between moire fringes and their inclination to reflecting planes by means of relations:

$$d = \Lambda \left[ 1 + \left( \frac{\Lambda}{d_0} \right)^2 + 2 \frac{\Lambda}{d_0} \cos \phi \right]^{\frac{1}{2}}, \quad \theta = \frac{\sin \phi}{\frac{\Lambda}{d_0} + \cos \phi} \quad (1)$$

we calculated relative strains  $\frac{\Delta d}{d_0}$  and rotations of atomic planes  $\theta$  in the analyzing crystal. Relative strains change from  $2 \times 10^{-6}$  to  $5 \times 10^{-7}$ , and rotations of atomic planes – from 0.0025 to 0.05 angular seconds.

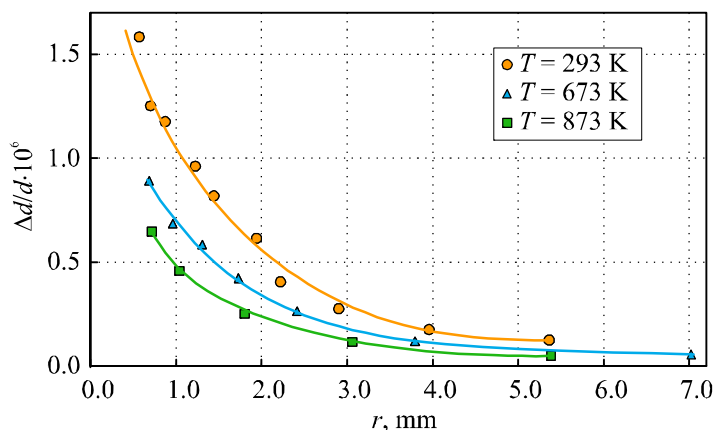


Fig. 3. Curves of relative strain versus the edge of a scratch (Fig. 2).

Fig. 3 represents curves of relative strain versus the distance from the edge of a scratch for different annealing temperatures. Analysis of the investigations shows that stress relaxation processes in silicon crystal at annealing temperatures from 293 K to 873 K are based on different mechanisms: 1) initial stress relaxation as a result of atomic displacement due to weakening of chemical bonds with a rise in temperature; 2) high-temperature relaxation occurs due to dislocation motion in  $\{111\}$  planes and  $\langle 110 \rangle$  directions [5].

The paper also studied the way scratches are depicted in structural dilatation moire which are scribed in different directions to the diffraction vector (Fig. 4). These interferograms (Fig. 4) were obtained from a silicon interferometer, on the output surface of which two scratches 1.5 mm and 2 mm were scribed parallel and normal to the diffraction vector  $g_{220}$ , respectively, under the load of 40 g.

Structural moire fringes are moved apart by the field of elastic strains that appeared in the area of scratches. In the moiré patterns (Fig. 4), the structure of the diffraction contrast of scratches is clearly visible. Interferograms obtained at different times (1, 5, 12 days, Fig. 4), allowed revealing that even at room temperature there is stress relaxation around scratches, which is manifested in contrast change, splitting of moire fringes and change of period between them. It is almost impossible to fix this change by other methods, since a change in strained crystal area near the scratch has passed interplanar distance (1.920752 Å).



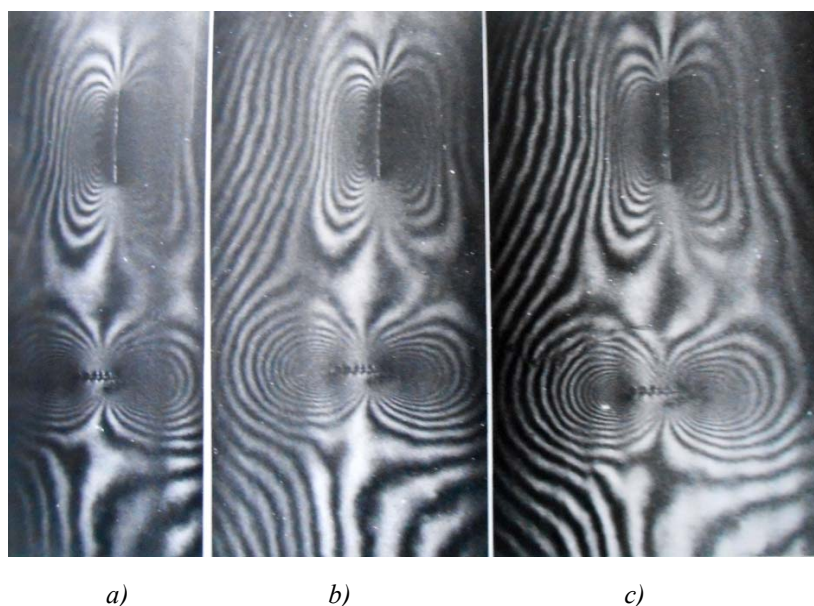


Fig. 4. Moire patterns of scratches on (111) surface of Si analyzer

in  $[110]$  and  $[\bar{1}1\bar{2}]$  directions at a load of 0.4 N: a – 1 day after scratching; b – 5 days; c – 12 days,  $\times 8$ .

The number of additional moire fringes around a scratch depends on the load on the indenter (Fig. 4, 5). Structural moire fringes in the centre of a scratch are divided by zero dark moire fringe relative to which the moire pattern is partially symmetric (Fig. 5).

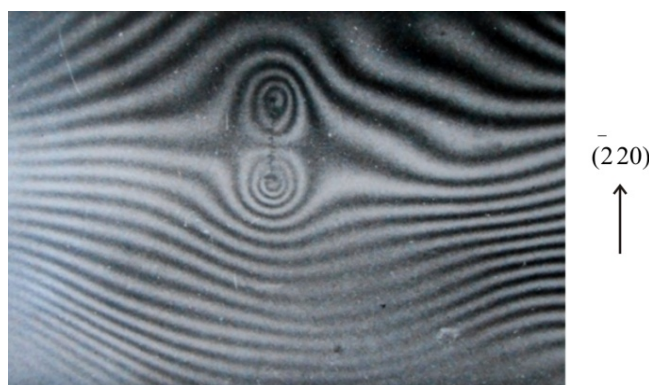


Fig. 5. Image of a scratch in the structural moire applied on the analyzer surface

(111) in  $[\bar{1}10]$  direction at a load of 0.15 N. Reflection  $(\bar{2}20)$ ,  $\times 8$ .

It is noteworthy that on the interferograms one can simultaneously observe a diffraction image of the scratch which is localized close to it and to strain fields which become apparent as moire fringes at large distances. The dimensions of diffraction and moire contrast areas  $L$  tens and hundreds of times exceed the geometrical dimensions of scratches. With increasing scratch width, the ratio  $L/d$  ( $d$  is scratch width) is reduced. This is due to the fact that under the influence of large loads the boundary of brittle fracture occurs, causing the appearance of cracks and partial relaxation of elastic stresses.

This paper also analyzed the way a scratch is depicted depending on its depth in diffraction moire pattern. For this purpose an interferometer was used which comprised a rotation moire according to which the relative rotation of atomic planes corresponded to 0.025 sec. The interferometer analyzer was set at an angle of 30 minutes in drawing plane, as a result of which the indenter was buried in the surface.

Fig. 6 shows moire patterns with two scratches scribed on the analyzer plane (110) in [001] direction. Diffraction vector  $g(\bar{2}20)$  is normal to traces of scratches. The resulting total field of elastic strains from the two scratches is located on one side of them.

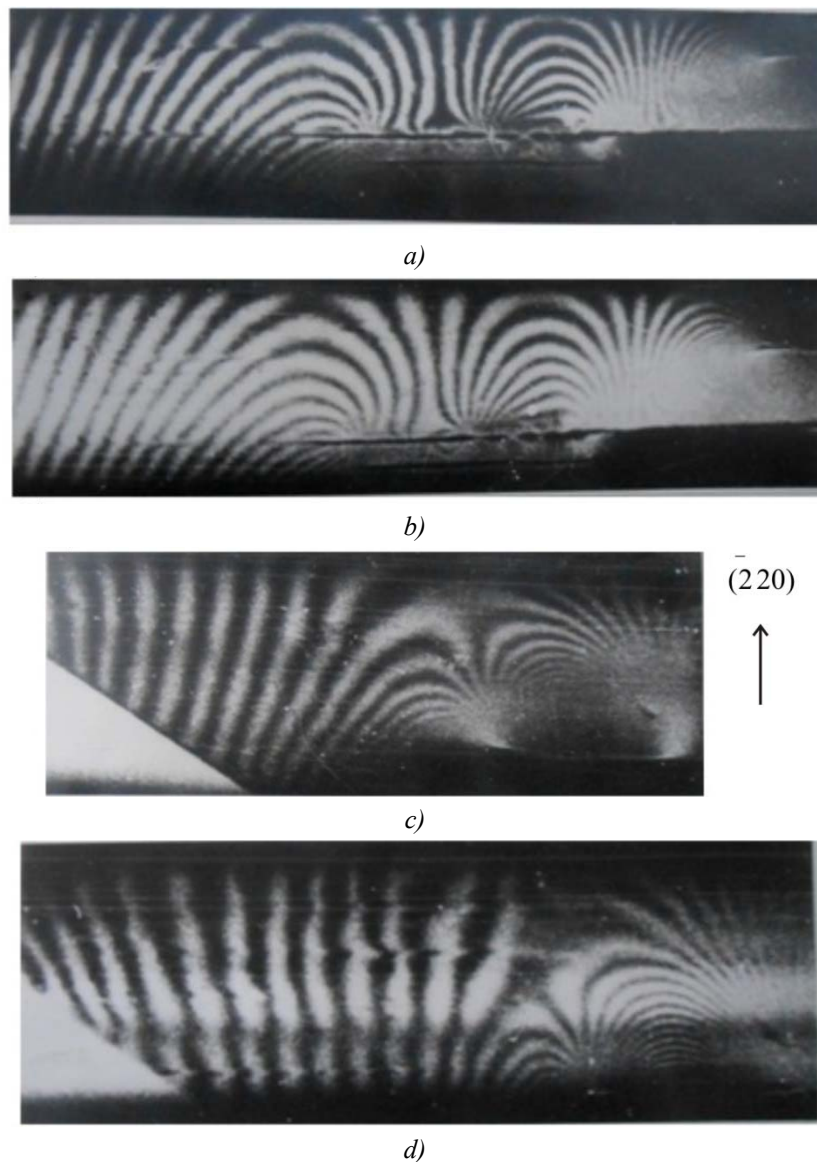


Fig. 6. Interferograms of the system of scratches: a, b – scratches on (110) surface of Si analyzer in [001] direction; c, d – relaxation of stresses after breaking of plate along the scratch line. Reflection  $g(\bar{2}20) \times 10$ .

Seven closest to the scratch moire fringes from the perfect crystal part bend and end near the scratch. Seven further moire fringes begin on the scratch, bend and after some time end on it, which testifies to alternating-sign character of bend of atomic planes. With slight bends of interferometer analyzer, the location of moire fringes is changed, the contrast of moire fringes is changed, but the structure of strain field remains unvaried (Fig. 6b). In this case, strain area found from the moire patterns (Fig. 6), in [110] direction reaches 1 mm. After breaking of analyzer plate along scratch line, the strain area decreased to 0.45 mm, as long as stress relaxation took place as a result of change in the moire patterns (Fig. 6c, d). The strained area of the analyzing crystal was displaced by interplane distance, as long as the contrast of moire fringe changed to the opposite. On the moire pattern (Fig. 6d) in the bifurcated moire fringe one can observe 12 additional fringes, pointing to the presence of dislocations, since each additional fringe corresponds to a dislocation.

From this system of scratches a moire pattern was also taken with the use of reflection (004), when the diffraction vector was parallel to scratch lines (Fig. 7).



Fig. 7. Interferogram of scratches, reflection (004),  $\times 10$ .

The number of additional fringes near the scratch per unit length is large. The upper part of the interferogram shows a dislocation in the form of two additional semi fringes. The number of additional fringes in moire pattern  $N$  is determined by the projection of the Burgers vector to the normal to reflecting planes  $N = (qb)$ , for full dislocations  $N$  is an integer, and dislocation in moire pattern becomes apparent as one or several additional fringes.

Of particular interest is investigation of strain fields arising near the intersection of two scratches. Such scribing method is widely used in the fabrication of microcircuits. It was demonstrated above that strain fields are essentially dependent on the orientation of scratch lines relative to crystallographic directions. For this case scratches were scribed on the output surface (111) of perfect germanium interferometer analyzer at a load of 0.15 N in  $[110]$  and  $[11\bar{2}]$  directions.

As is seen from Fig. 8, the character and value of atomic plane strains depends on the distance to the strain and its orientation relative to diffraction vector. The resulting moire pattern from two scratches which intersect is a system of moire fringes which envelop a scratch parallel to diffraction vector and end on a scratch parallel to it.

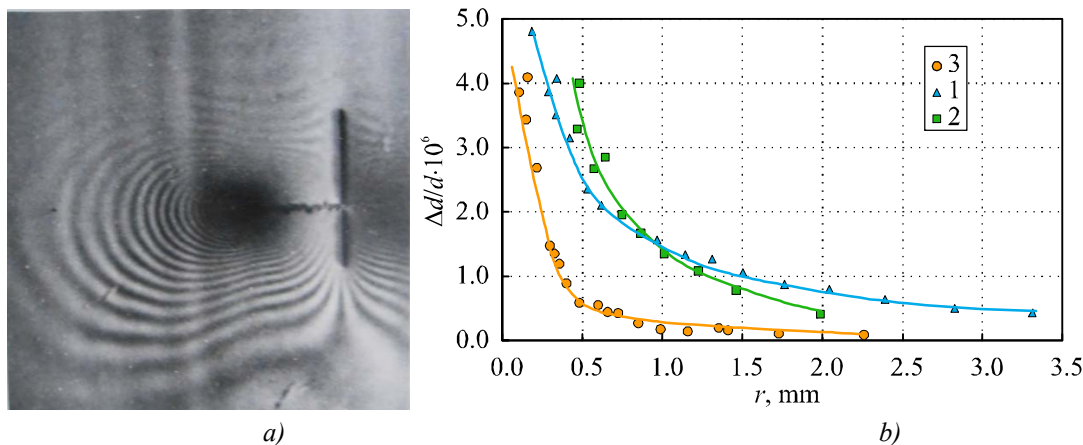


Fig. 8. a – interferogram of intersecting scratches in  $[110]$  and  $[11\bar{2}]$  directions, reflection  $(\bar{2}20)$ ,  $\times 10$ , b – relative strain of atomic planes versus the distance from the edge of scratch in  $[110]$  direction:

$$1 - [110], 2 - [11\bar{2}], 3 - [110] \wedge [11\bar{2}] = 45^\circ.$$

Fig. 8b represents the curves of dependence of relative strains of atomic planes on the distance to the scratch in different directions. The dependence of relative strain of atomic planes on the distance to the scratch corresponds to function  $-1/r$  ( $r$  is the distance from the edge of the strain), which testifies to dislocation structure. The structure of displacement fields is practically unchanged in the presence in the interferometer of dilation, rotation or phase moires.

The paper also examines how a more pattern is formed from the scratches applied at different angles to the diffraction vector (Fig. 9) in structural moire. The resulting strain field becomes apparent in additional moire fringes which begin on one scratch and end on the other, the number of such additional fringes is almost 14.



Fig. 9. Image of scratches applied at an angle to diffraction vector  $g_{220}^-$  :  
a) at room temperature; b) after annealing at 1023 K,  $\times 10$ .

Annealing of interferometer at 1023 K leads to relaxation of stresses in the area of scratches, owing to which the number of moire fringes reduced to three, and relative strains of atomic planes reduced by an order of magnitude. High-temperature relaxation of stresses around scratches occurs due to motion of dislocations in  $\{111\}$  planes and  $\langle 110 \rangle$  directions.

Note that the paper considered the impact of temperature gradient created in the interferometer on the formation and appearance of moire patterns when it is higher and lower than zero. In the former case the interferometer was heated to 310 K by means of thermoelement, in the latter – it was cooled by means of thermal cooler to 263 K. High-quality and contrast moire patterns could not be obtained from different scratches, as long as interacting waves in the interferometer analyzer are not completely coherent, owing to which there is a relationship between the amplitudes of the waves and their phases in the first two interferometer components ( $S$  and  $M$ ).

An important aspect of the investigation is to determine strain fields which arise at interaction of focused laser beam with the surface of silicon single crystals, as long as laser beam scribing is widely used in semiconductor industry when breaking plates into elements [1]. When silicon surface is exposed to a laser beam, craters are formed only when radiation intensity exceeds critical value and in separate cases they have the shape of a hexagon (Fig. 1c) in  $(111)$  plane.

Fig. 10 represents interferograms from laser induce damage which are symmetrical relative to direction  $[11\bar{2}]$ . From the moire patterns it is seen that elastic strain fields expand to long distances which are in large excess over the geometrical dimensions of damages and the diffraction contrast. Imposing temperature gradient  $dT/dy = 2$  K/cm on the interferometer analyzer by means of thermoelement along the atomic planes  $(\bar{1}10)$  [7], it was shown that stress relaxation occurs even at room temperature (Fig. 10b). This low temperature gradient in the interferometer analyzer leads to

relaxation of stresses, as testified by the increased contrast of moire fringes (Fig. 10b) and high stability of thermal cooler (thermoelement), as long as the exposure of moire patterns lasted almost 6 hours. Using relation (1), the relative strains  $\frac{\Delta d}{d_0}$  and rotations of atomic planes  $\theta$  in the analyzing

crystal in the vicinity of laser induced damage were calculated. At annealing of interferometer at different temperatures we managed to find out the processes of relaxation of stresses in the area of laser damage. At annealing temperature 1273 K there is considerable reduction of crystal strain which is clearly visible from the interferogram (Fig. 10c). Calculations showed that relative strains decrease by about 16 times, and the structure of strain field remains unchanged. Control and investigation of structural perfection and distribution of strain fields in the vicinity of local damages allows one to control the energy of laser radiation and correct its technological modes.

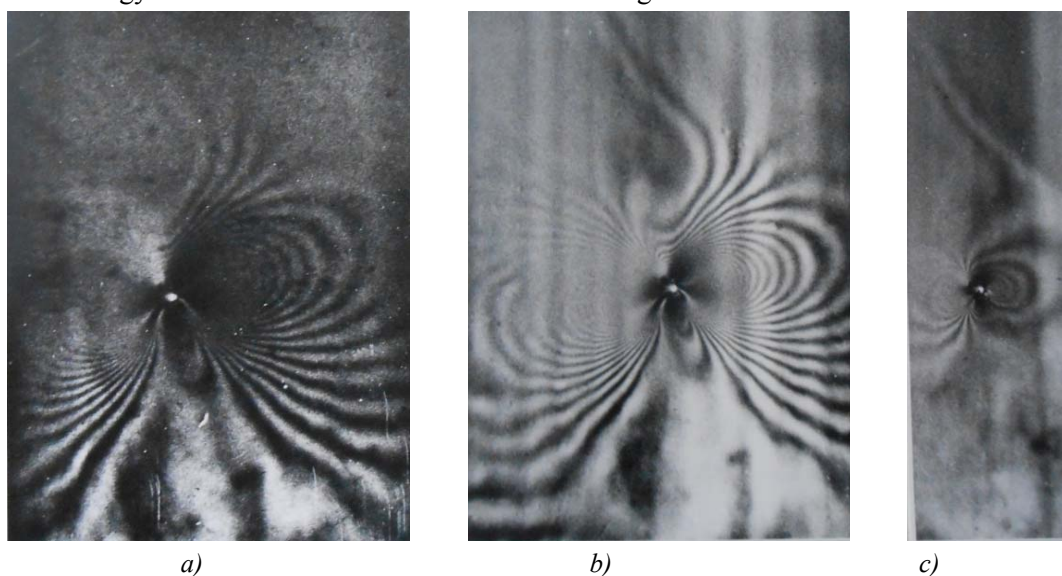


Fig. 10. Moire pattern of laser induced damage in CuK $\alpha$ -radiation with the use of reflection ( $\bar{2}20$ ):  
a – after laser induced damage; b – after applied temperature gradient; c – after annealing,  $\times 10$ .

X-ray diffraction (XRD) moire method allows one to determine with high accuracy the long-range displacement and strain fields of crystal atomic planes at considerable distances from the system of scratches and laser damages, thereby reproducing the real function of local misorientations of the strained crystal region which can be used for theoretical calculation with the use of the Takagi equations of moire patterns [8].

## Conclusions

A new method was proposed to determine strain field distribution in the vicinity of local damages in silicon and germanium single crystals with the use of X-ray diffraction moire. It was found out that relaxation of strain fields around mechanical damages (indenter marks, scratches and laser craters) occurs even at room temperatures, as well as at annealing temperatures from 473 K to 1273 K. Low-temperature relaxation results from atomic displacement due to weakening of chemical bonds, and high-temperature relaxation results from dislocation motion in  $\{111\}$  planes and  $\langle 110 \rangle$  directions. Knowing strained area from the scribed stripes, one can correctly design integral circuits, arranging their components not closer than 150  $\mu\text{m}$  from the edge of the scratch.

**References**

1. O.A. Kontsevoy, Yu.M. Litvinov, and E.A. Fattakhov, *Plasticity and Strength of Semiconductor Materials and Structures* (Moscow: Radio i Sviaz, 1982), 240.
2. S.S. Gorelik, Yu.M. Litvinov, and A.V. Prikhodko, Relaxation of Local Mechanical Strains in Silicon Near-Surface Layers, *J. Surface Investigation* 5, 80 – 83 (1985).
3. N.D. Raransky, V.P. Shafraniuk, and I.M. Fodchuk, X-ray Interferometric Image of Strain Fields around Dislocation Clusters, *Metal Physics* 7(5), 63 – 71 (1985).
4. N.D. Raransky, V.P. Shafraniuk, Defects of Interface Boundaries and Stress Relaxation of Si-Si, Ge-Si, GaP-Si Epitaxial Systems, *Ukrainian J. Physics* 30 (1), 127 – 132 (1985).
5. V.P. Shafraniuk, Potential of X-Ray Diffraction Interferometry in Studying the Relaxation of Local Mechanical Stresses in the Subsurface Layers of Single Crystals, *Scientific Bulletin of Chernivtsi National University, Physics*, issue 32, 122 – 127 (1998).
6. N.D. Raransky, Ya.M. Struk, I.M. Fodchuk, V.P. Shafraniuk, and A.N. Raransky, Applied Possibilities of X-Ray Diffraction Interferometry, *Proc.SPIE -Bellingham* 2647, 457 – 467 (1995).
7. V.P. Shafraniuk, Determination of Structural Changes and Temperature Distribution within Crystals, *J. Thermoelectricity* 3, 89 – 94 (1998).
8. I.M. Fodchuk, M.D. Raransky, Ya.M. Struk, I.V. Fesiv, et al., Moire Images of Defects in X-ray Three-Crystal Interferometry, *Scientific Bulletin of Chernivtsi National University. Physics*, issue 92, 14 – 19 (2000).

Submitted 04.11.2016

---

**E.I. Rogacheva, K.V. Martynova, A.S. Bondarenko**

National Technical University “Kharkiv Polytechnic Institute”,  
2, Kirpicheva Str, Kharkiv 61002, Ukraine

**THERMOELECTRIC AND MECHANICAL PROPERTIES  
OF  $(Bi_{1-x}Sb_x)_2Te_3$  ( $x = 0 \div 0.07$ ) SEMICONDUCTOR SOLID SOLUTIONS**

---

*The dependences of thermoelectric properties and microhardness on the composition of polycrystalline  $(Bi_{1-x}Sb_x)_2Te_3$  solid solutions in the concentration range  $x = 0 \div 0.07$  at room temperature were investigated. A drastic growth of microhardness was discovered with a simultaneous reduction of the Hall coefficient, the Seebeck coefficient and electric conductivity with increase in antimony content  $x = 0.005 - 0.01$ , following which with further increase in  $x$  to  $x = 0.01 - 0.015$ , the type of the dependences was reversed. The observed effect is attributable to a high degree of crystal lattice disorder with the introduction of the first portions of impurity and to subsequent relaxation processes with formation of percolation channels in crystal impurity subsystem. With further increase in  $x$ , the Hall coefficient and the Seebeck coefficient practically do not change with composition, and the observed more complicated dependence of microhardness and electric conductivity on  $x$  is interpreted as a manifestation of short-range processes in a solid solution.*

**Key words:**  $(Bi_{1-x}Sb_x)_2Te_3$  solid solution, composition, room temperature, thermoelectric properties, microhardness, percolation.

## Introduction

Today semiconductor solid solutions of bismuth and antimony telluride  $(Bi_{1-x}Sb_x)_2Te_3$  are among the most efficient thermoelectric (TE) materials widely used for the purposes of TE cooling at close to room temperatures [1 – 4].

The  $Bi_2Te_3$  and  $Sb_2Te_3$  compounds and a continuous series of  $(Bi_{1-x}Sb_x)_2Te_3$  solid solutions between them crystallize in a rhombohedral lattice of tetradymite type based on a nine-layer package of  $Bi(Sb)$  and  $Te$  atoms and characterized by considerable anisotropy of properties. To describe the zone structure of these compounds, use is usually made of a six-ellipsoid model of isoenergetic surface with ellipsoid centres on symmetry planes, which is in fairly good agreement with the experimental data [1 – 5]. The maximum on the liquidus and solidus curves close to  $Bi_2Te_3$  compound in  $Bi-Te$  system is shifted from stoichiometric composition towards  $Bi$  excess and at congruent melting temperature corresponds, according to different authors, to compositions: 59.935 at %  $Te$  [6], 59.95 at %  $Te$  [7] and 59.8 at %  $Te$  [8].

The data of various authors regarding the boundaries of  $Bi_2Te_3$  homogeneity area at high temperatures (700 – 850 K) are in good agreement with each other: (59.4 – 59.92) – (60.05 – 60.35) at %  $Te$  [2, 6 – 9]. The range of  $Bi_2Te_3$  homogeneity area in  $Bi-Te$  system, determined in [10] for the samples prepared by the procedure similar to that used here corresponded to 59.5 – 61 at %  $Te$ . The basic types of defects in stoichiometric  $Bi_2Te_3$  and  $Sb_2Te_3$  and  $(Bi_{1-x}Sb_x)_2Te_3$  solid solutions are antisite defects  $Bi_{Te}$  and  $Sb_{Te}$ , formed by substitution of tellurium vacancies by  $Bi$  and  $Sb$  atoms [6, 11]. In [10] it was shown that with a deviation from stoichiometric composition (60 at %  $Te$ )

both toward *Bi* excess and *Te* excess there is growth of microhardness  $H$  and electric conductivity  $\sigma$  and drop of the Seebeck coefficient  $S$  and the Hall coefficient  $R_H$  which was attributed by the authors [10] to introduction to crystals of nonstoichiometry defects increasing carrier concentration and the level of stress in the lattice. It was established that with stoichiometric composition (60 at % *Te*) and with a deviation from it toward *Bi* excess the *p*-type conductivity is observed.

In recent years it has been established that  $Bi_2Te_3$  and  $Sb_2Te_3$  compounds refer to a new class of objects in solid state physics, namely 3D-topological insulators, where strictly spin-oriented surface electrons are not scattered by defects and can move along the surface of the bulk material almost without energy loss. Thanks to protection of surface states, the topological insulators hold good promise for practical applications in spintronics, quantum computers, thermoelectricity and other fields [12 – 14]. As long as it is rather difficult to single out the contribution to conductivity of surface layer, one of the tasks is to reduce the contribution to conductivity of the bulk component, which can be done by doping of material in order to reduce charge carrier concentration. Therefore, the works studying the effect of impurities on carrier concentration in  $Bi_2Te_3$  and  $Sb_2Te_3$  are of current interest.

Studies of TE properties of *Bi-Sb-Te* ternary system in the cut of  $Bi_2Te_3$ - $Sb_2Te_3$  were performed by many authors (see, for instance, [15 – 22]). However, practically in all the works the samples were made with a big step of impurity component concentration, which prevented from making a thorough investigation of properties behaviour with composition.

Earlier in many works (see, for instance, [23 – 32]) for a number of semiconductor and semimetallic solid solutions it was discovered that in the area of low impurity content (up to ~ 1 at %) the concentration anomalies were observed on the composition dependences of properties. The authors of these works attributed these peculiar properties to the fact that in going from dilute to concentrated solid solutions there is phase transition of percolation type, accompanied by critical phenomena and having a universal character, i.e. inherent in any solid solutions [31, 32]. As long as the presence of phase transition generally results in considerable change of properties, it is very important to take this effect into account in the development of efficient TE materials, since one of the main ways for modification of TE material properties is formation of solid solutions and doping.

When using semiconductor materials in TE devices, certain demands are placed on mechanical properties. Doping for the purpose of improving TE figure of merit is accompanied by modification of not only thermoelectric, but also mechanical properties, and the character of this modification should be known. One of informative mechanical characteristics is microhardness, i.e. characteristic of material strength under conditions of combined stress arising at introduction of indenter [33]. As long as between  $H$  and other mechanical characteristics of crystal there is a definite link, by the value of  $H$  one can estimate the value of hardening without taking tension (compression) – stress diagram.

In connection with the above, it was interesting to study TE and mechanical properties depending on the composition of  $(Bi_{1-x}Sb_x)_2Te_3$  solid solutions prepared under identical process conditions, in the area of low content of the second component. As the object of study,  $(Bi_{1-x}Sb_x)_2Te_3$  solid solution in the concentration range  $x = 0 \div 0.07$  was chosen, and as the properties under study –  $H$ ,  $R_H$ ,  $S$  and  $\sigma$ .

From the results obtained in this paper it follows that with a detailed study of the properties of polycrystalline cast samples of  $Bi_2Te_3$  solid solutions in  $(Bi_{1-x}Sb_x)_2Te_3$  system one can find concentration anomalies of properties in the range of low concentrations of introduced impurity component ( $Sb_2Te_3$ ).



## Experimental procedure

Polycrystalline cast samples of  $(Bi_{1-x}Sb_x)_2Te_3$  ( $x = 0 - 0.07$ ) solid solutions with concentration step  $\Delta x$  from 0.0025 to 0.01 were obtained from high-purity (at least 99.999 % of basic component) elements (*Bi*, *Sb* and *Te*) by melting them in evacuated to  $10^{-3}$  Pa quartz ampoules at temperature  $(1020 \pm 10)$  K, holding in the melt for 5 hours with the use of vibratory agitation, cooling to temperature  $(650 \pm 10)$  K, holding at this temperature for 300 hours for homogenization of alloys and obtaining compositionally uniform ingots and subsequent cooling at a rate of switched off furnace. All 20 samples of various compositions were synthesized and subject to thermal treatment simultaneously, during one process cycle, which assured the identity of their preparation conditions and the possibility of comparing the properties of samples of various compositions.

Quantitative chemical analysis of obtained samples was performed by the methods of X-ray fluorescent analysis and electron-microprobe analysis. X-ray fluorescent analysis was conducted on X-ray fluorescent spectrometer SPRUT. The area of irradiated surface was  $\sim 12$  mm<sup>2</sup>. The accuracy of the method was  $\approx 0.2 - 0.5$  %. Electron microprobe analysis was conducted on scanning electron microscope JSM-6390LV (Jeol Ltd., Japan), with a system of energy-dispersive spectrometer INCA Energy 350 (Oxford Instruments Analytical Ltd., Great Britain). Control weighing of ingots after synthesis and thermal treatment, as well as the above set of quantitative chemical analysis methods showed that the deviation of alloy composition from the calculated one in all the elements did not exceed  $\Delta x = 0.0002$ .

The degree of uniformity of obtained samples was also controlled by methods of local measurements of  $H$  and  $S$  on the samples cut of the same ingot in two mutually perpendicular directions. The size of microprobe for measurement of  $S$  was  $\approx 100$   $\mu$ m, and the size of print in the measurement of  $H$  did not exceed  $\approx 10$   $\mu$ m. The spread in the values of measured parameters in the sample did not exceed their measurement error, which, on the one hand, pointed to isotropy of polycrystalline material, and, on the other hand, to its uniformity.

Microhardness  $H$  was measured at room temperature on PMT-3 instrument using a diamond pyramid under load  $P = 0.49$  N. The choice of load value was made by constructing the dependences  $H(P)$  for each sample and determining the value of  $P$  following which  $H$  ceases to depend on  $P$ . It was established that microhardness decreases with an increase in  $P$  (a scale effect takes place), but the values of  $H$  are practically independent of  $P$ , starting from  $P = 0.49$  H, and under these conditions  $H$  is an objective characteristic of sample strength properties. The times of loading, holding under load and load removal made 10 s. Adjustment of the instrument was done with the aid of freshly cleaved *NaCl* crystals. The values of  $H$  were obtained as the arithmetical mean when measuring 30 prints. Statistical treatment of measured results showed that the value of relative mean-square fluctuation of a series of 30  $H$  measurements did not exceed 2 – 3 %. Determination of  $\sigma$  and  $R_H$  to an accuracy not less than  $\pm 5$  % was performed using the van der Pauw method with magnetic field induction  $B = 1$  T. The Seebeck coefficient was measured by compensation method with respect to copper electrodes to an accuracy of  $\pm 3$  %. The concentration of charge carriers (holes)  $p$  was calculated by the formula  $p = r/(e \cdot R_H)$ , assuming that the Hall factor is  $r = 1$ .

With a strong degeneracy (which takes place in this case) a relation between carrier concentration and the Seebeck coefficient is expressed by the formula [3]

$$S = \left( \delta + \frac{3}{2} \right) \frac{2\pi^{2/3} k^2 T m^*}{3^{5/3} e \hbar^2 p^{2/3}}, \quad (1)$$

where  $m^*$  is effective mass;  $p$  is charge carrier concentration;  $\delta$  is coefficient depending on scattering mechanism (for  $(Bi_{1-x}Sb_x)_2Te_3$  solid solutions  $\delta = 0$  [3]). From formula (1) by the obtained value of  $S$  for  $Bi_2Te_3$ , taking into account that  $m^* = 0.34 m$  [3] and  $T = 300$  K, one can obtain the concentration of charge carriers (holes). The calculated value of  $p$  ( $p = (1.25 \pm 0.05) \cdot 10^{19} \text{ cm}^{-3}$ ) for  $Bi_2Te_3$  is in good agreement with the value of  $p$  measured by the Hall effect method, as well as with the data reported in the literature. The same situation was observed for all investigated alloys.

The value of TE power  $P$  was determined by the formula  $P = S^2\sigma$ .

### Experimental results

Fig. 1 shows the composition dependence of  $H$  which is apparently of a complex type. On introducing to  $Bi_2Te_3$  of the first portions of  $Sb_2Te_3$  up to  $x = 0.0075$  there is a sharp (almost 1.5 times) increase in  $H$ . With a further increase of  $x$  to  $x = 0.015$ , microhardness drastically drops to the value close to  $H$  value of the initial component ( $Bi_2Te_3$ ). Later, with increase in  $x$ , there is again growth of  $H$  to  $x = 0.025$ , following which  $H$  is reduced to  $x = 0.04$ . In the composition range  $x = 0.04 \div 0.07$  there is a minor increase in microhardness. The type of the dependence  $H(x)$ , unusual for solid solutions, points to qualitative changes in crystal defective subsystem with increasing concentration of  $Bi$ . Note that  $H$  value of the initial bismuth telluride ( $H = 0.35 \pm 0.01$  GPa) is somewhat lower than the values cited in a number of papers for single crystals and polycrystals (0.5 – 0.95 GPa) [34 – 37]. The difference may be due to the difference in sample manufacturing technique and, accordingly, their structural state, the methods for measuring  $H$  (for instance, different load on the indenter), the quality of sample surface preparation for measuring  $H$ . Moreover, in [10] it was shown that TE properties and microhardness are extremely sensitive to deviation from stoichiometric composition which is matched by minimum  $H$  values and maximum  $S$ ,  $\sigma$  and  $R_H$  values.

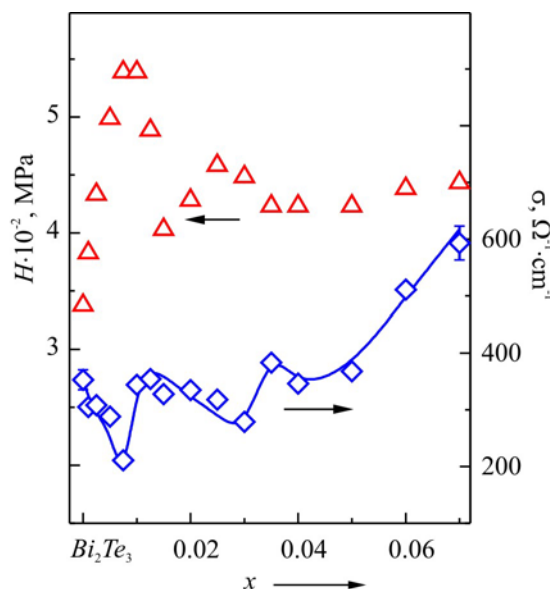


*Fig. 1. Dependences of microhardness  $H$  and electric conductivity  $\sigma$  on composition  $x$  of polycrystalline  $(Bi_{1-x}Sb_x)_2Te_3$  solid solutions at 300 K.*

All samples under study had  $p$ -type conductivity, just as the initial polycrystal of stoichiometric  $Bi_2Te_3$ . Fig. 2 shows the dependences  $R_H(x)$  and  $S(x)$ . It can be seen that the type of the dependences is similar for both kinetic coefficients: in the range  $x = 0 \div 0.005$  there is a decrease in  $R_H$  and  $S$  values, then up to  $x = 0 \div 0.01$  they increase and further  $R_H$  and  $S$  values are practically unchanged.

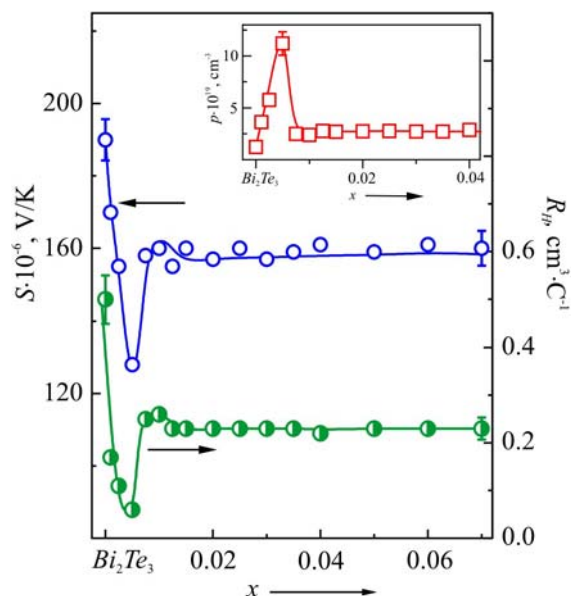


Fig. 2. Dependences of the Seebeck coefficient  $S$  and the Hall coefficient  $R_H$  on composition  $x$  of polycrystalline  $(\text{Bi}_{1-x}\text{Sb}_x)_2\text{Te}_3$  solid solutions at 300 K. The inset: Dependence of hole concentration  $p$  on composition  $x$  of  $(\text{Bi}_{1-x}\text{Sb}_x)_2\text{Te}_3$  solid solutions at temperature 300 K.

By the  $R_H$  values, on the assumption of one sort of charge carriers, the hole concentration  $p$  was calculated, the composition dependence of which is given in the insert to Fig. 2. With increase in  $x$  to  $x = 0.005$ , the value of  $p$  grows, increasing by almost an order, then up to  $x = 0.01$  – drops, following which it is practically unchanged. The simplest calculation shows that in the area  $x = 0 \div 0.005$  each antimony atom which substitutes  $\text{Bi}$  atom introduces additionally  $(0.65 \pm 0.05)$  charge carriers (holes).

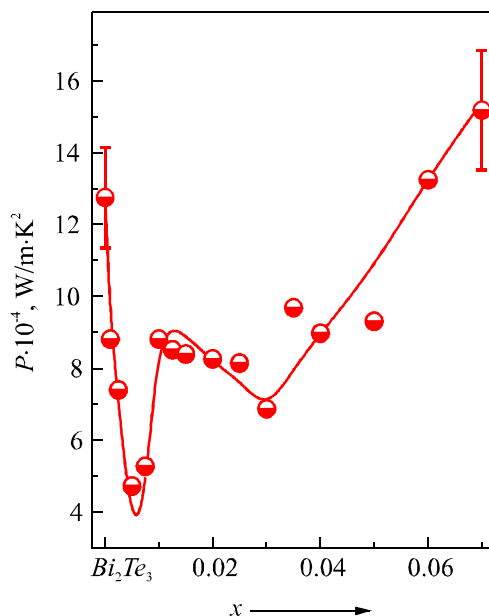


Fig. 3. Dependence of thermoelectric power  $P = S^2 \cdot \sigma$  on composition  $x$  of polycrystalline  $(\text{Bi}_{1-x}\text{Sb}_x)_2\text{Te}_3$  solid solutions at 300 K.

Electric conductivity changes with composition in a complicated way (Fig. 1). At first, on introducing of  $\text{Sb}_2\text{Te}_3$  (up to  $x = 0.0075$ ),  $\sigma$  drastically decreases, then in the range

$x = 0.0075 \div 0.0125$  there is growth of electric conductivity, following which  $\sigma$  again drops to  $x \sim 0.03$  and then grows up to  $x = 0.07$ . The composition dependence of TE is of similar type (Fig. 3).

From the obtained experimental data it follows that the dependences of properties on the composition of  $(Bi_{1-x}Sb_x)_2Te_3$  solid solutions in the concentration range adjacent to bismuth telluride are of a pronounced non-monotonic type.

### Discussion of the results

As long as  $Sb_2Te_3$  compound is isovalent and isomorphic impurity for  $Bi_2Te_3$ , and both compounds form a continuous series of solid solutions, it might be expected that the composition dependences of various properties will represent smooth curves. Such assumption agrees with the data from a number of works [17 – 22] which indicated a continuous decrease of  $R_H$  and  $S$ , as well as growth of  $\sigma$  in going from  $Bi_2Te_3$  to  $Sb_2Te_3$ . However, these works studied few alloys of different composition over a wide concentration range. Therefore, a complex type of concentration dependences of properties discovered in this paper in the range  $x = 0 \div 0.07$  demands explanation.

It is known that introduction of impurity forming a solid solution is practically always accompanied by  $H$  increase. The theories of solid solution strengthening generally deal with a case of dilute solid solutions and show that the composition dependence of  $H$  is close to linear [38 – 40]. From the standpoint of modern concepts, mechanical properties of crystal are largely determined by dislocation mobility [38], and the root cause for strengthening is elastic interaction of dislocations with the dissolved impurity atoms which block dislocation motion. In the region of dilute solid solutions the elastic deformation fields created by individual impurity atoms practically do not overlap, each impurity atom introduces an additive contribution to  $H$  value, and the main parameters governing the degree of change in  $H$  are concentrations of point defects and the bonding energy of point defect and dislocation. The elastic interaction between dislocations and impurities leads to reduction of dislocation mobility and, hence, to strengthening. So, growth of  $H$  with the introduction of the first portions of  $Sb_2Te_3$  (to  $x = 0.0075$ ) does not require special explanation. However, a drastic drop of  $H$  at  $x = 0.0075$ , pointing to a change in the character of dislocation motion, increase of their mobility and crystal weakening, cannot be explained within the theories of solid solution strengthening.

In a number of earlier works by one of the present authors, weakening defect was discovered in the region of low impurity concentrations [23, 26, 29, 31 – 32] and within percolation theory [41 – 42] weakening mechanism was proposed related to collective interaction of deformation fields of impurity atoms, when concentration of the latter reaches percolation threshold – critical value of  $x_c$  corresponding to formation of “infinite cluster” – a single chain of overlapping deformation fields that penetrates crystal. Formation of “infinite cluster” on achievement of percolation threshold  $x_c$  can be regarded as a phase transition accompanied by critical phenomena.

Assuming that composition with  $x = 0.005$  corresponds to percolation threshold, and using the conclusions obtained from solving the problem of spheres of percolation theory [41 – 42], one can estimate the size of deformation sphere  $R_0$  by the formula:

$$\frac{4}{3}\pi N_c (2R_0)^3 \approx 2.7, \quad (2)$$

where  $N_c$  is the number of sphere centres in the unit volume with the composition of  $(Bi_{1-x}Sb_x)_2Te_3$  solid solution corresponding to percolation threshold ( $x = x_c$ ). Simple calculation shows that  $R_0 = (2.7 \pm 0.05) a_0$ , where  $a_0$  is quasi-cubic parameter of  $Bi_2Te_3$  unit cell, which agrees with the short-range character of deformation interaction.

A sharp increase in hole concentration with small additions of  $Sb_2Te_3$  ( $x = 0 - 0.005$ ) and a simultaneous drastic increase in  $H$  and decrease of  $\sigma$  testify to considerable deformation of crystal lattice and the appearance of additional electrically active centres. In this connection, it can be assumed that the first portions of  $Sb_2Te_3$  do not enter crystal lattice by the mechanism of simple cationic substitution, and formation of solid solution is accompanied by the appearance of additional antisite defects. Because of deviation from stoichiometry toward  $Bi$  excess (the maximum on fusion curves in  $Bi-Te$  system is shifted from stoichiometric composition), the stoichiometric  $Bi_2Te_3$  comprises a certain equilibrium concentration of defects, mainly antisite  $Bi_{Te}$  defects. With the introduction to bismuth telluride of the first portions of  $Sb_2Te_3$ , conditions of thermodynamic equilibrium change, which can lead to increase in equilibrium concentration of antisite defects in  $Bi_2Te_3$ . From the thermodynamic standpoint for the emerged  $Sb$  it is more favourable to occupy antisite positions, owing to which hole concentration increases. However, it is valid so long as antimony atoms practically do not interact with each other. After formation of percolation channels the situation changes and interaction energy begins to contribute to the expression for free energy, changing thermodynamic equilibrium conditions and leading to a decrease in the equilibrium concentration of defects.

This assumption is supported by the fact that in the concentration range  $x = 0 - 0.005$  each  $Sb$  atom supplies  $(0.65 \pm 0.05)$  holes, which corresponds to formation of acceptor-type antisite defects ( $Bi_{Te}$  or  $Sb_{Te}$ ) [43]. It is also noteworthy that increase in the assortment and number of structural defects with a low impurity content, when interaction of impurity atoms between each other can be ignored, is stimulated by a sharp increase in configuration entropy, which with the introduction of the first portions of impurity is not compensated by simultaneous growth of crystal internal energy. As long as bonding energy of impurity atom is less than that of the host atom (at least in the region of low impurity concentration), the antisite defects will be primarily formed by impurity atoms.

Achievement of percolation threshold stimulates self-organization processes in the subsystem of defects which in the presence of corresponding thermodynamic stimuli can lead to formation of ordered phase. In this case the weakening effect must be particularly significant. A sharp decrease in  $H$  and  $p$  with a simultaneous growth of  $\sigma$  suggest that ordering processes in all likelihood take place.

After passing of crystal to a qualitatively new state related to formation of percolation channels ("impurity condensate"), new centres appear that impede dislocation motion, and  $H$  again grows with increase in antimony concentration.

Further increase in  $x$  increases the likelihood of Coulomb interaction between the introduced unlike charged ions  $Sb^{+3}$  and  $Te^{+2}$  which stimulates the process of chemical interaction with formation of electrically neutral  $Sb_2Te_3$  complexes. As long as the concentration of complexes is low, they do not interact with each other, but as their concentration increases, flow channels are formed in the crystal through the resulting complexes. The presence of the second anomalous portion of  $H$  drop and  $\sigma$  growth with increase in  $x$  in the range  $x = 0.025 - 0.04$  can be related to achievement of "complex formation threshold", when flow channels through neutral molecular complexes  $Sb_2Te_3$  are formed, leading to a qualitative change of properties [44].

Thus, the composition dependences of both  $H$  and TE properties testify to complex defect forming processes taking place in  $Bi_2Te_3$  crystal lattice with the introduction of  $Sb_2Te_3$ .

One should take into account possible influence of kinetic factors. For a long time (300 hours) the alloys were annealed at 650 K, with high probability of their coming to a state close to equilibrium at this temperature, following which they were cooled to temperature 300 K at a rate of furnace turned

off. Taking into account low diffusion rate at close to room temperatures and low concentration of impurity atoms not interacting with each other, it can be assumed that in the range of the lowest concentrations of impurity component, in view of incompleteness of diffusion processes, high-temperature states are recorded that correspond to annealing temperature and are oversaturated with defects. In this case, formation of percolation channels can drastically increase the rate of diffusion processes and transfer the alloy oversaturated with defects to a more equilibrium state. A sharp decrease in  $H$  and a sharp increase in  $R_H$ ,  $S$  and  $\sigma$  with  $x$  increase above  $x = 0.01 - 0.015$  may indicate transition to equilibrium state from the nonequilibrium state formed as a result of oversaturation with defects and freezing of high-temperature state after accelerated cooling of alloys at a rate of furnace turned off. Therefore, it is desirable to study the effect of ageing processes on the properties of  $(Bi_{1-x}Sb_x)_2Te_3$  solid solutions in the range of low concentration of  $Sb_2Te_3$  in order to reveal the role of kinetic factors in the character of manifestation of percolation effects.

## Conclusion

Analysis of the results of detailed investigation of the composition dependences of thermoelectric and mechanical properties of polycrystalline  $(Bi_{1-x}Sb_x)_2Te_3$  ( $x = 0 - 0.07$ ) solid solutions has shown that the concentration dependences of microhardness, the Seebeck coefficient, the Hall coefficient, electric conductivity and thermoelectric power are of a pronounced non-monotonic type.

A drastic increase in microhardness and carrier concentration with a simultaneous decrease in the Seebeck coefficient and electric conductivity values with the introduction of the first impurity portions (up to  $x = 0.005 - 0.01$ ) is related to high degree of crystal lattice disorder and increase in the concentration of antisite defects, and the reversal of the type of the dependences with further increase in  $x$  – to change in thermodynamic equilibrium conditions on achievement of percolation threshold and formation of “infinite cluster”. It is assumed that this percolation-type transition from dilute to concentrated solid solutions is accompanied by self-organization processes in crystal impurity subsystem.

Anomalies on the concentration dependences of microhardness and electric conductivity in the range  $x = 0.025 - 0.04$  are connected with transition to associated solid solutions.

An assumption was made on the influence of kinetic factors on the type of composition-property dependence at low impurity concentrations because of the possibility of freezing high-temperature states corresponding to annealing temperature as a result of rapid cooling to room temperature and insufficient time for completion of diffusion processes.

The obtained results prove the earlier assumptions on the universal character of solid solutions behaviour in the low concentration range of impurity component – the presence of concentration anomalies of properties related to transition from dilute to concentrated solid solutions. The discovered effects must be taken into account in the development of methods for improving the thermoelectric efficiency of materials by forming solid solutions and doping.

## References

1. L.I. Anatychuk, *Thermoelements and Thermoelectric Devices: Reference Book* (Kyiv: Naukova Dumka, 1979), 768 p.
2. H. Scherrer, Bismuth Telluride, Antimony Telluride and their Solid Solution in: *CRC Handbook of Thermoelectrics ed. by D.M. Rowe* (London, New York, Washington: CRC Press, Boca Raton, D.C., 1995), p. 213 – 223.

3. B.M. Goltsman, V.A. Kudinov, and I.A. Smirnov, *Semiconducting Thermoelectric Materials Based on  $\text{Bi}_2\text{Te}_3$*  (Moscow: Nauka, 1972), 320 p.
4. L.E. Bell, Cooling, Heating, Generating Power, and Recovering Waste Heat with Thermoelectric Systems, *Science* 321, 1457 – 1467 (2008).
5. J.R. Drabble, Galvanomagnetic Effects in Bismuth Telluride, *Journal of Physics and Chemistry of Solids* 8, 1101 – 1108 (1959).
6. G. Offergeld and J. Van Cakenberghe, Determination de la Composition a Fusion Congruente de Semiconducteurs Binaires par Analyse Thermique Differentielle Application a  $\text{Bi}_2\text{Te}_3$ ,  $\text{Sb}_2\text{Te}_3$  et  $\text{Bi}_2\text{Se}_3$ , *J. Phys. Chem. Sol.* 11, 310 – 314 (1959).
7. R.F. Brebrick, Homogeneity Ranges and  $\text{Te}_2$  – Pressure along the Three – Phase Curves for  $\text{Bi}_2\text{Te}_3$  and a 55 – 58 at % Te, Peritectic Phase, *J. Phys. Chem. Sol.* 30, 719 – 731 (1969).
8. A.C. Glatz, An Evaluation of the Bismuth-Tellurium Phase System, *J. Electrochem. Soc.* **112** (12), 1204 – 1207 (1965).
9. C.B. Satterthwaite and R.W. Ure, Electrical and Thermal Properties of  $\text{Bi}_2\text{Te}_3$ , *Phys. Rev.* 108, 1164 – 1170 (1957).
10. E.I. Rogacheva, A.V. Budnik, O.S. Vodorez, and M.V. Dobrotvorskaya, Effect of Nonstoichiometry on the Thermoelectric and Mechanical Properties of  $\text{Bi}_2\text{Te}_3$  Polycrystals, *J. Thermoelectricity* 6, 42 – 51 (2014).
11. G.R. Miller and Che-Yu Li, Evidence for the Existence of Antistructure Defects in Bismuth Telluride by Density Measurements, *J. Phys. Chem. Sol.* 26, 173 – 177 (1965).
12. J.E. Moore, The Birth of Topological Insulators, *Nature* 464, 194 – 198 (2010).
13. M.Z. Hasan and C.L. Kane, Colloquium: Topological insulators, *Rev. Mod. Phys.* 82, 3045 – 3067 (2010).
14. Y.L. Chen, J.G. Anaiytis, J.-H. Chu, et al., Experimental Realization of a Three-Dimensional Topological Insulator,  $\text{Bi}_2\text{Te}_3$ , *Science* 325, 178 – 181 (2009).
15. S.V. Airapetiants, B.A. Yefimova, Thermoelectric Properties and Character of Bonds of  $\text{Bi}_2\text{Te}_3$ - $\text{Sb}_2\text{Te}_3$  System, *Zhurnal Tekhnicheskoi Fiziki* 28, 1768 – 1774 (1958).
16. M.J. Smith, R.J. Knight, and C.W. Spencer, Properties of  $\text{Bi}_2\text{Te}_3$ - $\text{Sb}_2\text{Te}_3$  Alloys, *J. Applied Physics* **33** (7), 2186 – 2190 (1962).
17. L.R. Testardi, J.N. Bierly, and F.J. Donahoe, Transport Properties of *p*-Type  $\text{Bi}_2\text{Te}_3$ - $\text{Sb}_2\text{Te}_3$  in the Temperature Range 80 – 370 K, *J. Physics and Chemistry of Solids* 23, 1209 – 1217 (1962).
18. G.V. Kokosh and S.S. Sinani, Thermoelectric Properties of Alloys of Pseudo-Binary  $\text{Sb}_2\text{Te}_3$ - $\text{Bi}_2\text{Te}_3$  System, *Physics of the Solid State* **2** (6), 1118 – 1124 (1960).
19. C.H. Champness, P.T. Chiang, and P. Parekh, Thermoelectric Properties of  $\text{Bi}_2\text{Te}_3$ - $\text{Sb}_2\text{Te}_3$  Alloys, *Canadian Journal of Physics* **43** (4), 653 – 669 (1965).
20. H.-W. Jeon, H.-P. Ha, and D.-B. Hyun, Electrical and Thermoelectrical Properties of Undoped  $\text{Bi}_2\text{Te}_3$ - $\text{Sb}_2\text{Te}_3$  and  $\text{Bi}_2\text{Te}_3$ - $\text{Sb}_2\text{Te}_3$ - $\text{Sb}_2\text{Se}_3$  Single Crystals, *J. Physics and Chemistry of Solids* **52** (4), 579 – 585 (1991).
21. L.D. Ivanova and Yu.V. Granatkina, Thermoelectric Properties of  $\text{Bi}_2\text{Te}_3$ - $\text{Sb}_2\text{Te}_3$  Single Crystals in the Range 100 – 700 K, *Inorganic Materials* 36, 672 – 677 (2000).
22. L.D. Ivanova and L.I. Petrova, Thermoelectric Materials Based on  $\text{Sb}_2\text{Te}_3$ - $\text{Bi}_2\text{Te}_3$  Solid Solution with Optimal Performance in the Range 100 – 400 K, *Inorganic Materials* **43** (9), 933 – 937 (2007).
23. E.I. Rogacheva, Concentration-Dependent Microhardness in Semiconductor Solid Solutions, *Izv. AN SSSR. Neorgan. Mater* **25**(5), 643 – 646 (1989).
24. E.I. Rogacheva, N.A. Sinelnik, and O.N. Nashchekina, Concentration Anomalies of Properties in

- Pb<sub>1-x</sub>Ge<sub>x</sub>Te*, *Acta Phys. Pol 84A* (4), 729 – 732 (1993).
25. E.I. Rogacheva, I.M. Krivulkin, V.P. Popov, and T.A. Lobkovskaya, Concentration Dependences of Properties in *Pb<sub>1-x</sub>Mn<sub>x</sub>Te* Solid Solutions, *Phys. Stat. Sol. (a)* **148**(2), p. K65 – K67(1995).
  26. E.I. Rogacheva, A.S. Sologubenko, and I.M. Krivulkin, Microhardness of *Pb<sub>1-x</sub>Mn<sub>x</sub>Te* Semimagnetic Solid Solutions, *Inorganic Materials* **34**, 545 – 549 (1998).
  27. E.I. Rogacheva, V.I. Pinegin, and T.V. Tavrina, Percolation Effects in *Pb<sub>1-x</sub>Ge<sub>x</sub>Te*, *Proc. SPIE* **3182**, 364 – 368 (1998).
  28. E.I. Rogacheva, I.M. Krivulkin, Concentration Anomaly of Heat Capacity in the *Pb<sub>1-x</sub>Mn<sub>x</sub>Te* Semimagnetic Semiconductors, *Institute of Physics Conference Series* **152**, 831 – 834 (1998).
  29. E.I. Rogacheva, T.V. Tavrina, and I.M. Krivulkin, Anomalous Composition Dependence of Microhardness in *Pb<sub>1-x</sub>Ge<sub>x</sub>Te* Semiconductors Solid Solutions, *Inorganic Materials* **35**, 236 – 239 (1999).
  30. E.I. Rogacheva, A.A. Drozdova, and O.N. Nashchekina, Percolation Effects in Semimetallic *Bi-Sb* Solid Solutions, *Phys. Stat. Sol. (a)* **207**(2), 344 – 347 (2010).
  31. E.I. Rogacheva, Critical Phenomena in Heavily-Doped Semiconducting Compounds, *Jpn. J. Appl. Phys* **32** (32-3), 775 – 777 (1993). E.I. Rogacheva, Percolation Effects and Thermoelectric Materials Science, *J. Thermoelectricity* **2**, 61 – 72 (2007).
  33. V.K. Grigorovich, Hardness and Microhardness of Metals (Moscow: Nauka, 1976), 230 p. (in Russian).
  34. D. Arivuoli, F.D. Gnanam, and P. Ramasamy, Growth and Microhardness Studies of Chalcogenides of Arsenic, Antimony and Bismuth, *Journal of Materials Science Letters* **7**, 711 – 713 (1988).
  35. S. Augustine and E. Mathai, Dislocation, Annealing and Quenching Effects on the Microindentation Hardness of *Bi<sub>2</sub>Te<sub>3</sub>* and *Bi<sub>2</sub>Te<sub>2.9</sub>Se<sub>1</sub>* Single Crystal, *Materials Characterization* **52**, 253 – 262 (2004).
  36. J. Bhakti and V.S. Dimple, Structural Defects and Microindentation Analysis of Zone Melted *Bi<sub>2</sub>Te<sub>3-x</sub>Se<sub>x</sub>* Whiskers, *J. Crystal Growth* **352**, 143 – 146 (2012).
  37. J.W. Anthony, R.A. Bideaux, K.W. Bladh, and M.C. Nichols, *Handbook of Mineralogy Vol.1.* (California, Mineral Data Publishing, 1995), 458 p.
  38. T. Suzuki, H. Yoshinaga, and S. Takeuchi, *Dislocation Dynamics and Plasticity* (Moscow: Mir, 1989), p. 78 – 85.
  39. R.L. Fleischer, Substitutional Solution Hardening, *Acta Met.* **11**(3), 203 – 209 (1963).
  40. R.A. Labusch, Statistical Theory of Solid Solution Hardening in Concentrated Solutions, *J. Appl. Phys.* **39**(9), 4144 – 4151 (1968).
  41. B.I. Shklovskii and A.L. Efros, *Electronic Properties of Doped Semiconductors* (New York: Springer-Verlag, 1984), 388 p.
  42. D. Stauffer, A. Aharony, *Introduction to Percolation Theory* (London/Washington DC, Taylor & Francis, 1992), p.15 – 88.
  43. F.A. Kroger, On the Relation between Non-Stoichiometry and the Formation of Donor and Acceptor Centres in Compounds, *J. Phys. Chem. Solids* **7**, 276 – 278 (1958).
  44. E.I. Rogacheva, The Specificity of Structure and Electrical Behavior of Multinary Solid Solutions Formed by Chemical Compounds, *Physica Status Solidi C* **6**(5), 1307 – 1311 (2009).

Submitted 16.11.2016



---

**O.N. Manik, T.O. Manik, V.R. Bilinsky-Slotylo**

Yu.Fedkovich Chernivtsi National University,  
2 Kotsyubynsky str., Chernivtsi, 58012, Ukraine

**PECULIARITIES OF ELECTRONIC STRUCTURE  
OF HYBRID ORBITALS AND INTERATOMIC INTERACTION  
IN CADMIUM ANTIMONIDE CRYSTALS**

---

*This paper reports on the development of method and results of calculating parameters of electronic structure of hybrid orbitals corresponding to nonequivalent interatomic distances in cadmium antimonide crystals. On the basis of quantum-mechanical approach, calculations were made of effective charges, effective radii, as well as of the redistribution of electron density and dissociation energy of nonequivalent hybrid orbitals which can be used in the development of new CdSb-based materials with predicted properties.*

**Key words:** nonequivalent hybrid orbitals, effective radii, effective charges, dissociation energies.

## **Introduction**

Cadmium antimonide is a thoroughly studied semiconductor compound which is widely used in electronic equipment, and solid solutions on its basis are promising for application in thermoelectricity. The need for integrated research is due to the fact that the effect of interatomic interaction on the dynamics of chemical bond formation in low-symmetry crystals of rhombic syngony is poorly known.

In this connection, prediction of thermoelectric properties of *CdSb*-based semiconductor compounds by theoretical analysis of their electron structure is a strategic objective of materials science.

It should be noted that the attempts to create a quantitative method for calculating parameters of substance electronic structure on the basis of either strict quantum mechanical or empirical approach have not met with a success so far.

The experience of using different models taking into account concepts that are necessary for the construction of a theory shows that qualitatively new concepts should be introduced into statement of problem. To formulate them logically and mathematically, omitting generalization of experimental data does not seem possible.

Preliminary work on such generalization made within empirical approach [1 – 3] has shown that independent development of theoretical and empirical approaches must give way to a mixed method combining the advantages of quantum-mechanical method and the experience of crystal-chemical ways of studying the electronic structure of substance.

A combination of two different approaches in a single quantitative method is not a mechanical summation of any concepts or computational tricks. Theoretical comprehension of numerous empirical dependences is related to revision of established views, which is not always the result of development of the existing theories, and often denies some of them. Therefore, the way to solving the problem lies through analysis of empirical material and quantum-mechanical description of the relationship between the properties of elements and the compounds formed by them.

## Quantum-chemical models of electronic structure of elements and their compounds

According to quantum mechanics [4], analysis of electron density distribution reduces to calculation of wave function  $\psi$  the square of which  $\psi^2$  determines the possibility of electron position in the given region of the atom. A description of change in the values of  $\psi^2$  depending on the distance  $r$  to the nucleus yields information on electron cloud distribution, summarizing qualitatively in a new fashion the data on individual characteristics of electrons. Different form of their orbitals affects electron binding forces with a nucleus, allowing the use of the Fermi statistics according to which the probability of filling any state in the atom with energy  $E$ :

$$f(E) = \frac{1}{1 + \exp\left(\frac{E - E_F}{kT}\right)}, \quad (1)$$

where  $E_F$  is the Fermi energy corresponding to  $f(E_F) = 1/2$ ;  $k$  is the Boltzman constant;  $T$  is the absolute temperature/

Taking all this into account, in [5] it was assumed that at known dependences  $\psi^2 = f(r)$  for any element with different ionization degree, as well as at certain values of  $\psi_F^2$  and  $r_F$  (Fermi radii) the dependence of  $r_F$  on the number of electrons  $n$  in the orbitals characterizes electron configurations of interacting atoms depending on the length and number of the bonds they formed.

Attempts to connect together and generalize the analysis of versatile empirical information on the properties of atoms and their ions based on experience, as well as the existing theories and traditions of crystal-chemical approach were made in different scientific works. Thus, in [1 – 3], a study was conducted on the relationship between electronic properties and structure of semiconductor melts with the diagrams of state, classification of melts was made according to character of chemical bond. In [5 – 7], the empirical information on the properties of elements and the electronic structure of their compounds was analyzed from the standpoint of non-polarized ion radii  $R_{UH}$ . It was shown that both functions  $r_F = f(n)$  and equations relating  $R_{UH}$  to the charge of ions allow solving the same problem, namely to determine electronic configurations of interacting atoms depending on the length and number of the bonds they formed.

Thus, the necessity of construction of semi-phenomenological equations relating the value of  $R_U$  to the number of electrons  $n$  in atomic orbitals follows from the analysis of complications of modern quantitative theories of interatomic interaction.

The specific shape of such equation systems and their solutions will depend on the half-empirical concepts which will be involved. The simplest relationships were obtained by postulating the key dependence: with a change in the number of electrons in the outer shell of atom, the logarithm of its Fermi radius changes by rectilinear law [5]. In the search for graphical solution of the problem on the relation between  $R_U$  and  $n$ , the numerical values of electronegativities turned out to be the most useful. The relationship between the slope ratio of rectilinear dependences of logarithm  $R_U$  on  $n$   $\text{tg}\alpha = \frac{\Delta \lg R_U}{\Delta n}$  and electronegativity rules out the possibility of arbitrary variation of compared values.

A good agreement between the set of experimental data on various physical and chemical properties of atoms and their ions and the values  $R_U$  and  $\text{tg}\alpha$  is provided by the dependence

postulated in [6]:

$$\lg R_{UA}^x = \lg R_{UA}^o - x \operatorname{tg} \alpha, \quad (2)$$

where  $R_{UA}^o$  is radius of nonexcited-state atom, and  $x$  is valence.

Coefficients  $R_{UA}^o$  and  $\operatorname{tg} \alpha$  of (2)-type equations regularly change depending on the element position in periodic table.

Thus, the utility of (2)-type equations is determined by how much their use helps to avoid difficulties in modern theories of chemical bond and to obtain rather accurate and physically meaningful description of the results of interatomic interaction.

Chemical bond formation is accompanied by reconstruction of valence electron shells of interacting atoms owing to which spherical symmetry of their electron clouds is violated. However, with any type of bond the redistribution of electrons is performed so as to assure the continuity and smoothness of wave function which mates their ion cores.

As long as equations (2) describe a change in  $R_U$  of  $A$  and  $B$  atoms with a change in the number of electrons in the orbitals of each atom, the problem reduces to formulation of the condition of equality of  $\psi_A^2$  and  $\psi_B^2$  at point of  $\psi_{\min}^2$  with any length of  $A$ - $B$  bond.

On the assumption of equality of the absolute values of charges of interacting atoms, dependence (2) takes on the form of the system:

$$\lg R_{UA}^{+x} = \lg R_{UA}^o - x \operatorname{tg} \alpha_A \quad (3)$$

$$\lg R_{UB}^{-x} = \lg R_{UB}^o + x \operatorname{tg} \alpha_B \quad (4)$$

$$d_l = R_{UA}^{+x} + R_{UB}^{-x} \quad (5)$$

From the standpoint of quantum-mechanical approach to solution of chemical bond problem the system of equations (3) – (5) formally considers geometrical conditions of contact of spherical electron clouds with different density level at their boundary, i.e.  $\psi_{\min A}^2 + \psi_{\min B}^2$ . In so doing, a complicated process of reconstruction of electron shells of interacting atoms reduces to transfer of electrons from the orbitals of one atom to the orbitals of the other. Therefore, additional criteria are needed which will enable crystallochemical system of equations (3) – (5) to be put in terms of quantum chemistry.

For this purpose it was necessary to analyze a dependence of interatomic distances on effective charges:  $d_l = f(z_{\text{eff}})$ . It turned out that at any point of this dependence, except for  $d_l = d_{\min}$ , the density of states at the boundaries of ions is different. Moreover, to determine effective charges and corresponding effective atomic radii, in the bonds with  $d_l < d_{\min}$  it remains to use  $d_{\min}$  as parameters of the moment from which formation of ( $A$ - $B$ ) bond is accompanied by electron escape to other directions of interatomic interaction, i.e. the bond becomes donor. The values  $z_{\text{eff}}$  of atoms must be changed so as to assure the equality of density of states at the boundaries of corresponding atoms. This condition can be fulfilled in the case when removal of electrons ( $+\Delta q$ ) or their localization ( $-\Delta q$ ) in given bond direction equally change the values of charges that the given pair of atoms has at

$$d_l = d_{\min}, \text{ i.e. } z_{\text{eff}A(B)} = z_{\min A(B)} + \left( \frac{\Delta q}{2} \right).$$

Conditions of preserving wave function continuity in the zone of ion core interface of interacting atoms with this approach are given by equation system [6]:

$$d_1 = R_{UA}^{ZA} + R_{UB}^{ZB} \quad (6)$$

$$\lg R_{UA}^{ZA} = \lg R_{UA}^o - (z_{\min_A} + \Delta q / 2) \cdot \operatorname{tg} \alpha_A \quad (7)$$

$$\lg R_{UB}^{ZB} = \lg R_{UB}^o - (z_{\min_B} + \Delta q / 2) \cdot \operatorname{tg} \alpha_B \quad (8)$$

In outward appearance, systems of equations (6) – (8) and (3) – (5) do not differ in principle, but in reality substitution of  $x$  value by  $(z_{\min_{A(B)}} + \Delta q / 2)$  changes their physical meaning. Function  $d_1 = f(z_{\text{eff}})$ , calculated in conformity with traditions of crystallochemical approach ( $x_A = -x_B$ ), is correct from quantum-mechanical standpoint only at  $d_1 = d_{\min}$ , but this is enough for equation system (6) – (8) to be solved at known  $d_1$ .

This is the basis for derivation of the principles of using nonequivalent hybrid orbitals for the description of interatomic interaction and construction of rigid traceability charts of electron structure parameters and physico-chemical properties of the resulting compounds. This formulation of the problem brings to the forefront the regularities of decoding electron configurations of atoms along the length of the bond they formed. At the same time, in terms of nonequivalent hybrid orbitals, the type of structure and a set of interatomic distances must be the function of individual properties of interacting atoms. From this generalizing description follows that the difference in chemical bond nature (in terms of donor and acceptor determination in  $A - B$  pair) is a consequence of the action of uniform for all compounds regularities of electrons redistribution between partners to assure the continuity of wave function  $\psi$ .

The possibility of obtaining equations (6) – (8) opens up wide prospects for solution of prediction problems.

Also, the value of this information is that to obtain equations (6) – (8), it is sufficient to study the structure of two representatives of compound-analogs group, and for the rest of its members the necessary information can be obtained by calculation. Moreover, such calculations become relevant due to the fact that the boundaries of homogeneity area of defective phases are determined by the strength of their interatomic bond, and the possibilities of solving such problems on the basis of nonequivalent hybrid orbitals theory have not yet been studied.

### **Effective charges and effective radii of atoms of nonequivalent chemical bonds in cadmium antimonide crystals**

The specific feature of chemical bond in  $CdSb$  crystals is the fact that cadmium sublattice and antimony sublattice are displaced relative to each other. In so doing, each  $Cd$  atom in its immediate surrounding has three  $Sb$  atoms and one  $Cd$  atom, and each  $Sb$  atom has three nearest  $Cd$  atoms and one  $Sb$  atom. There are five nonequivalent chemical bond components altogether, which differ both in the interatomic distances and in the composition of components. Analysis of chemical bond models is given in [8].

To solve the formulated problem, it was necessary to write the system of equations (6) – (8) for each  $i$ -th nonequivalent hybrid orbital, and then by solving the inverse problem using known

interatomic distances  $d_i$  ( $1 \leq i \leq 5$ ) to find  $R_{U_{Cd}}, R_{U_{Sb}}, \Delta q$ .

A system of logarithmic transcendental equations was solved by variation method. An error  $\varepsilon \geq d_i^{exper} - d_i^{theor}$  was specified which in our case for all  $1 \leq i \leq 5$  did not exceed 0.01 %. The accuracy of calculations was restricted by the accuracy of experimental methods of finding interatomic distances.

The  $\text{tg}\alpha_{Cd}$  and  $\text{tg}\alpha_{Sb}$  necessary for generation of equation systems (6) – (8) were found by the method of [5]. As a result of calculations, the numerical values were obtained:

$$\text{tg}\alpha_{Cd} = 0.095; \quad \text{tg}\alpha_{Sb} = 0.076. \quad (9)$$

For the correct use of the formalism of nonequivalent hybrid orbital method, in the numerical calculations of this work a diagram  $d_i = f(z_i^{eff})$  was constructed.

The figure shows a dependence of interatomic distances  $d_i$  of c  $\varphi_i(Cd_x - Sb_{-x})$  bonds (in angstroms) on the effective charges  $x$  in the range of  $-4 < x < 4$ . As follows from the results, the minimum on this dependence is realized at  $d_{min} = 2.9271 \text{ \AA}$ , which exceeds real interatomic distances along the bonds  $\varphi_1(Cd - Sb)$ ,  $\varphi_2(Cd - Sb)$  and  $\varphi_3(Cd - Sb)$ . A similar situation is also observed for the bonds  $\varphi_4(Sb - Sb)$  and  $\varphi_5(Cd - Cd)$ . All this necessitated the recalculation of effective charges for each bond.

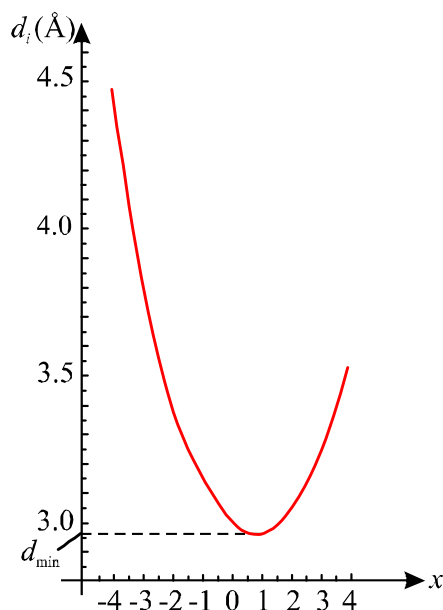


*Fig. Dependence of length  $d_i$  on the effective charges  $x$  of Cd and Sb bond  $\varphi_i(Cd_x - Sb_{-x})$ .*

Then, with regard to the above remarks, calculations of  $R_{USb}^i, R_{UCd}^i, \Delta e_i$  were performed for nonequivalent hybrid orbitals  $1 \leq i \leq 5$ . The advantage of this approach is that in a simple and uniform form for each compound type it generalizes information not only on the interatomic distances, but also on the parameters of electronic structure, i.e. at known  $\text{tg}\alpha$  and  $R^0$  a replacement of  $R_{UA}$  and  $R_{UB}$  by expressions (7) – (8) makes it possible to calculate  $\Delta q, z_{eff}, R_{U_{eff}}$  and  $d_1$ . From such generalizing

description it follows that the difference in chemical bond nature (from the standpoint of determination of donor and acceptor in  $(A - B)$  pair which is commonly referred to as “valence”) results from the action of uniform for all compounds regularities of electrons redistribution between partners to assure the continuity of wave function. In so doing, the value of accurate quantitative picture increases due to the fact that the dependences of dissociation energy of chemical bonds  $D = f(R_{UA} / R_{UB})$  have a clear physical meaning, since the ratio  $R_{UA} / R_{UB}$  determines the position and absolute value of  $\psi_{\min}$  in the inter-nuclear space.

Therefore, derivation of semi-empirical dependences that can be used to calculate bond energies between inhomogeneous atoms in dimensional molecular groups can be considered as one of important problems in nonequivalent hybrid orbital theory. The possibility of uniform physical interpretation of similar equations will be largely determined by achievements in the description of interaction of individual characteristics of atoms with the types and periods of structures formed by them. The results of study on interatomic interaction in compounds differing in stoichiometry, structure, supposed type of chemical bond and physical-chemical properties, give grounds to state that the use of nonequivalent hybrid orbitals for the description of conditions for wave function continuity between bond partners allows us to proceed to solving the tasks of prediction problem in materials science.

Thus, due to account of quantum-mechanical interpretation of empirical data by combining the concepts of different approaches – logically mathematical and experimental – in a uniform quantitative method for calculation of parameters of substance electronic structure, the authors of this work were able to describe the dependence of bond energies of nonequivalent hybrid orbitals on their lengths and electronic configurations of interacting atoms in low-symmetry crystals of cadmium antimonide in one general expression:

$$D_{A-B}^{(j)} = \frac{c_1(R_{UA}^o + R_{UB}^o)}{(tg\alpha_A + tg\alpha_B) \left( \frac{1}{d_j} - \frac{c_2 d_j}{d_j^2 - R_{UA} R_{UB}} \right)}, \quad (10)$$

where  $R_{UA}^o$  and  $tg\alpha_{A(B)}$  are coefficients of equations (3) – (4) for  $A$  and  $B$  atoms, and  $R_{UA}$  and  $R_{UB}$  – effective radii of their ions in  $(A-B)$  bond of length  $d_j$  ( $1 \leq j \leq 5$ ).

Constants  $c_1$  and  $c_2$  are chosen from the following considerations:  $c_2$  is a coefficient depending on the type of crystalline structure and reflecting quantitative relation between coefficients  $tg\alpha_A$  and  $tg\alpha_B$  from equations (3) – (4) and the values  $(R_{UA} / R_{UB})$ . Therefore, when solving a self-consistent variation problem, as a first approximation,  $c_2$  is chosen equal to  $c_2 \approx 0.5$  and for different compositions it can lie within  $0 < c_2 < 1$ .  $c_1$  is a coefficient showing a relationship between the dimensional and energy characteristics of interatomic interaction, such as ionization potentials, screening effects, electronegativity with effective radii and interatomic distances. In case of using non-system units, when the energy is measured in electron-volts, and the distance in angstroms ( $\text{\AA}$ ), for all nonequivalent hybrid orbitals of  $CdSb$   $c_1$  takes on the value equal to  $c_1 = 0.046 \text{ eV}/(\text{\AA})^2$ .

Calculations performed according to (10) yielded numerical values of the bond energies of nonequivalent hybrid orbitals in  $CdSb$  crystals (which are also referred to as dissociation energies of nonequivalent hybrid orbitals). Results of calculation of effective radii of interatomic distances of electron density redistribution  $\Delta e$ , dissociation energy  $D_i$  are given in the table.

Table

*Effective charges, effective radii and dissociation energies  
of nonequivalent hybrid orbitals in CdSb crystals*

$\varphi_j$ $R_U, \Delta l, D_j$	$\varphi_1(Cd - Sb)$	$\varphi_2(Cd - Sb)$	$\varphi_3(Cd - Sb)$	$\varphi_4(Sb - Sb)$	$\varphi_5(Cd - Cd)$
$d_j^{exper} (\text{\AA})$	2.84	2.91	2.81	2.81	2.99
$d_j^{theor} (\text{\AA})$	2.8398	2.9102	2.8104	2.81	2.9894
$R_U^{Cd} (\text{\AA})$	1.4408	1.4813	1.4239	–	1.4947
$R_U^{Sb} (\text{\AA})$	1.399	1.4289	1.3865	1.405	–
$R_U^{Cd} / R_U^{Sb}$	1.02988	1.03667	1.02697	1	1
$\Delta q$ bond $\varphi_j$	0.21	0.086	0.263	0.185	0.05
$D_j$ (eV)	6.78	6.95	6.71	7.598	6.414

As follows from the above results, the numerical values of dissociation energy of chemical bonds of bond energies of nonequivalent hybrid orbitals agree with the results of calculation of fine structure of chemical bond in [8 – 11] performed by methods of microscopic theory and inverse problems solutions. It is also noteworthy that the values of atomic constants, ionization potentials and affinity to electron were taken from [12].

### Discussion of results

Analysis of the results obtained in the present study shows that calculations of parameters of electronic structure in low-symmetry crystals by the proposed method are different from those predicted by modern quantitative chemical bond theories. Dissociation energy of bond energies of nonequivalent hybrid orbitals in *CdSb* crystals depends on interatomic distances. With increasing interatomic distances, the interaction energy of atoms must decrease. At the same time, there is a change of electronic density on the bonds which can both amplify and weaken this effect.

What is meant here is not the refinement of quantitative estimates, but a qualitative change in the system of views on chemical bond nature which is related to rejection of one of commonly accepted concepts ( $Z_A = -Z_B$ ) and increased attention to directional character of chemical bond.

Generalization of obtained information on the parameters of electronic structure ( $Z_{eff}$ ,  $R_U$ ,  $\Delta q$ ) and its comparison to a set of physical and chemical properties (in our case to dissociation energy of bond energies of nonequivalent hybrid orbitals in *CdSb*) made it possible to identify the regularities that could be brought into a logically consistent and harmonious system only with quantum-mechanical approach.

Such a way of solving the problem holds out a hope that the imperfections of theoretical treatment of the issues raised in this paper will stimulate further study of the problems of quantitative description of interatomic interaction in low-symmetry crystals and superlattices on their basis.

## Conclusions

1. On the basis of quantum-mechanical approach a method of using nonequivalent hybrid orbitals has been developed for the calculation of interatomic interaction in *CdSb* crystals.
2. Calculations were made of charge redistribution  $\Delta q$  on the nonequivalent hybrid orbitals characterizing formation of a bond, which is accompanied by escape of electrons to other directions of interatomic interaction, i.e. the bond becomes donor ( $+\Delta q$ ) or acceptor ( $-\Delta q$ ).
3. With regard to quantum-mechanical interpretation of empirical data, a method has been developed and calculations have been performed of dissociation energy of nonequivalent chemical bonds in *CdSb* crystals.
4. The results obtained in this paper agree with the results of chemical bond calculation by microscopic theory methods and can be used in the development of technological conditions for synthesis of new *CdSb* based materials with predicted properties.

## References

1. D.P. Belotskii, O.N. Manik, On the Relationship between Thermoelectric Material Melts' Properties and the State Diagrams 1. Regularities of Cleavage Manifestation in the State Diagrams, *J. Thermoelectricity* 1, 21 – 47 (1996).
2. D.P. Belotskii, O.N. Manik, On the Relation of Structure of Melts to the Diagrams of State in Thermoelectric Material. 2. Phase Changes and Electronic Properties of Melts, *J. Thermoelectricity* 2, 23 – 57 (1996).
3. D.P. Belotskii, O.N. Manik, On the Relationship between Electronic Properties and Structure of Thermoelectric Material Melts and the Diagrams of State. 3. Short-Range Structure and the character of Chemical Bond, *J. Thermoelectricity* 3, 3 – 24 (2001).
4. L.D. Landau, *Quantum Mechanics. Nonrelativistic Theory* (Moscow: Nauka, 1974), 752 p.
5. E.V. Prikhodko, On the Relationship between Thermodynamic Characteristics of Ions and Parameters of their Electronic Structure, *Izvestiya. Ferrous Metallurgy* 2, 1 – 4 (1991).
6. E.V. Prikhodko, On the Relationship between Thermodynamic Properties of Compounds and Parameters of their Electronic Structure, *Izvestiya. Ferrous Metallurgy* 8, 1 – 5 (1991).
7. E.V. Prikhodko, A.A. Rudenko, On the Effect of Component Effective Charges on Thermodynamic Properties of Oxide Melts, *Izvestiya. Ferrous Metallurgy* 6, 4 – 7 (1991)
8. I.V. Gutsul, O.N. Manik, T.O. Manik, Mathematical Models of Elasticity Theory and Chemical Bond in Low-Symmetry Crystals of Cadmium and Zinc Antimonides, *J. Thermoelectricity* 2, 18 – 25 (2010).
9. O.M. Manik, I.V. Gutsul, T.O. Manik, A.I. Savchuk, V.R. Bilinsky-Slotylo, Structure-Energy Peculiarities of Se, Te, Sb and Fe Chemical Bond, *J. Thermoelectricity* 3, 29 – 34 (2011).
10. A.A. Ascheulov, O.N. Manik, and T.O. Manik, Volumetric Micro- and Nanostructures of Sensor Electronics Based on Low-Symmetry  $A^{II}B^V$  Crystals, 4-th International Scientific and Technical Conference "Sensor Electronics and Microsystem Technologies", Abstracts (Ukraine, Odessa, June 28 – July 2, 2010), P.144.
11. O.M. Manik, T.O. Manik, and V.R. Bilinsky-Slotylo, Electron Structure and Dissociation Energies of Nonequivalent Chemical Bonds in *CdSb* and *ZnSb* Crystals, *Proc. of International Scientific and Technical Conference "Physico-Technological Problems of Information Transfer, Processing and Storage in Infocommunication Systems"* (Ukraine, Chernivtsi, November 3-5, 2016), P. 264.
12. *Chemical Bonds Dissociation Energy. Ionization Potentials and Affinity to Electron. Handbook*. Ed. by V.N. Kondratyev (AN SSSR Publ, 1962).

Submitted 18.11.2016



**L.I. Anatyчук<sup>1,2</sup>, R.R. Kobylanskyi<sup>1,2</sup>, I.A. Konstantinovich<sup>1,2</sup>, V.V. Lys'ko<sup>1,2</sup>,  
O.V. Puhantseva<sup>1,2</sup>, Yu.Yu. Rozver<sup>1,2</sup>, V.A. Tiumentsev<sup>1,2</sup>**

<sup>1</sup>Institute of Thermoelectricity of the NAS and MES Ukraine,

1 Nauky str., Chernivtsi, 58029, Ukraine;

<sup>2</sup>Yu.Fedkovich Chernivtsi National University,

2 Kotsyubynsky str., Chernivtsi, 58012, Ukraine

## **CALIBRATION BENCH FOR THERMOELECTRIC CONVERTERS OF HEAT FLUX**

---

*The results of development of the calibration bench for thermoelectric converters of the heat flux as well as their metrological characteristics analysis are provided in this paper. The calibration methods for one and two converters at a time were developed. The thermoelectric converter of a new type with simultaneous temperature and the heat flux measurements on the human body surface was developed and manufactured.*

**Key words:** calibration bench, thermoelectric converter, heat flux, volt-watt sensitivity.

### **Introduction**

Thermoelectric converters are promising devices used to determine local heat release on the human body surface [1 – 4]. State-of-the-art thermoelectric converters of the heat flux manufactured on the basis of highly efficient semiconductor materials are characterized by high sensitivity, response rate, technological effectiveness, optimum weight and overall dimensions, high reliability and low cost [5 – 9]. Such converters are unpretentious in service and can perform round-the-clock monitoring of the human body heat release [10 – 16] as well as the heat losses in remote heating lines.

An issue referred to the calibration of thermoelectric converters of the heat flux used in the devices for measuring integrated heat fluxes of biological objects, losses through engineering structures, heat-insulating coatings and in the heating line sections is of current interest. Typically, the calibration of such converters is carried out by an absolute method using a compensation heater and differential metering thermocouples, which are the indicators of zero temperature difference [17, 18]. However, such calibration requires the improvement in the measurement accuracy, since such converters refer to measuring equipment. It is possible to improve the accuracy by using a high-sensitivity auxiliary thermoelectric converter of the heat flux [19 – 21].

Therefore, *the purpose of this work* is to develop the calibration bench for thermoelectric converters of the heat flux using advanced method and to analyse metrological characteristics of these converters.

### **HFC calibration bench design**

For metrological characteristics analysis and calibration of thermoelectric heat flux converters (HFC) in the temperature range of  $-30\text{ }^{\circ}\text{C} \div +130\text{ }^{\circ}\text{C}$ , the bench shown in Fig. 1 was designed.

The bench consists of a measuring unit 1, a control unit 2 and a meter 3 (a high precision digital multimeter).

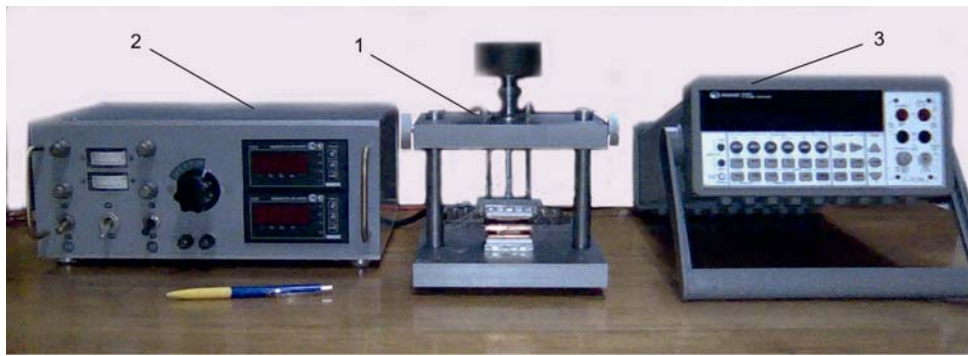


Fig. 1. Appearance of the bench for metrological characteristics analysis and HFC calibration.

The bench consists of a measuring unit 1, a control unit 2 and a meter 3 (a high precision digital multimeter).

In its turn, the measuring unit 1 incorporates an aluminium platform, on which liquid heat exchangers, a clamping device and a connecting bar are arranged. One or two HFC under study can be placed between hot and cold-side heat exchangers.

Schematically, the measuring unit 1 is shown in Fig. 2.

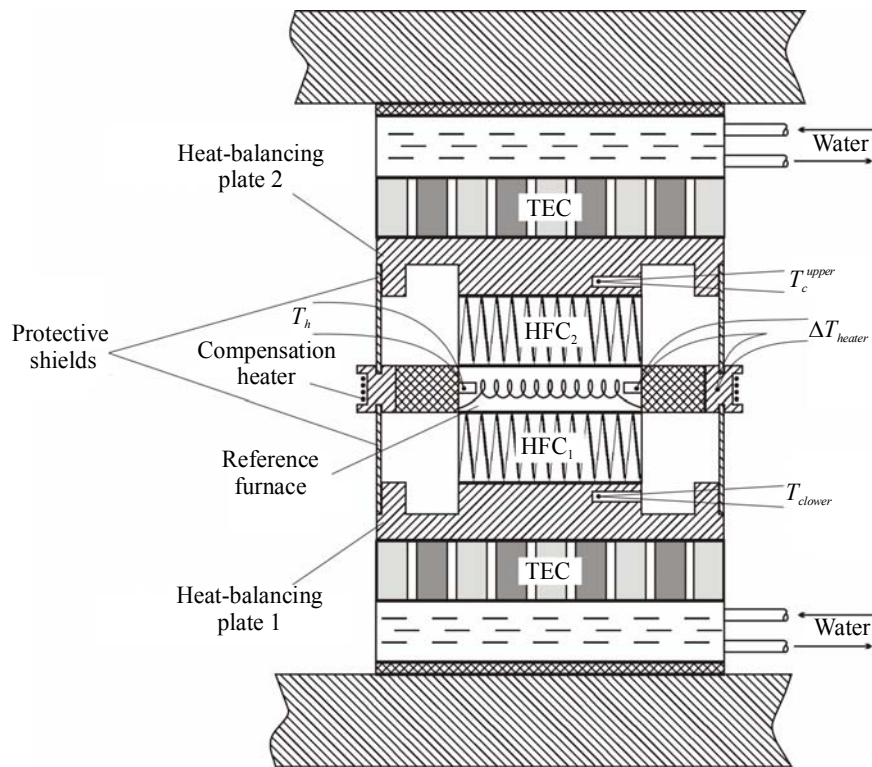


Fig. 2. Schematic diagram of the measuring unit for HFC calibration bench.

As shown in Fig. 1 and Fig. 2, two identical heat exchange units, which are designed to remove heat – cold-side heat exchangers, are mounted on a lower base of the aluminium platform and on a suspension of an upper base of the measuring unit 1. These heat exchangers are reverse ones, since they are manufactured on the basis of thermoelectric coolers (TEC) with liquid waste heat removal and can operate both in cooling and in heating modes depending on the direction of the electric current flow. Heat-balancing copper plates with built-in temperature sensors - platinum resistance thermometers, are fixed onto the TEC operating side. These plates in their central part are polished to achieve high-class purity flat surface - working platform. The HFC under study is placed on this

platform. The other HFC side contacts the hot-side heat exchanger – a flat heater which has two (upper and lower) polished operating surfaces. The thickness of the flat heater is made thin enough, so that its lateral surface is as small as possible and can be well heated throughout its volume. The temperature sensor - platinum resistance thermometer, is mounted in the casing of the heater. The use of platinum temperature sensors makes it possible to measure and maintain the temperature of the working platforms of heat exchangers using temperature controllers with an accuracy of  $\pm 0.1$  °C minimum in the temperature range of  $-30 \div + 130$  °C.

Since a lateral surface of the hot-side heat exchanger is not involved in the process of heat exchange with HFC and the heat losses are inevitable from it, a protective ring heater is mounted around its lateral surface to prevent such losses. The main task of the ring heater is to maintain the temperature to correspond to the temperature of the hot-side heat exchanger. This is achieved by using the differential thermocouple connected to a free channel of the temperature controller adjusted in such a way that the specific voltage supply to the heater of the protective ring furnace resulted in the zero signal of this thermocouple. Thus, the adiabatic isolation of the lateral surface of the hot-side heat exchanger is achieved.

The protective ring heater fulfils another important function. It transfers its temperature to a protective shield, which is positioned opposite to the lateral surface of the HFC under study. On the lower (and upper) surface of the protective ring heater, milled slots, which include “hot” end faces of the protective shields, are made. Other “cold” end faces of these shields are in thermal contact with the working platforms of the cold-side heat exchangers. Thus, the temperature gradient that corresponds to the temperature on the HFC lateral side is vertically formed on the surfaces of the protective shields. Due to this, the heat is not dissipated to the environment from the HFC lateral surface during its calibration.

Two cold-side heat exchangers are used in the bench for pair comparison calibration of two HFCs simultaneously. During calibration of a single HFC, a spare cold-side heat exchanger is used as another protective heater, in which the temperature of the hot-side heat exchanger is set using the temperature controller, and thus, adiabatic protection against heat losses from the spare surface of the heater of the hot-side heat exchanger is created. The control unit 2, which comprises regulated power supply units for TEC and heaters, two duplex microprocessor temperature controllers PE-202, connecting elements and test measuring terminals, monitors the process of temperature control in all heat exchangers.

All the outputs of electrical components from the measuring unit 1 converge in the connecting bar and are connected to the control unit 2 with a cable. The meter – a high precision digital multimeter M3500, is also connected to the control unit with the possibility of measurement results transmission to a PC in real time. Thus, the developed bench enables the calibration of thermoelectric HFCs and the analysis of their metrological characteristics under dynamic conditions.

### **The calibration methods for a single HFC**

The calibration of a single thermoelectric HFC using the developed bench (Fig. 1) is carried out according to the following procedure:

- Connect the measuring unit 1 to the control unit 2
- Connect the cable input of the measuring device 3 to the corresponding terminals of the control unit 2
- Connect the TEC liquid-cooled hoses to the water main, turn on and run the tap through the cooling system

- Lift and fix the top cold-side heat exchanger in upper position
- Place the HFC under study on the working platform of the lower cold-side heat exchanger
- Connect the outputs of the HFC under study to the corresponding terminals of the connecting bar
- Install the lower shield
- Install the hot-side heat exchanger with the protective ring heater on the HFC and the upper end face of the protective shield
- Install the upper protective shield
- Lower the upper cold-side heat exchanger, so that its heat-balancing plate is arranged on the upper protective shield. In this connection, the clamping force is set with the use of the additional load
- Set the temperature of the lower cold-side heat exchanger on the temperature controllers of the control unit 2
- Set up the instrument switch on the control unit 2 on the position “heater voltage”, switch on the meter 3 and switch it to the mode “DC voltage” with “Automatic” range and from the expression

$$W = U^2 / R, \quad (1)$$

(where  $R$  – is the heater resistance) determine the voltage and set it in the heater of the hot-side exchanger, which would correspond to the required electric power in the range of 10 mW - 1 W;

• Based on the reading “Hot-side heat exchanger temperature” at the respective channel of the temperature controller operating in the temperature measuring mode, when this temperature reaches the steady-state mode, set the same temperature value in the upper cold-side heat exchanger. In this case, the temperature of the ring heater is maintained automatically

- Set up the switch of the control unit 2 on the position “Thermoelectric HFC”
- When the set temperatures are reached in the fixed heat exchangers, determine the thermopower value of the thermoelectric HFC
- Set up the instrument switch on the position “Hot-side heat exchanger heater voltage” and “Hot-side heater exchanger heater current” in sequence and determine the precise values of the electrical signals

- Determine the heater capacity from the expression:

$$W = UI. \quad (2)$$

- Determine the volt-watt sensitivity of the thermoelectric HFC by the formula:

$$v = \frac{E}{W}. \quad (3)$$

### **Calibration methods for two HFCs at a time**

Pair calibration of two thermoelectric HFCs simultaneously is performed only when measuring similar samples. Such pair measurement of characteristics differs from the measurements of a single HFC only in the fact that the second HFC is mounted on top of the hot-side heat exchanger. The outputs of the second HFC are connected to the respective terminals of the connecting bar on the measuring unit 1 and the measurement of the HFC thermopower signal is carried out when the instrument switch of the control unit 2 is adequately positioned.

In this case, the same temperature is set in the upper cold-side heat exchanger on the temperature controller as in the lower cold-side heat exchanger.

The electric power released in the hot-side heat exchanger is divided in half, passes through two HFCs and dissipates at two cold-side heat exchangers. Since the temperatures of the hot sides of each HFC are common, and the cold-side temperatures are the same (maintained by the temperature

controller), the volt-watt sensitivities of each HFC can be calculated from the following expressions:

$$v_1 = \frac{2E_1}{W}, \quad (4)$$

$$v_2 = \frac{2E_2}{W}. \quad (5)$$

where  $E_1$  and  $E_2$  are the thermopower values for the first and second HFCs under study, respectively. The number “2” in the numerator comes from the denominator, since the half-value power is taken for each HFC, that is

$$W_1 = W_2 = \frac{W}{2}. \quad (6)$$

### HFC parameter measurement results

By optimizing the geometry of half-cells of HFC microthermopiles, experimental samples of primary converters of improved design with increased sensitivity and response rate with dimensions of  $22 \times 22 \times 4$  mm (Fig. 3) were produced. Metrological characteristics (volt-watt sensitivity, time constant, etc.) of such converters were studied on the developed bench designed for the HFC calibration based on the abovementioned methodology.

The appearances of such HFC experimental samples are shown in Fig. 3.

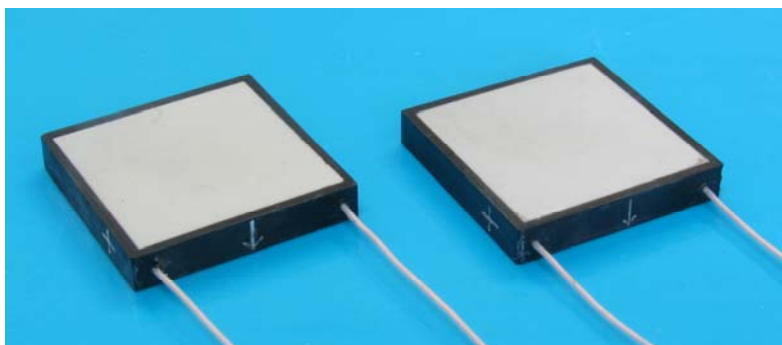


*Fig. 3. Appearances of HFC experimental samples with dimensions of  $22 \times 22 \times 4$  mm.*

Parameter measurement results for two HFC experimental samples with dimensions of  $22 \times 22 \times 4$  mm are shown in Table 1.

*Table 1*

*Parameter measurement results for HFC with dimensions of  $22 \times 22 \times 4$*

№	Parameter name	HFC	
		No.1	No.2
1.	Heat flux range, W/m <sup>2</sup>	$10^{-2} \div 10^3$	$10^{-2} \div 10^3$
2.	Sensitivity, V/W	1.48	1.51
3.	Time constant, sec	12	12
4.	Operating temperature range, °C	$-30 \div +130$	$-30 \div +130$
5.	Thermopile overall dimensions, mm	$22 \times 22 \times 4$	$22 \times 22 \times 4$

Besides, a new design type of thermoelectric converters that combine simultaneous measurements of temperature and the heat flux on the human body surface was developed. The appearance of HFC experimental samples with dimensions of  $16 \times 16 \times 3$  mm is shown in Fig. 4.

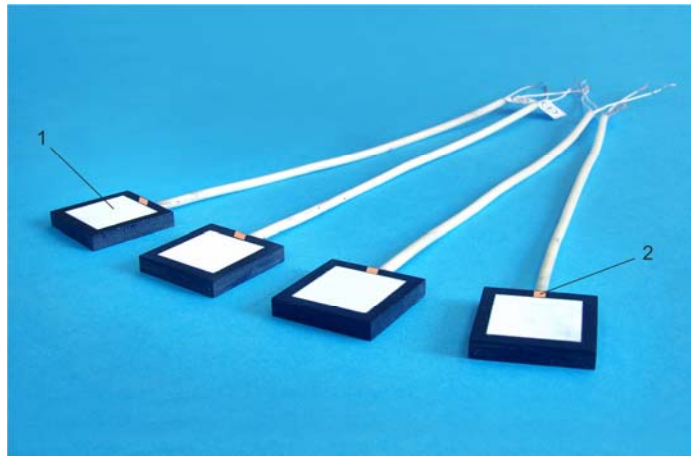


Fig. 4. Appearance of HFC experimental samples with dimensions of  $16 \times 16 \times 3$  mm:  
 1 – thermoelectric heat flux sensor, 2 – temperature sensor.

The results of determination of the main parameters of four HFC experimental samples with dimensions of  $16 \times 16 \times 3$  mm are given in Table 2.

Table 2

*Parameter measurement results for HFC with dimensions of  $16 \times 16 \times 3$  mm*

№	Parameter name	HFC			
		№ 1	№ 2	№ 3	№ 4
1.	The heat flux range, W/m <sup>2</sup>	$10^{-2} \div 10^3$	$10^{-2} \div 10^3$	$10^{-2} \div 10^3$	$10^{-2} \div 10^3$
2.	Sensitivity, V/W	3.2	3.32	3.1	3.25
3.	Time constant, sec	10	11	11	10
4.	Thermopile overall dimensions, mm	$16 \times 16 \times 3$	$16 \times 16 \times 3$	$16 \times 16 \times 3$	$16 \times 16 \times 3$

Time characteristics of these thermoelectric HFC are shown in Fig. 5.

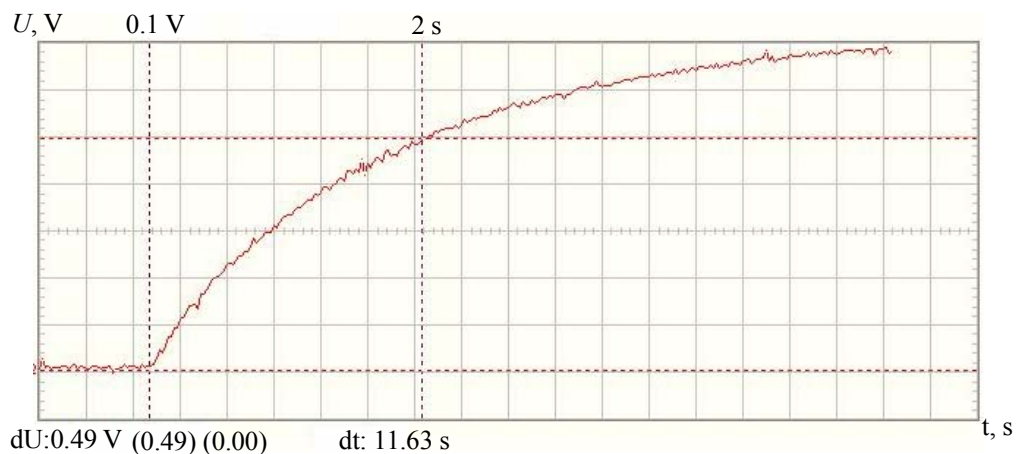


Fig. 5. Time characteristics of HFC with dimensions of  $16 \times 16 \times 3$  mm  
 with ceramic receiving surface.

As can be seen from the above, the bench designed for the thermoelectric HFC calibration makes it possible to study the characteristics of the converters and transmit the measurement results to a PC in real time. The thermoelectric HFCs of a new type with simultaneous measurements of temperature and the heat flux enable monitoring of the temperature and heat condition of a human in real time.

## **Conclusions**

1. The calibration bench for thermoelectric converters of the heat flux, which makes it possible to study the metrological characteristics of the converters and transmit the measurement results to a PC in real time was developed and manufactured. The calibration methods for one and two thermoelectric converters at a time were developed.
2. The thermoelectric converters of a new type with simultaneous measurements of the temperature and heat flux, ensuring monitoring of the temperature and heat condition of a human in real time, were developed.
3. An advanced calibration method for thermoelectric sensors using an auxiliary high-sensitivity thermoelectric converter of the heat flux, which allows improving the accuracy of experimental determination of the volt-watt sensitivity of such sensors, was implemented.

## **References**

1. L.I. Anatyshuk, *Thermoelements and Thermoelectric Devices: Reference Book* (Kyiv:Naukova Dumka, 1979), 766 p.
2. O.A. Geraschenko, *Foundations of The heat flux Measurement* (Kyiv: Naukova Dumka, 1971), p.192.
3. L.I. Anatyshuk, O.Ya. Luste, *On Boundary Possibilities of Microcalorimeters* (Engineering and Physics Journal, 1978, V.35, №4), pp. 638 – 647.
4. L.I. Anatyshuk, O.Ya. Luste, *Microcalorimetry* (Lviv: Vyscha shkola. Lviv Univ. Pub., 1981), 160 p.
5. L.I. Anatyshuk, N.G. Lozinsky, P.D. Mykytyuk and Yu.Yu. Rozver, *Thermoelectric Semiconductor Heat Meter, Instruments and Experimental Techniques* **5**, 236 (1983).
6. L.I. Anatyshuk, L.P. Bulat, D.D. Gutsal and A.P. Myagkota, *Thermoelectric Heat Meter, Instruments and Experimental Techniques* **4**, 248 (1989).
7. O.A. Geraschenko, T.G. Grischenko, L.V. Dekusha, *Methods of Designing Optimal The heat flux Converters* (Problems of energy saving, 1990, Issue 3), pp. 36 – 42.
8. L.I. Anatyshuk, B.M. Demchuk, O.Ya. Luste, *The Theory of Designing Vortex Microcalorimeters*, *J.Thermoelectricity*, 2002, №3, pp. 18 – 27.
9. B.M. Demchuk, O.Ya. Luste, *Information And Energy Description of Thermoelectric Multiple Thermopiles*, *J.Thermoelectricity*, 2003, №2, pp. 54 – 56.
10. R.B. Ladyka, D.N. Moskal, V.D. Didukh, *Semiconductor Heat Meters in Arthropathy Diagnostics and Treatment*, *Meditinskaya Tekhnika* **6**, 34 – 35 (1992).
11. R.B. Ladyka, O.N. Dakaliuk, L.P. Bulat, A.P. Miagkota, *Application of Semiconductor Heat Meters in Diagnostics and Treatment*, *Meditinskaya Tekhnika* **6**, 36 – 37 (1992).
12. B.M. Demchuk, L.Ya. Kushneryk, and I.M. Rublenyk, *Thermoelectric Sensors for Orthopedics*, *J.Thermoelectricity* **4**, 80 – 85 (2002).
13. A.A. Asheulov, L.Ya. Kushneryk, *Thermoelectric Device for Medico-Biological Express-*

- Diagnostics, *Tekhnologiya i Konstruirovaniye v Elektronnoi Apparature* **4**, 38 – 39 (2004).
14. V.S. Gischuk, R.R. Kobylanskyi, and R.G. Cherkez, Multi-Channel Device for Temperature and The heat flux Density Measurement, *Scientific Bulletin of Chernivtsi University: Collected Scientific Works. Physics. Electronics*, **3**, issue 1 (Chernivtsi: Chernivtsi National University, 2014), p. 96 – 100.
  15. R.R. Kobylanskyi, V.V. Boichuk, The Use of Thermoelectric Heat Meters in Medical Diagnostics, *Scientific Bulletin of Chernivtsi University: Collected Scientific Works. Physics. Electronics*, **4**, issue 1 (Chernivtsi: Chernivtsi National University, 2015), p. 90 – 96.
  16. L.I. Anatyshuk, O.I. Ivaschuk, R.R. Kobylanskyi, I.D. Postevka, V.Yu. Bodiaka, I.Ya. Gushul, Thermoelectric Device for Temperature and The heat flux Density Measurement "ALTEC-10008", *J. Thermoelectricity* **1**, 76 – 84(2016).
  17. T.O. Lukhtan, D.P. Kolomiets, S.I. Kovtun, L.Y. Vorobyov, Metrological Certification Thermoelectric Converters of Heat Flux, *Ukrainian Food Journal*, V.1, №3, 60 – 63(2012).
  18. L.I. Anatyshuk, R.R. Kobylanskyi, and I.A. Konstantinovich, Calibration of Thermoelectric The heat flux Sensors, *Proc. of XV International Research and Practical Conference "Current Information and Electronic Technologies"*, Vol.2 (Odessa, Ukraine, May 26-30, 2014), p. 30 – 31.
  19. GOST 25380-82. Method of measuring density of heat flows passing through enclosure structures. – 1983.
  20. GOST 7076-99. Building materials and products. Method of determination of steady-state thermal conductivity and thermal resistance. – 2000.
  21. GOST 3756-98. Thermoelectric heat flow converters for general use. – 2000.

Submitted 26.10.2016



---

**U.I. Abdulkhakimov, D.V. Yevdulov, O.V. Yevdulov, N.A. Nabiev**

Federal State Budget Educational Institution of Higher Professional Education  
“Dagestan State Technical University”, 70, Ave. Imam Shamil, 367015,  
Makhachkala, Russia

---

## **MODEL OF THERMOELECTRIC DEVICE FOR CARRYING OUT THERMAL COSMETOLOGY PROCEDURES**

---

*A model of thermoelectric system for carrying out thermal cosmetology procedures is considered which is based on solving a two-dimensional nonstationary problem for a system of complex configuration. Temporal variations of temperature at different points of target object – skin area exposed to thermal cosmetology procedures, were obtained as a function of cooling capacity and heating efficiency of thermoelectric modules.*

**Key words:** thermoelectric system, thermal exposure, cosmetology, biological object, temperature field, model.

### **Introduction**

At the present time, in the practice of carrying out cosmetology procedures the methods based on thermal exposure (thermal and cryotherapy) are increasingly used [1, 2]. Such fairly active use of this type of methods is due to the fact that thermal exposure has a great influence on the energy balance in the body. Under the influence of heat, the blood and lymph vessels expand, which improves blood circulation in many internal organs. This leads to activation of metabolism and qualitative saturation of the body with nutrients and oxygen. Heating stimulates fat oxidation, purifies organism, removing harmful toxins and other products of vital activity through sweat, thereby contributing to the improvement of skin condition. Cooling has a strong anti-aging effect, smooths wrinkles, eliminates the spread of acne, cellulite deposits, smooths scars, removes skin formations, papillomas and benign tumors. Cooling masks remove puffiness of the face, model its shape, smooth wrinkles and improve color. Thermal massage is used to strengthen the scalp and hair roots and effectively treats seborrhea.

The application of heat to the body as a whole or its parts is constantly improved, differentiated and at present represents a number of approved methods, each of which has its own indications [3]. Today, the use of thermal exposure in cosmetology practice follows two main directions. First, cooling or heating the entire organism or its comparatively large parts. Second, thermal effect only on certain tissue areas, including pathologically changed.

While in the former case powerful cooling and thermal machines (e.g., vapour compression, absorption, etc.) are used for cooling (heating) the entire organism, systems with lower heating efficiency and cooling capacity based on other principles of energy conversion can be used for exposure to heat of individual zones of human body.

Under these conditions, the use of thermoelectric systems (TES) [4], which are characterized by high reliability, ecological compatibility, noiselessness, functionality and a significant service life, as well as the possibility of a simple transition from cooling to heating mode and vice versa, has a good outlook for local thermal exposure for the purpose of cosmetology procedures.

*The purpose of the work* is development of a theoretical model to study various operating modes of TES for carrying out thermal cosmetology procedures, taking into account complex configuration of the system, as well as the possibility of a simultaneous contrast thermal effect on biological object in arbitrary zones.

### **Design of TES for carrying out thermal cosmetology procedures**

The appearance of operating part of TES (control unit bases) is shown in Fig. 1 [5]. It comprises a base made in the form of a mask repeating the contours of human face with the holes for eyes, nose and mouth. In the frontal and cheek areas on the inside of the base there are thermal exposure zones the function elements of which are thermoelectric modules (TEM) contacting with heat-leveling plates for creation of a uniform heat flux. The TEM are connected to programmable direct current source implementing various operating conditions of modules (cooling, heating, their alternation) depending on the type of cosmetology procedure. The dose and duration of thermal exposure is determined by the doctor-cosmetologist, who is also in charge of current monitoring of the patient's condition.



*Fig. 1. Appearance of operating part of the system for carrying out cosmetology procedures.*

### **Model of TES for carrying out thermal cosmetology procedures**

The model is based on solving two problems: determination of the required values of heat flux from TEM, the function element of TES, and calculation of the basic characteristics of the latter.

The first problem is solved on the basis of analysis of the temperature field of arbitrary-shaped plate which is a target object, with discrete energy sources corresponding to TEM in the system [6].

With regard to presentation of heat sources and sinks (TEM) as a step function, mathematical formulation of the problem of calculation of the temperature field of target object was obtained as follows:

$$\lambda \frac{\partial^2 T}{\partial x^2} + \lambda \frac{\partial^2 T}{\partial y^2} + q_{TEM}(x, y) + q_{amb} = c\rho \frac{\partial T}{\partial \tau}, \quad (1)$$

$$q_{TEM}(x, y) = \sum_{j=1}^J q_{TEM_j}(x, y); \quad (2)$$

$$q_{TEM_j}(x, y) = \begin{cases} \frac{Q_{TEM_j}}{S_{TEM_j}} & \text{in the area of energy source} \\ 0 & \text{outside the area of energy source} \end{cases}, \quad (3)$$

$$S_{TEM_j} = \iint_{S_{TEM_j}} S_{TEM_j}(x, y) dx dy, \quad (4)$$

$$q_{cp} = \alpha(T - T_{amb}), \quad (5)$$

$$\lambda \frac{\partial T}{\partial n} = \alpha(T - T_{amb}) \text{ at } x, y \in L, \quad (6)$$

$$T = 309.6 \text{ K at } \tau = 0. \quad (7)$$

where  $T$  is temperature at any point of target object;  $T_{amb}$  is ambient temperature;  $\tau$  is time;  $\delta$  is plate thickness;  $\lambda$  is effective thermal conductivity coefficient of target object;  $\alpha$  is coefficient of heat transfer to the environment ( $\alpha = \text{const}$ );  $c$  is heat capacity of target object,  $\rho$  is density of target object,  $q_{TEM}(x, y)$  is total surface density of heat flux from the local heat sources and sinks,  $q_{TEM_j}(x, y)$  is surface density of heat flux from  $j$ -th local heat source (TEM);  $Q_{TEM_j}$  is power dissipated by  $j$ -th local source of heat;  $q_{amb}$  is surface density of heat flux to target object from the environment;  $L$  is curve restricting the area of biological object exposed to thermal effect,  $n$  is normal to curve  $n = (xh + yg)$ ;  $h, g$  are unit vectors.

Solving of equations by finite element numerical method (1)–(7) allowed temperature determination at different points of target object – skin area exposed to thermal cosmetology procedures, as well as tracing its variation depending on the value of heat flux from TES (cooling capacity and heating efficiency of TEM), ambient conditions.

Calculation was performed in conformity with the necessary conditions of carrying out cosmetology procedures: target object temperature –  $283 \div 313$  K, exposure duration –  $3 \div 12$  min., possibility of alternation of heating and cooling modes. In the system model it was supposed to use 6 standard TEM, 2 of which are arranged in the frontal part, and 2 in each cheek zone. TEM dimensions: length - 40 mm, width - 40 mm. The input data were as follows:  $\lambda = 0.6$  W/(m·K),  $C = 3458$  J/(kg·K),  $\rho = 1041$  kg/m<sup>3</sup>,  $T_{amb} = 295$  K,  $\alpha = 5$  W/(m<sup>2</sup>·K).

Temporal variations of biological object temperature on exposure to uniform and contrast thermal effect were obtained. The results of calculations are given in Figs. 2 – 3.

Fig. 2 represents temporal variations of base surface temperature brought into contact with human face on exposure to cooling and heating for the values of  $q_{TEM_j}(x, y)$ , equal to 7000 W/m<sup>2</sup>; 9000 W/m<sup>2</sup>; 11000 W/m<sup>2</sup>; 13000 W/m<sup>2</sup>, respectively.

As follows from the above dependences, the duration of onset of steady-state regime is 5 minutes for device operation in cooling mode and 4 minutes for device operation in heating mode. In so doing, the increase in surface density of heat flux from TEM leads to decreasing temperature of biological object for TES operation in cooling mode and to increasing its temperature for TES operation in heating mode, respectively, which corresponds to increase in cooling capacity and heating

efficiency of modules. Thus, the increase in  $q_{TEMj}(x, y)$  from  $7000 \text{ W/m}^2$  to  $13000 \text{ W/m}^2$  on cooling biological object reduces its temperature from  $287.5 \text{ K}$  to  $283 \text{ K}$ , and the increase in  $q_{TEMj}(x, y)$  by the same value on heating increases the temperature of target object from  $317.7 \text{ K}$  to  $320 \text{ K}$ .

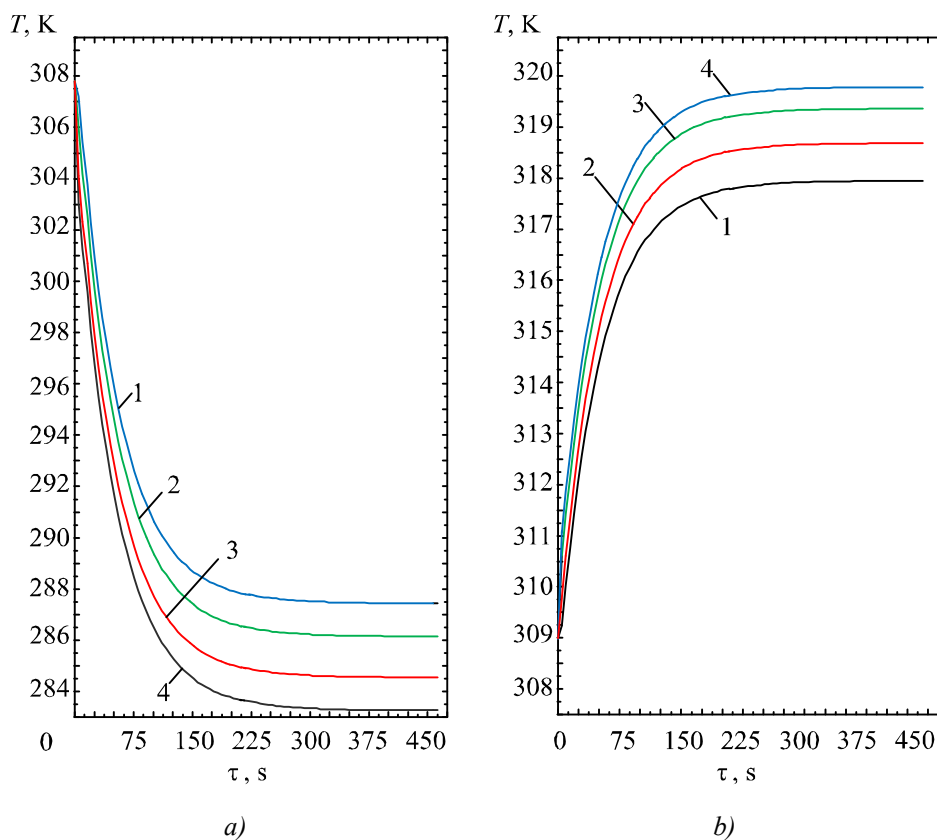


*Fig. 2. Temporal variation of biological simulator temperature on exposure to cooling (a), to heating (b) for different values of  $q_{TEMj}(x, y)$ : 1 –  $q_{TEMj} = 7000 \text{ W/m}^2$ ; 2 –  $q_{TEMj} = 9000 \text{ W/m}^2$ ; 3 –  $q_{TEMj} = 11000 \text{ W/m}^2$ ; 4 –  $q_{TEMj} = 13000 \text{ W/m}^2$ .*

Here it should be noted that it seems expedient to bring TES to operating mode prior to carrying out cosmetology procedures with a view to increase their comfort. The above can be implemented by preliminary cooling (heating) of the base, and then, on achievement of required temperatures, its application on the face of a person.

With the use of the proposed TES design, a dynamic thermal operating mode of the device can be implemented, which is characterized by alternation of cooling and heating modes in conformity with the specified program.

To study the possibilities of TES with implementation of this operating mode, the dependences of temporal change of biological simulator temperature with alternation of device operating conditions were obtained, which are shown in Fig. 3. The results are represented for  $q_{TEMj}(x, y)$  equal to  $6000 \text{ W/m}^2$ ;  $5000 \text{ W/m}^2$ ;  $4000 \text{ W/m}^2$ . In both cases, the duration of transition from cooling to heating mode and vice versa is of the order of 5 minutes, which calls for further optimization in terms of reducing the duration of this transition from one mode to the other.

This optimization seems possible by selecting the appropriate type of TEM characterized by high-speed performance; transition when switching TES from cooling to heating from the mode of maximum coefficient of performance (heating coefficient) to the mode of maximum cooling capacity (heating efficiency); reduction of total heat capacity of design by selecting the appropriate base material; reduction of total thermal inertia of design due to elimination of certain zones of human face

from the cosmetology procedure and, accordingly, the base area (exposure of only certain areas of human face, as needed), arrangement of TEM directly in the affected area, instead of using the entire base for cooling (heating).

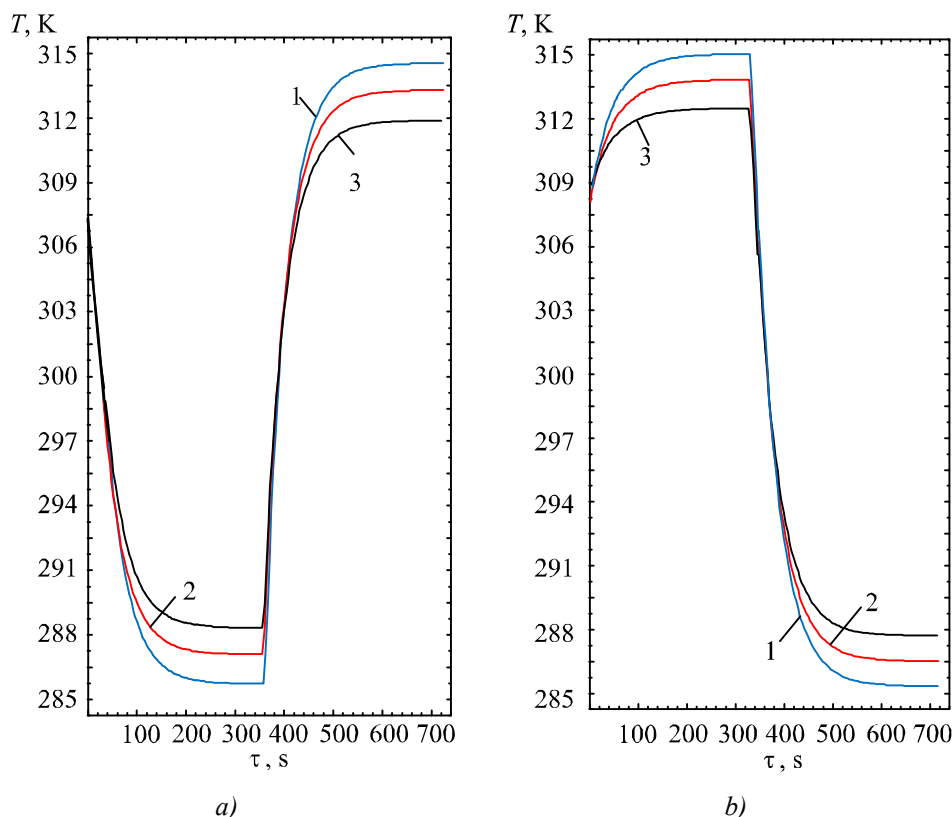


*Fig. 3. Temporal variation of biological object temperature on exposure to contrast dynamic thermal effect at transition of TES from cooling to heating mode (a), from heating to cooling mode (b) for different values of  $q_{TEMj}$ .  
 1 –  $q_{TEMj} = 6000 \text{ W/m}^2$ ; 2 –  $q_{TEMj} = 5000 \text{ W/m}^2$ ; 3 –  $q_{TEMj} = 4000 \text{ W/m}^2$ .*

It should be noted that the existing analogs which implement this kind of thermal cosmetology procedures, for instance, cosmetology instruments Vivax CryoPro (company "Vivax", France) [7], OHOTA-5M ("OHOTA" Ltd., Moscow) [8], Flash 1 Jumbo (company "General Project", Italy) [9] and others, described in sufficient detail in [4], possess higher-speed performance (change of mode can be implemented within tens of seconds). However, the distinguishing feature of these systems is the use of a small-size probe as a function element, which is mechanically moved over person's face during the procedures. In so doing, the high speed of alternation of thermal exposure modes refers only to the zone of action of this probe at given instant. If, however, we consider the cosmetology procedure with respect to the entire patient's face, or its larger part, implementation of contrast thermal exposure will be much longer. Thus, the lack of the possibility of simultaneous coverage of large exposure areas will cancel out the advantage of high-speed performance of analogs, reduce the efficiency of procedures, and improve their duration when covering the entire face.

Based on the analysis of the obtained heat flux values formed by TES, equivalent to cooling capacity and heating efficiency of TEM, calculation of characteristics of the latter can be performed which is the second problem solved in the construction of system model. The sought-for values in this case are geometric dimensions of thermoelements that make up the module, the value of supply current, and electric power consumption. A detailed description of the method for calculating these

TEM characteristics is given in [10]. In so doing, in the majority of cases TES can employ TEM of standard type that can be selected using special software packages. For TES version under study, for instance, use can be made of standard TEM of TB-127-1.0-1.5 type, produced by Kryotherm company (Saint-Petersburg), fully implementing the required modes of carrying out therapeutic procedures. For their selection, “Thermoelectric system calculation” software package can be used [11]. This software yields the dependences of change in such TEM parameters as cooling capacity, coefficient of performance on its current characteristics.

## **Conclusions**

1. To date, in cosmetology practice, methods of exposure based on the use of a thermal factor (cooling and heating of a biological object) are becoming increasingly widespread.
2. Among the existing methods of thermal cosmetology procedures, the use of technical means based on thermoelectric energy converters is efficient.
3. A thermoelectric system (TES) for thermal cosmetology effect on human face was developed, where the function elements are TEM enabling to combine cooling and heating modes in a single device.
4. A model of TES was developed for carrying out thermal cosmetology procedures which is based on solving a two-dimensional nonstationary thermal conductivity problem for a complex system.
5. Temporal variations of temperature at different points of target object – skin area exposed to thermal cosmetology procedures as a function of cooling capacity and heating efficiency of TEM were obtained.
6. It was established that the onset of regime for TES is of the order of 4 – 5 minutes, so it seems advisable to reach the operating mode of TES prior to carrying out cosmetology procedures by their preliminary cooling or heating.
7. In the framework of the experiment it was established that the duration of TES switching from cooling to heating mode and vice versa is 5 minutes, which requires further design optimization due to the use of more advanced types of TEM, variation of TEM operating conditions, as well as reduction of total heat capacity of device design.

## **References**

1. V.V.Yezhov, Physical Therapy and Physioprofilaxis as the Methods for Keeping Healthy and Rehabilitation, *Physical Therapy, Balneology and Rehabilitation* 4, 33-36 (2011) (in Russian).
2. V.M.Bogolyubov, V.S.Ulashchik, Combination and Conjunction of Therapeutic Physical Factors, *Physical Therapy, Balneology and Rehabilitation* 5, 39-45 (2004) (in Russian).
3. S.M.Zubkova, Role of Thermal Component in the Therapeutic Effect of Physical Factors, *Physical Therapy, Balneology and Rehabilitation* 6, 3– 10 (2011) (in Russian).
4. L.I.Anatyshuk, O.I.Denisenko, R.R.Kobylianskyi, and T.Ya.Kadenyuk, On the Use of Thermoelectric Cooling in Dermatology and Cosmetology, *J.Thermoelectricity* 3, 57-71 (2015).
5. *Patent of Russian Federation for invention № 2562509 Thermoelectric Device for Cosmetological Procedures on Human Face / T.A.Ismailov, O.V.Yevdulov, M.A.Khazamova, D.V.Yevdulov, U.I.Abdulkhakimov, and B.I.Akhmedov, publ. 10.09.2015, Bul. №25.*
6. T.A.Ismailov, O.V.Yevdulov, M.A.Khazamova, and R.A.-M.Magomadov, Mathematical Model of Thermoelectric System for Local Thermal Effect on Human Hand, *J.Thermoelectricity* 1, 77-86 (2014).

7. <http://ankportal.ru/catalog/vivax-cryo-pro>.
8. <http://www.tepmoxota.ru/agregat.htm>.
9. <http://medbuy.ru/apparat-dlya-elektroepilyacii/general-projektflash-1-jumbo>.
10. L.I. Anatyshuk, *Thermoelements and Thermoelectric Devices* (Kyiv: Naukova Dumka, 1979), 768 p.
11. <http://www.kryotherm.ru>.

Submitted 21.11.2016



*M.V. Maksimuk*

**M.V. Maksimuk, I.S. Andrusiak**

Institute of Thermoelectricity of the NAS  
and MES of Ukraine, 1, Nauky Str., Chernivtsi,  
58029, Ukraine



*I.S. Andrusiak*

**ELECTRONIC CONTROL UNIT FOR  
THERMOELECTRIC AUTOMOBILE  
STARTING PRE-HEATER**

---

*Design and operation algorithm of electronic control unit for thermoelectric automobile starting pre-heater is presented. The main functional units of the device are described. The results of experimental research on the work of electronic unit with the heater components are given.*

**Key words:** processor module, analog-to-digital converter, thermoelectric converter, flame indicator.

**Introduction**

Modern means for preheating of vehicle engines under low ambient temperatures must meet a number of requirements. Thus, alongside with high heat productivity, low fuel consumption and reasonable dimensions, starting pre-heaters must start reliably and operate without failure. That is why apart from creation of new heat-efficient designs, producers of starting equipment place great emphasis on development of electronic control units, namely systems of automatic control of heater components, i.e. fuel and circulation pumps, air supply fan, burner filament pin.

The basic functions of such electronic unit are as follows [1]:

- temperature control of engine cooling liquid and depending on its value establishment of corresponding heating conditions;
- diagnostics of components when starting the heater and during its operation;
- the heater switch on and off on command from control panel;
- the heater switch off in case of emergency (failure of components, heat carrier overheat, absence of flame, voltage difference, short circuit, etc.).

For the autonomous thermoelectric starting pre-heater developed in the Institute of Thermoelectricity [2 – 8] the task of creation of electronic unit is significantly complicated, since alongside with traditional components, the heater design employs a thermoelectric converter which is used for electric energy supply to components themselves, as well as to automobile battery. So, apart from the above functions the electronic unit must provide constant and simultaneous temperature control of the hot and cold sides of thermal converter. Otherwise, thermopile overheat will not only cause quick failure of all heater components, but will also cause malfunction of other automobile equipment. It is important to choose rational operation algorithm of the heater that would not only assure maximum efficiency of thermoelectric conversion, but also would create conditions for a reliable start-up and stable operation of the device.

*The purpose of this work* is to create electronic control unit for thermoelectric automobile starting pre-heater and examine it for compliance with the above functional requirements.



### Design and operating principle

Block-diagram of electronic control unit for thermoelectric automobile starting pre-heater is shown in Fig. 1.

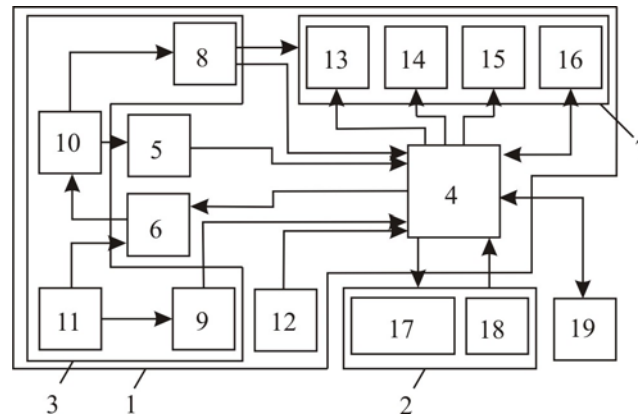


*Fig. 1. Block-diagram of electronic control unit [8]: 1 – monitor control unit; 2 – regulating and indicating unit; 3 – signal processing unit; 4 – processor module; 5 – voltage converter; 6 – battery charge control unit; 7 – external actuator control unit; 8 – input circuit of battery voltage meter; 9 – input circuit of thermopile voltage meter; 10, 11 – terminals; 12 – digital thermal sensor unit; 13 – power switching unit of filament pin; 14 – power switching unit of fuel pump; 15 – power switching unit of circulation pump; 16 – fan power supply and speed control; 17 – optical indication unit; 18 – temperature control unit; 19 – software communication unit.*

Electronic control unit consists of two building blocks: 1 – monitor control unit of thermoelectric starting pre-heater and 2 – regulating and indicating unit.

Monitor control unit comprises signal processing unit 3, processor module 4 powered from voltage converter 5, battery charge control unit 6 and external actuator control unit 7.

Sensor signal processing units consist of input circuits 8 and 9 of battery and thermopile voltage meter which are connected through terminals 10 and 11 to processor module, digital thermal sensor unit 12 and analog-to-digital converter (ADC) of processor module (not shown in the figure).

External actuator control unit comprises power switching units 13, 14, 15 of filament pin, fuel pump and liquid pump, respectively, as well as unit 16 for power supply and speed control of a fan for air supply to combustion chamber.

Regulating and indicating unit (control panel) consists of optical indication unit 17 and cold heat carrier temperature control unit 18 (Fig. 2).

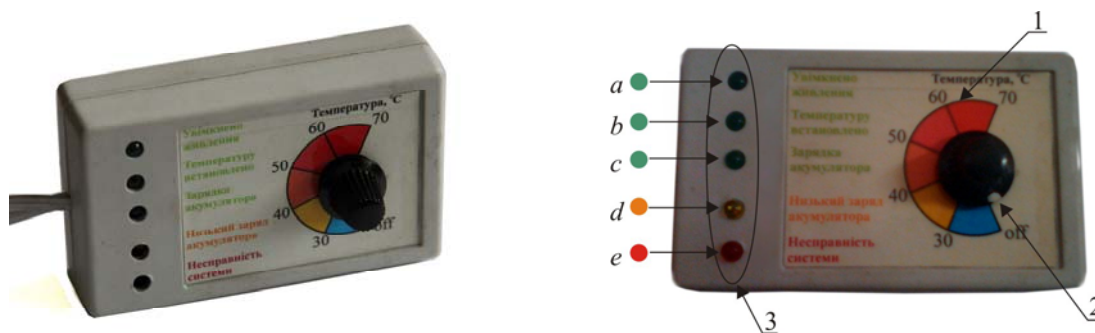


*Fig. 2. Control panel of thermoelectric starting pre-heater: 1 – cold heat carrier temperature scale; 2 – cold heat carrier temperature control; 3 – optical indication scale. a – “Components power supply on” indicator; b – “Heat carrier temperature set” indicator; c – “Battery charging” indicator; d – “Low batter charge” indicator; e – “System malfunction” indicator.*

It should be noted that in case of malfunctions in the work of the heater “System malfunction” indicator informs of error type by corresponding number of flashes.

For heater testing and keeping track of its components operation the electronic unit can be connected to specialized software (Fig. 3) by means of communication unit 19 and additional converter of data interface (is not part of the system).

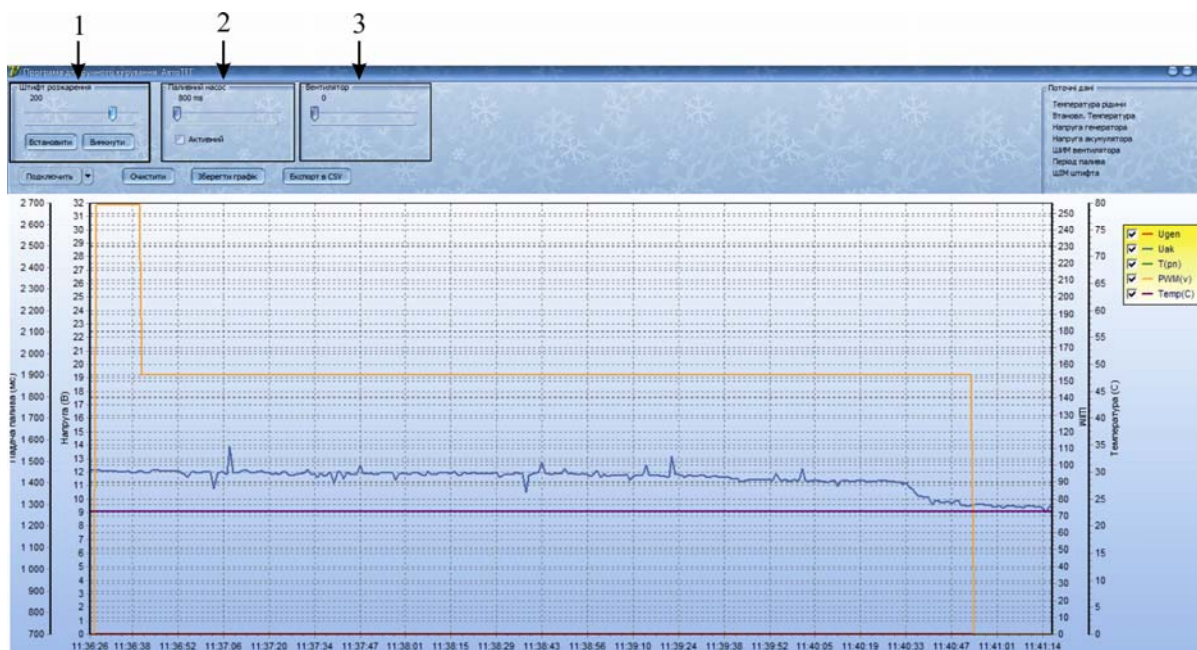


*Fig. 3. Program window for heater testing and keeping track of its components operation:*  
 1 – filament pin power manual control window; 2 – fuel pump pulse period manual control window;  
 3 – fan rpm manual control window;  $U_{gen}$  – electric voltage output of thermoelectric heater;  
 $U_{bat}$  – electric voltage of automobile battery;  $T(pn)$  – fuel pump pulse period;  
 PWM (v) – fan speed; Temp(C) – cold heat carrier temperature.

Connection to personal computer enables monitoring of the state of control signals from control units of peripheral devices, reflection of signals from sensors for measuring voltage, fan speed and voltage values on battery and generator terminals, as well as a list of device operation algorithm events is accessible.

The system also involves possibility of switching to manual control. In this mode, control signal of filament pin power, fan power, fuel supply period and heat carrier pump on and off can be assigned manually.

Control unit works as follows.

When the battery is connected to terminals 10, there is shutdown of all peripheral actuators and examination of the set temperature on control 7. At the set temperature below 30 °C (“off” zone) the device goes to standby mode. At the set temperature above 30 °C switching of the device and initialization of the burner take place by the following algorithm.

Units 15 and 16 switch on the pump and the fan using control signal from central processor 1.

In 10 seconds an inspection of fan speed takes place. If there are no pulses from fan speed control sensor 16, an emergency shutdown of the heater occurs, i.e. all peripheral devices are switched off and a corresponding error signal is displayed on optical indicator unit 7. If the pulses arrive, the initialization algorithm continues, i.e. fan power is reduced and filament pin is smoothly switched on by power switching unit of filament pin 13 by means of control signal from central processor unit 1.

In 40 seconds with the help of power switching unit of fuel pump 14 and control signal from central processor unit 1 the supply of fuel by fuel pump begins. In the process, the voltage is checked on the terminals of thermoelectric generator 11. Through the input circuit of thermoelectric generator voltage meter 9 the signal comes to the input of ADC unit of central processor 1. If in 5 minutes there is no voltage increase on the generator terminals, the heater switches off accidentally. If in 40 seconds there is voltage increase, the burner is lit, filament pin is switched off and the period of fuel supply is gradually reduced from 2.5 to 1 s.

Following that, the system exits initialization mode and enters stabilization mode.

In stabilization mode, constant monitoring of heat carrier temperature is realized by means of digital thermal sensor unit 12.

If heat carrier temperature is less than the set temperature, the period of fuel supply is smoothly reduced to 1 s. If this temperature corresponds to the set value, current period of fuel supply is maintained and a signal of temperature stabilization is displayed on optical indicator unit 6. If heat carrier temperature is higher than the set temperature, the period of fuel supply is gradually increased to 2.5 s.

During operation of the device there is constant voltage control on battery terminals 10 through input circuit of battery voltage meter 8. In conformity with the voltage on battery terminals and period of fuel supply the necessary fan power is set by battery power switching unit 6 and control signal from central processor unit 1. In so doing, battery charge control is done by means of battery charge switching unit 6 and control signal from central processor unit 1.

Moreover, the system exerts constant control over the presence of flame by measuring the voltage on terminals 11 of thermoelectric generator. If voltage drop within 15 seconds is greater than 0.4 V, the system initiates flame disappearance, the burner is restarted, and if the burner could not be restarted, an error message is displayed on optical indicator unit 6.

In 2 hours of operation in the absence of manual disconnection of the heater – it is switched off automatically – the fan power increases to maximum and fuel delivery stops (“blowdown” mode).

In 10 minutes the device goes to standby mode, and the heater can be re-started by turning the knob of thermal controller 7 to position below 30 °C and re-setting of the necessary temperature.

Thus, operation algorithm of the heater is based on smooth increment of heat source thermal power and gradual increase of electric power consumption by the heater components.

Such automatic alternate transition from the moment of components initiation to the mode of maximum power through a series of intermediate modes [5] provides reliable starting and stable operation of device.

## **Research results**

The operation algorithm of electronic unit paired with components of thermoelectric automobile heater is illustrated by the results of bench tests (Fig. 4 – 7).

The evidence presented suggests that the behaviour of both temperature and electrical dependences is practically identical. After switching on the device and up to the moment of reaching the assigned heat carrier temperature the electronic unit in conformity with the algorithm in microprocessor gradually increases thermal power of heat source to maximum. In so doing, accordingly, there is increase in temperature characteristics  $T_c$ ,  $T_h$ ,  $T_{gas}$  and transfer from the battery mode of components power supply to autonomous mode. With increasing electric power output of the generator, the electronic unit directs excess electric energy to battery recharging.

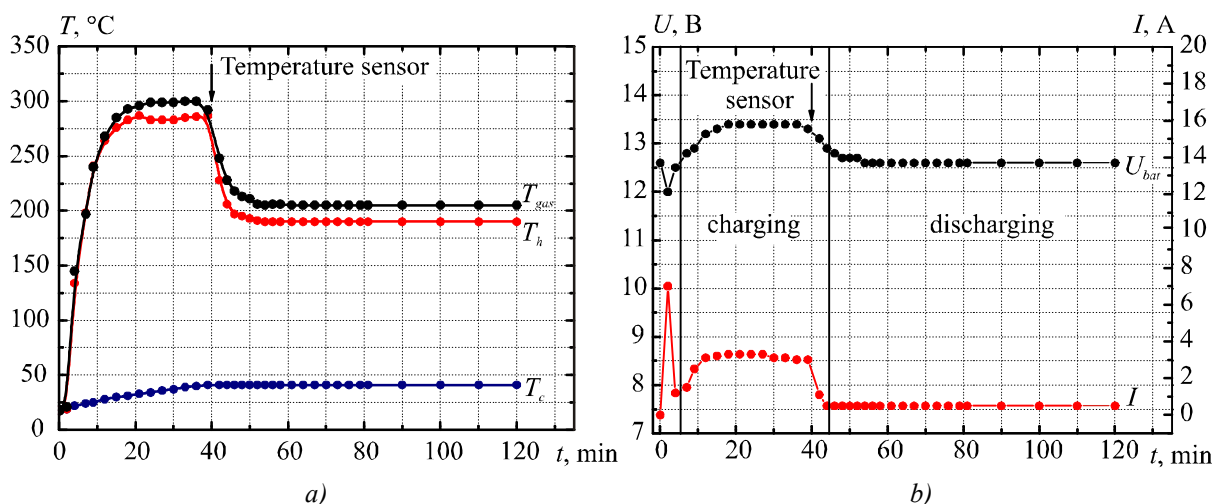


Fig. 4. Results of research on thermoelectric automobile heater with electronic control unit:  
 $T_{gas}$  – outlet gas temperature;  $T_h$  – hot heat exchanger temperature;  
 $T_c$  – cold heat exchanger temperature;  $U_{bat}$  – battery voltage;  
 $I$  – current in “heater”-“battery” circuit. Heat carrier temperature is set at 40 °C.

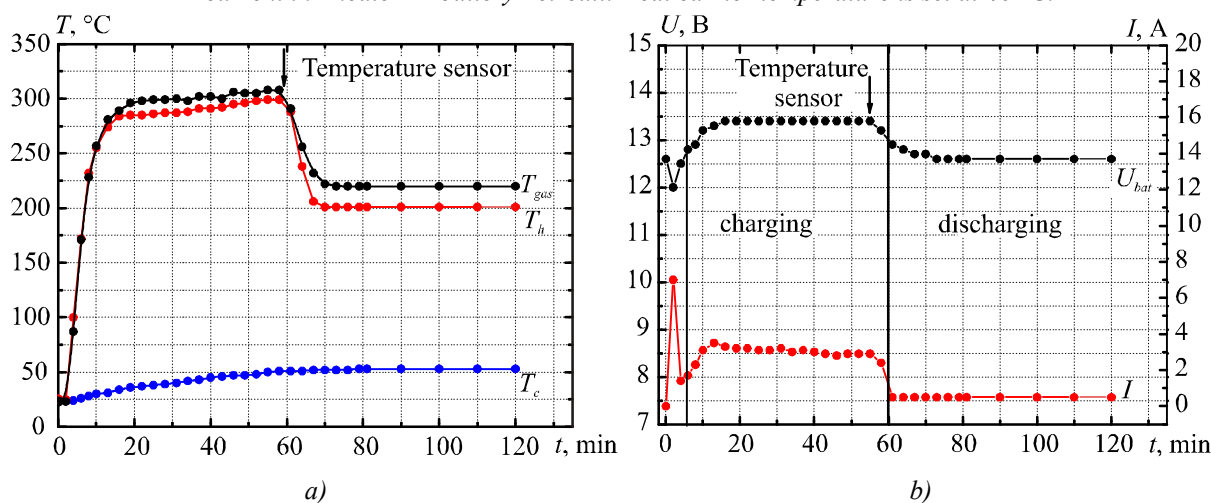


Fig. 5. Results of research on thermoelectric automobile heater with electronic control unit.  
 Heat carrier temperature is set at 50 °C. The notation is similar to Fig. 4.

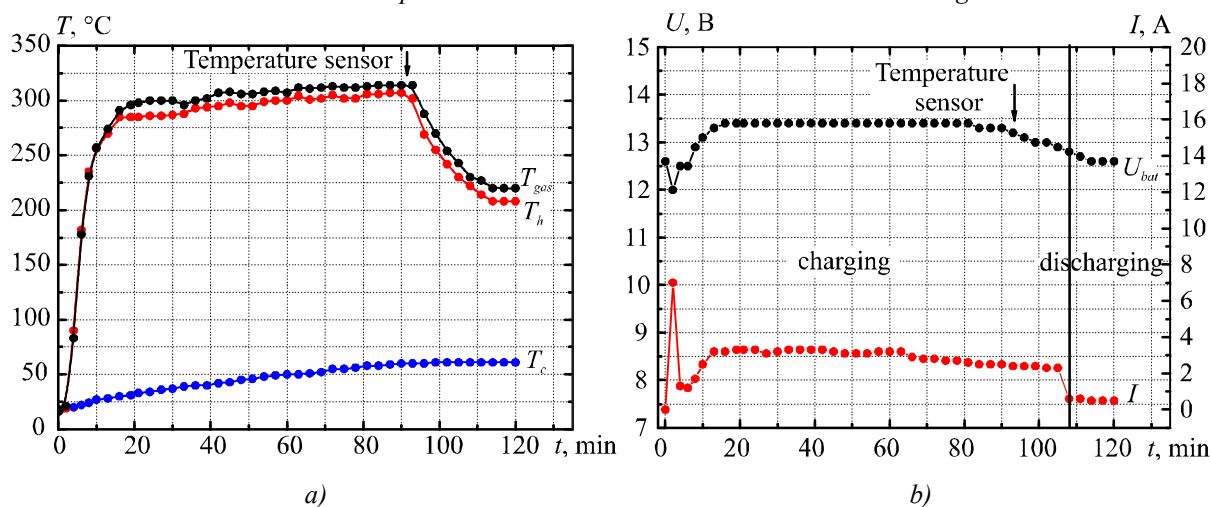
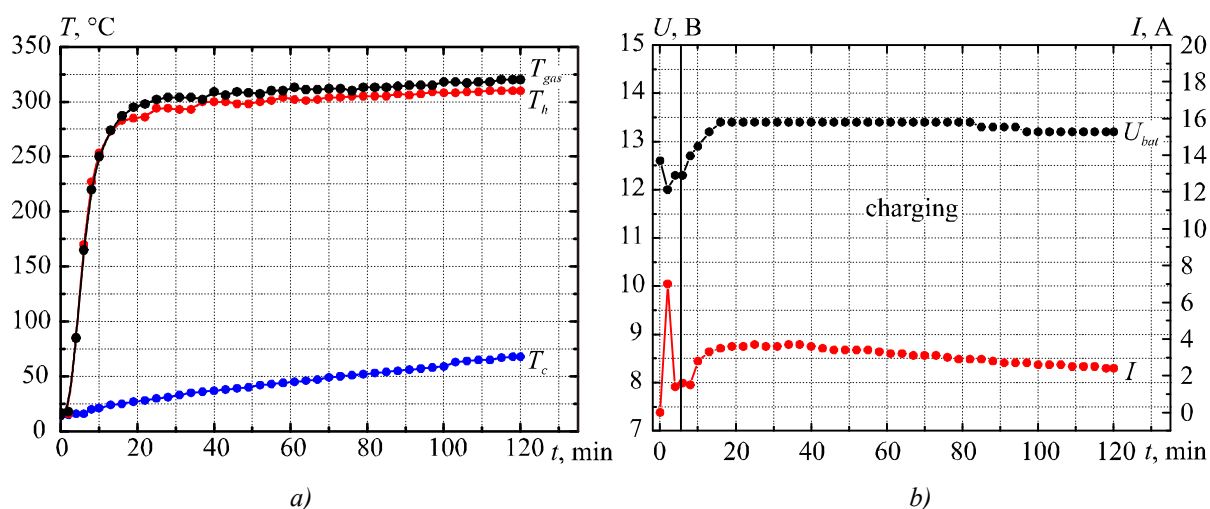


Fig. 6. Results of research on thermoelectric automobile heater with electronic control unit.  
 Heat carrier temperature is set at 60 °C. The notation is similar to Fig. 4.

When the set temperature of heat carrier is reached, the electronic unit in conformity with the output signal of digital thermal sensor, which is on one of the liquid heat exchangers of the heater, increases the period of fuel delivery to the burner and the heater starts working in the mode of set temperature support. In so doing, the temperature on the hot heat exchanger and the temperature of gases drop, and the temperature on the cold heat exchangers is stabilized. Note that in this mode the power generated by thermoelectric modules is insufficient for battery recharging, so the electronic unit by reversing current in “heater”-“battery” circuit switches power supply of components from the modules back to the battery. As can be seen from Fig. 4 – 6, under these conditions battery discharge current is as low as  $\sim 0.2$  A, which as compared its capacity is certainly a very low value (for instance, discharge current in operation of starting pre-heater “Webasto Thermo Top C” is an order of magnitude higher – 3 – 5 A). Therefore, it can be stated that in heat carrier temperature support mode the heater actually works without the use of battery energy.



*Fig. 7. Results of research on thermoelectric automobile heater with electronic control unit.  
 Heat carrier temperature is set at 70 °C. The notation is similar to Fig. 4.*

With heat carrier temperature set at 70 °C (Fig. 7) digital thermal sensor does not work, since heat carrier is heated to given temperature practically at the moment of switching off the heater. However, there are special advantages in this, since automobile battery is constantly charging.

It is also noteworthy that in the course of investigations an emergence situation was artificially created in operation of the heater by alternative disconnection from power supply of a fuel pump, a fan, a circulation pump. The results confirm the rationality of chosen algorithm for system protection from overheats and other dangerous situations, namely the electronic unit initializes an error in the operation of the heater (disappearance of flame in combustion chamber, overheat of the cold side of modules, etc.) and stops its work – the heater switches to “blowdown” mode. In so doing, as noted earlier, a signal of respective error type is displayed on control panel.

## Conclusions

1. A fundamentally new design of electronic control unit for thermoelectric starting pre-heater was created where thermoelectric converter is used as a flame sensor, and thermoelectric modules of the converter – for self-energizing of the system and battery recharging.
2. It was shown that heater control is carried out by an intelligent control algorithm of flame, air and fuel delivery and battery charge, which assures stable operation of device and creates a reliable

protection system in case of emergency.

3. As a result of experimental tests, the rationality of chosen electronic unit design and of the algorithm of heater operation employed was confirmed.

### **References**

1. V.S. Naiman, *All about Starting Pre-Heaters* (Moscow: ACT, 2007), p. 213.
2. V.Ya. Mykhailovsky, M.V. Maksimuk, Automobile Operating Conditions at Low Temperatures. The Necessity of Applying Heaters and the Rationality of Using Thermal Generators for their Work, *J.Thermoelectricity* 3, 20 – 31 (2015).
3. V.Ya. Mykhailovsky, M.V. Maksimuk, Rational Powers of Thermal Generators for Starting Pre-Heaters of Vehicles, *J.Thermoelectricity* 4, 69 – 77 (2015).
4. V.Ya. Mykhailovsky, M.V. Maksimuk, Computer Design of Thermoelectric Automobile Starting Pre-Heater Operated with Diesel Fuel, *J.Thermoelectricity* 1, 52 – 65 (2016)
5. L.I. Anatyshuk, V.Ya. Mykhailovsky, M.V. Maksimuk, I.S. Andrusiak, Experimental Research on Thermoelectric Automobile Starting Pre-Heater Operated with Diesel Fuel, *J.Thermoelectricity* №4, 81 – 90 (2016).
6. Patent (UA) № 72304 InCl: F01N 5/00; H01L35/00 Automobile Heater with Thermoelectric Power Supply / L.I.Anatyshuk, V.Ya.Mykhailovsky. – Publ. 10.08.2012, Bul. № 15, Appl. u2012 02055 of 23.02.2012.
7. Patent (UA) № 102303 InCl F01N 5/00 H01L 35/00 Thermoelectric Power Supply for Automobile / L.I. Anatyshuk, V.Ya. Mykhailovsky. – Publ. 25.06.2013, Bul. № 12, Appl u2011 13957 of 28.11.2011.
8. Patent (UA) № 90764 InCl F02N 19/00 Control System of Liquid Starting Pre-Heater for Internal Combustion Engines / V.Ya. Mykhailovsky, P.V. Zvozdetskyi, M.V. Maksimuk. – Publ. 10.06.2014, Bil № 11, Appl.u2013 15422 of 30.12.2013.

Submitted 29.09.2016

---

**L.I. Anatyчук<sup>1,2</sup>, A.V. Prybyla<sup>1</sup>, M.M. Korop<sup>1</sup>**

<sup>1</sup>Institute of Thermoelectricity of the NAS and MES Ukraine,  
1 Nauky str., Chernivtsi, 58029, Ukraine;

<sup>2</sup>Yu.Fedkovich Chernivtsi National University,  
2 Kotsyubynsky str., Chernivtsi, 58012, Ukraine

---

**COMPARATIVE ANALYSIS OF THERMOELECTRIC  
AND COMPRESSION HEAT PUMPS  
FOR INDIVIDUAL AIR CONDITIONERS AT  
ELEVATED AMBIENT TEMPERATURES**

---

*The paper presents the results of comparative analysis of thermoelectric and compression heat pumps for their use in human air conditioners at elevated ambient temperatures.*

**Key words:** thermoelectric heat pump, compression heat pump, human air conditioner.

## **Introduction**

*General characterization of the problem.* In the literature, reference is made to the possibility of human body air-conditioning by various methods [1 – 9]. Of particular interest are methods based on the use of compression and thermoelectric heat pumps. This is due to their advantages, namely high energy conversion efficiency and possibility of operation both in cooling and heating modes. Paper [10] gives a comparative analysis of thermoelectric and compression heat pumps for individual air conditioners with respect to their energy and weight-and-size characteristics in the range of ambient temperatures 20 – 30 °C. This enabled us to identify the advantages of thermoelectric heat pumps under low supply powers (up to 500 W) which correspond to operating conditions of human air conditioners.

However, of particular interest is the use of human air conditioners at elevated ambient temperatures (37 °C and more), which is related to complicated human body heat exchange with the environment. As shown by the analysis of the literature, such operating conditions of heat pumps are understudied.

*The purpose of this paper* is to determine the opportunities for further quality improvement of individual human air conditioners based on thermoelectric and compression heat pumps by their comparative analysis under elevated ambient temperatures.

## **Calculation of energy characteristics of thermoelectric heat pump**

For comparative analysis of characteristics of heat pumps, computer calculations of thermoelectric heat pump were performed on the basis of a physical model presented in Fig 1. It comprises thermoelectric modules 1, the hot 3 and cold 6 heat exchangers, thermal contact resistances between them 4, 5 and liquid pumps 2, 7 which assure motion of heat carriers through heat exchangers ( $W_1$ ,  $W_2$ ). Temperature differences along heat exchangers are considered to be minor and can be ignored.

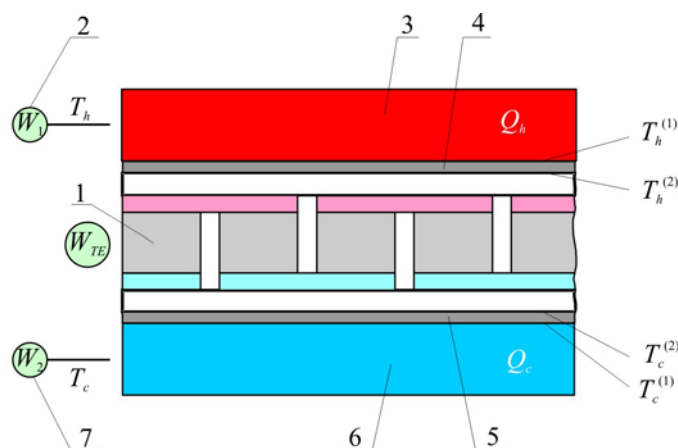


Fig. 1. Physical model of thermoelectric heat pump.

A system of equations describing coefficient of performance as a function of parameters of physical model elements is determined from heat balance equations in the heat pump:

$$\begin{cases} Q_c = \chi_1(T_c^{(1)} - T_c) \\ Q_c = \chi_2(T_c^{(2)} - T_c^{(1)}) \end{cases}, \quad (1)$$

$$\begin{cases} Q_h = \chi_3(T_h^{(2)} - T_h^{(1)}) \\ Q_h = \chi_4(T_h^{(1)} - T_h) \end{cases}, \quad (2)$$

$$Q_h = Q_c + W_{TE}. \quad (3)$$

Here,  $T_c$  – cold heat carrier temperature,  $T_c^{(1)}$  – cold heat exchanger temperature,  $T_c^{(2)}$  – cold side temperature of thermoelectric module,  $T_h$  – hot heat carrier temperature,  $T_h^{(1)}$  – hot heat exchanger temperature,  $T_h^{(2)}$  – hot side temperature of thermoelectric module,  $\chi_1$  is thermal resistance of the cold heat exchanger 6,  $\chi_2$  is thermal contact resistance 4,  $\chi_3$  is thermal contact resistance 5,  $\chi_4$  is thermal resistance of the hot heat exchanger 3,  $Q_c$  is cooling capacity of thermal pump,  $Q_h$  is its heating efficiency.

With regard to (1) – (3), the expression for a real coefficient of performance of thermoelectric heat pump will be given by:

$$\varepsilon_r = \frac{Q_c}{W_{TE} + W_1 + W_2} = \frac{\alpha I(T_c + Q_c N_1) - 0.5 I^2 R - \lambda(T_h - T_c - (Q_h N_2 + Q_c N_1))}{W_{TE} + W_1 + W_2}, \quad (4)$$

where  $N_1 = \frac{(\chi_1 + \chi_2)}{\chi_1 \chi_2}$ ,  $N_2 = \frac{(\chi_3 + \chi_4)}{\chi_3 \chi_4}$ .

In the simulation, structural parameters of thermoelectric heat pump, as well as computer simulation procedure described in detail in [10] were used. The results of simulation are given below.

### Comparison of thermoelectric and compression individual human air conditioners

For comparison, analysis of the literature on compression heat pumps at elevated ambient temperatures was performed. Analysis shows that the use of compression heat pumps is restricted by maximum ambient temperature 45 °C [11]. In so doing, the value of cooling efficiency with a rise in



temperature drastically decreases. Despite scarce information on the characteristics of compression heat pumps at elevated temperatures, it has been found in [12, 13] (Fig. 2). The reported compression heat pump has electric power 3 kW, which does not correspond to the range of using individual human air conditioners. However, using the dependences of efficiency of compression heat pumps on their power obtained in [10], the dependences of coefficient of performance of compression heat pumps on ambient temperature for their different powers were found (Fig. 2).

For illustrative reasons we graphically construct a comparative characteristic of the coefficient of performance of compression and thermoelectric heat pumps versus ambient temperature (Fig. 2).

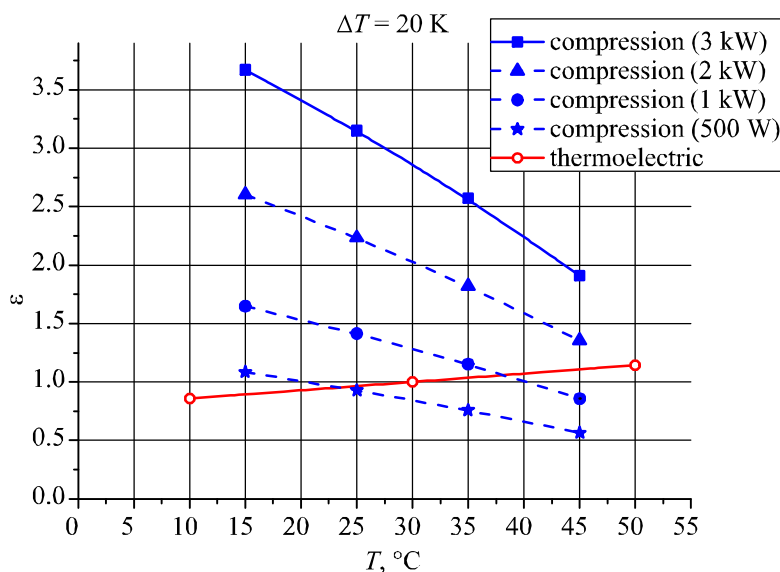


*Fig. 2. Dependence of coefficient of performance of compression (blue lines) and thermoelectric (red line) heat pumps on the ambient temperature.*

As is evident from Fig. 2, coefficient of performance of compression heat pumps considerably decreases with a rise in ambient temperature. Coefficient of performance of thermoelectric heat pumps in this case not only does not decrease, but even increases. Thus, thermoelectric heat pumps offer a definite advantage over compression pumps at elevated ambient temperatures in the range of low cooling capacities (up to 500 W), which correspond to operating conditions of human air conditioners.

## Conclusions

1. Coefficient of performance of thermoelectric heat pump was calculated versus ambient temperature and shown to increase with a rise in temperature.
2. Coefficient of performance of compression heat pumps was shown to drastically decrease with a rise in ambient temperature.
3. It was established that thermoelectric heat pumps offer a definite advantage over compression heat pumps at elevated ambient temperatures (above 30 °C) in the range of low cooling capacities (up to 500 W), which correspond to operating conditions of human air conditioners.

## References

1. Pat. 66389 Ukraine, InCl 2011.01, Overheat Protective Garment / L.V.Moroz; Publ. 26.12.11, Bul № 24.

2. Pat. US 3950789, Dry Ice Cooling Jacket / Stephan A. Konz, Jerry R. Duncan.- Pub. Date: Apr. 20, 1976.
3. Pat. CN 203633537 U, Fan Type Cooling Human Body Air Conditioning Clothes / Tian Weiguo.- Pub. Date: June, 11, 2014.
4. Pat. US 20060191270 A1, Air Conditioning System for a Garment / Ray Warren.- Pub. Date: Aug, 31, 2006.
5. Pat. US 20020073481 A1, Cooling Garment / Christopher Creagan, Charles Bolian, Irwin Singer.- Pub. Date: June, 20, 2002.
6. K.-Ch.Noutel, Systems of Working Clothes for Extremely Cold Working Conditions, *Mining Information-Analytical Bulletin 2* (2002).
7. Pat. US3524965 A, Electric Heating Element for Apparel / Stanley Arron.- Pub. Date: Aug. 18, 1970.
8. Pat. US 2010/0107657 A1, Appparel with Heating and Cooling Capabilities / Kranthi K. Vistakula.- Pub. Date: May. 6, 2010.
9. A.V. Prybyla, Physical Models of Personal Air-Conditioners (part one), *J.Thermoelectricity* 1, 16 –39 (2016).
10. A.V.Prybyla, Comparative Analysis of Thermoelectric and Compression Heat Pumps for Individual Air-Conditioners, *J.Thermoelectricity* 2, 31 – 39 (2016).
11. GOST 16317-87 Cooling Electric Devices. General Specifications.
12. A.I.Eydeius, V.L.Koshelev, Operating Efficiency of Air-Conditioners with a Capillary Tube under Off-Design Conditions, *Ventilation, Heating, Air Conditioning, Heat Supply and Building Thermal Physics* 5 (2007).
13. <http://www.airwell-residential.com/>

Submitted 10.11.2016

## ARTICLE PREPARATION RULES

The article shall conform to the journal profile. The article content shall be legible, concise and have no repetitions.

The article shall be submitted to the editorial board in electronic version.

The text shall be typed in text editor not lower than MS Word 6.0/7.0.

Page setup: “mirror margins”- top margin – 2.5 cm, bottom margin – 2.0 cm, inside – 2.0 cm, outside– 3.0 cm, from the edge to page header – 1.27 cm, page footer – 1.27 cm.

Graphic materials, pictures shall be submitted in color or, as an exception, black and white, in .opj or .cdr formats, .jpg or .tif formats being also permissible. According to author’s choice, the tables and partially the text can be also in color.

The article shall be submitted in English on A4 paper sheets; the number of pages shall not exceed 12. By agreement with the editorial board, the number of pages can be increased.

### **To accelerate publication of the article, please adhere to the following rules:**

- the authors’ initials and names are arranged in the centre of the first page at the distance of 1 cm from the page header, font Times New Roman, size 12 pt, line spacing 1.2;
- the name of organization, address (street, city, postal code, country) – indent 1 cm below the authors’ initials and names, font Times New Roman, size 11 pt, line spacing 1.2, center alignment;
- the title of the article is arranged 1 cm below the name of organization, in capital letters, semi-bold, font New Roman, size 12 pt, line spacing 1.2, center alignment. The title of the article shall be concrete and possibly concise;
- the abstract is arranged 1 cm below the title of the article, font Times New Roman, size 10 pt, in italics, line spacing 1.2, center alignment;
- key words are arranged below the abstract, font Times New Roman, size 10 pt, line spacing 1.2, justified alignment. The title “Key words” – font Times New Roman, size 10 pt, semi-bold;
- the main text of the article is arranged 1 cm below the abstract, indent 1 cm, font Times New Roman, size 11 pt, line spacing 1.2, justified alignment;
- formulae are typed in formula editor, fonts Symbol, Times New Roman. Font size is “normal” – 12 pt, “large index” – 7 pt, “small index” – 5 pt, “large symbol” – 18 pt, “small symbol” – 12 pt). The formula is arranged in the text, centre aligned and shall not occupy more than 5/6 of the line width, formulae are numbered in round brackets right;
- dimensions of all quantities used in the article are represented in the International System of Units (SI) with the explication of the symbols employed;
- figures are arranged in the text. The figures and pictures shall be clear and contrast; the plot axes – parallel to sheet edges, thus eliminating possible displacement of angles in scaling;
- tables are arranged in the text. The width of the table shall be 1 cm less than the line width. Above the table its ordinary number is indicated, right alignment. Continuous table numbering throughout the text. The title of the table is arranged below its number, center alignment;
- references should appear at the end of the manuscript. References within the text should be enclosed in square brackets. References should be numbered in order of first appearance in the text. Examples of various reference types are given below.

- L.I. Anatyshuk, *Thermoelements and Thermoelectric Devices: Handbook* (Kyiv: Naukova Dumka, 1979), p.766. (Book)
- T.M. Tritt, Thermoelectric Phenomena, Materials, and Applications, *Annual Review of Materials Research* **41**, 433 (2011). (Journal paper)
- U.Ghoshal, *Proceedings of the XXI International Conference on Thermoelectrics* (N.Y., USA, 2002), p. 540. (Proceedings Conference)

**The article should be supplemented by:**

- letter from the organization where the work was performed or from the authors of the work applying for the publication of the article;
- information on the author (authors): last name and initials; full name and postal address of the institution where the author works; academic degree; position; telephone number; E-mail;
- author’s (authors’) photo in color or, as an exception, in black and white. With the number of authors more than two their photos are not given;
- author’s application to the following effect:

We, the undersigned authors, ... transfer to the founders and editors of “Journal of Thermoelectricity” the right to publish the article...in Ukrainian, Russian and English. This is to confirm that the present publication does not violate the copyright of other persons or organizations.

Date

Signatures